

**Investigation of the Effects of Compressibility on Profile Pressure Losses
in Axial Turbine Cascades**

by

Steven Ronald Hall

**A thesis submitted to the Faculty of Graduate and Postdoctoral Affairs
in partial fulfillment of the requirements of the degree of**

Master of Applied Science

in

Aerospace Engineering

**Carleton University
Ottawa, Ontario**

**© 2012
Steven Ronald Hall**



Library and Archives
Canada

Published Heritage
Branch

395 Wellington Street
Ottawa ON K1A 0N4
Canada

Bibliothèque et
Archives Canada

Direction du
Patrimoine de l'édition

395, rue Wellington
Ottawa ON K1A 0N4
Canada

Your file Votre référence

ISBN: 978-0-494-93473-9

Our file Notre référence

ISBN: 978-0-494-93473-9

NOTICE:

The author has granted a non-exclusive license allowing Library and Archives Canada to reproduce, publish, archive, preserve, conserve, communicate to the public by telecommunication or on the Internet, loan, distribute and sell theses worldwide, for commercial or non-commercial purposes, in microform, paper, electronic and/or any other formats.

The author retains copyright ownership and moral rights in this thesis. Neither the thesis nor substantial extracts from it may be printed or otherwise reproduced without the author's permission.

AVIS:

L'auteur a accordé une licence non exclusive permettant à la Bibliothèque et Archives Canada de reproduire, publier, archiver, sauvegarder, conserver, transmettre au public par télécommunication ou par l'Internet, prêter, distribuer et vendre des thèses partout dans le monde, à des fins commerciales ou autres, sur support microforme, papier, électronique et/ou autres formats.

L'auteur conserve la propriété du droit d'auteur et des droits moraux qui protègent cette thèse. Ni la thèse ni des extraits substantiels de celle-ci ne doivent être imprimés ou autrement reproduits sans son autorisation.

In compliance with the Canadian Privacy Act some supporting forms may have been removed from this thesis.

While these forms may be included in the document page count, their removal does not represent any loss of content from the thesis.

Conformément à la loi canadienne sur la protection de la vie privée, quelques formulaires secondaires ont été enlevés de cette thèse.

Bien que ces formulaires aient inclus dans la pagination, il n'y aura aucun contenu manquant.

Canada

Abstract

An improved wind tunnel control system based on Mach number has been developed. Compared with the previous control system, the new system gives improved control of the Mach number, shorter settling times, and allows the wind tunnel to run stably at Mach numbers as low as 0.1.

Experiments and computations were performed at the midspan of a turbine cascade. The experiments were run at Mach numbers from 0.2 to 1.00 with corresponding Reynolds numbers of 155,000 to 831,000.

The results indicate that the effect of both the Reynolds number and Mach number on the total pressure losses have a similar magnitude for the range studied. The Reynolds number effects on losses are attributed to changes in the boundary layers. The effects of Mach number on the losses are attributed both to the change in the transition location and the change in the loading distribution.

The results were combined with data from the literature to evaluate the Reynolds number and compressibility corrections in the Kacker and Okapuu loss system. A tentative Reynolds number correction is suggested based on the computational results. Also, it is suggested that the shock losses will affect the losses before an exit Mach number of 1.0.

Acknowledgements

First, I'd like to thank my thesis supervisor, Professor Sjolander for his patient guidance and advice. I am grateful for all his input which has ensured that this thesis is of the highest quality.

I would also like to express my gratitude to Farzad Taremi and Hamza Abo El Ella for showing me how to operate the wind tunnel, and always being willing to return to help me with my endless questions. I must also acknowledge the insight and support provided by my fellow students: Andrew Scribner, Cameron MacLean, Gordon MacIsaac, Chris Sooriyakumaran, and Jean-Michel Prévost were always available to discuss the challenges I faced, or just to take a much needed lunch break.

The financial support provided by Pratt & Whitney Aircraft is gratefully acknowledged.

Above all, I wish to thank my family, especially my parents. No matter how difficult things were, I could always count on them to provide the support and motivation I needed to overcome the obstacles I faced.

Table of Contents

Abstract.....	ii
Acknowledgements.....	iii
List of Tables.....	xii
List of Figures.....	xv
List of Symbols.....	xxv
Chapter 1 Introduction.....	1
Chapter 2 Literature Review.....	4
2.1 Introduction.....	4
2.2 Description of the Flow in an Axial Turbine Blade Passage.....	4
2.3 Decomposition of the Losses for an Axial Turbine Blade Passage.....	7
2.4 Loss Coefficients.....	8
2.5 Aerodynamic Influences on Midspan Losses.....	10
2.5.1 Compressibility Effects on Midspan Losses.....	10
2.5.2 Base Pressure Influence on Trailing Edge Losses.....	15
2.5.3 Influence of Reynolds Number on Midspan Losses.....	17
2.5.4 Influence of Free-Stream Turbulence on Midspan Losses.....	19

2.5.5	Axial-Velocity-Density Ratio (AVDR)	20
2.6	Correlations for Profile Loss Prediction at Design Incidence	22
2.6.1	Ainley and Mathieson Loss System	22
2.6.2	Modifications to the Ainley and Mathieson System due to Dunham and Came	25
2.6.3	Modifications to the Ainley and Mathieson System due to Kacker and Okapuu	26
Chapter 3	Experimental Set-up and Measurement Methods.....	31
3.1	Introduction	31
3.2	High Speed Wind Tunnel	32
3.2.1	Air Supply	32
3.2.2	Cascade Test Section	34
3.2.3	Probe Calibration Rig	36
3.3	Instrumentation	38
3.3.1	Pressure Transducers	38
3.3.2	Three-Hole Probe	39
3.3.3	Test Section Endwall Measurements	42
3.3.4	Upstream Reference Total Pressure and Temperature Measurements	42
3.3.5	Data Acquisition System	43
3.3.6	Uncertainties in Measured Values	44

3.4	SL2 Cascade Geometry.....	45
Chapter 4 Design of an Improved Wind Tunnel Control System		46
4.1	Introduction.....	46
4.2	Control System Components.....	47
4.2.1	Introduction.....	47
4.2.2	Pressure Measurement.....	49
4.2.3	Data Acquisition Hardware and Software.....	50
4.2.4	Control Software	50
4.2.5	Control Valves	53
4.3	Characteristics of the System Response	54
4.3.1	Introduction	54
4.3.2	Initial Threshold Voltage	58
4.3.3	Valve Dead Band.....	59
4.3.4	Undershoot of Target Mach Number.....	61
4.3.5	Repeatability.....	62
4.3.6	System Response During Data Collection.....	64
4.4	Influence of PID Gains on System Response	65
4.4.1	Introduction	65
4.4.2	Influence of Proportional Gain, K_P	66
4.4.3	Influence of Integral Gain, K_I	67
4.4.4	Influence of Derivative Gain, K_D	69

4.4.5	Influence of Mach Number	70
4.5	Comparison to Previous Control System.....	71
4.5.1	Introduction.....	71
4.5.2	Qualitative Comparison to Previous Control System on Main Wind Tunnel	72
4.5.3	Settling Time.....	75
4.5.4	Variation of Mach Number During the Run	76
4.5.5	User Interface	77
4.5.6	Range of Available Mach Numbers	80
4.6	Uncertainty of Data at Low Mach Numbers	80
4.6.1	Introduction.....	80
4.6.2	Uncertainty in the Mach Number	82
4.6.3	Uncertainty in the Total Pressure Loss Coefficient	83
4.6.4	Uncertainty in the Integrated Pressure.....	84
4.7	Conclusions.....	85
Chapter 5	Computational Procedure and Results.....	87
5.1	Introduction.....	87
5.2	Test Cases	87
5.3	Solution Method	90
5.3.1	Solver.....	90

5.3.2	Mesh.....	91
5.3.3	Boundary Conditions.....	94
5.3.4	Turbulence Model.....	95
5.4	Mach Number Effects at a Fixed Reynolds Number.....	98
5.4.1	Introduction.....	98
5.4.2	Blade Loadings.....	99
5.4.3	Boundary Layer Properties.....	102
5.4.4	Losses.....	107
5.4.5	Flow Angles.....	109
5.4.6	Wake Profiles.....	110
5.5	Reynolds Number Effects at a Fixed Mach Number.....	111
5.5.1	Introduction.....	111
5.5.2	Blade Loadings.....	112
5.5.3	Boundary Layer Properties.....	114
5.5.4	Losses.....	118
5.5.5	Flow Angles.....	119
5.5.6	Wake Profiles.....	120
5.6	Combined Mach Number and Reynolds Number Effects Corresponding to a Fixed Exit Pressure.....	121
5.6.1	Introduction.....	121
5.6.2	Blade Loadings.....	122

5.6.3	Boundary Layer Properties.....	123
5.6.4	Losses	126
5.6.5	Flow Angles	128
5.6.6	Wake Profiles.....	129
5.7	Conclusions	130
Chapter 6 Experimental Performance Results of the SL2 Cascade		133
6.1	Introduction.....	133
6.2	Flow Quality.....	135
6.2.1	Introduction.....	135
6.2.2	Exit Flow Angles and Exit Flow Angle Correction.....	135
6.2.3	Upstream Uniformity	138
6.2.1	Axial-Velocity-Density Ratio.....	139
6.2.2	Periodicity.....	141
6.3	Blade Loadings.....	143
6.4	Losses	144
6.5	Wake Profiles	145
6.6	Conclusions	147
Chapter 7 Development of Correction Factors for the Effects of Reynolds		
Number and Mach Number on Profile Losses		149
7.1	Introduction.....	149
7.2	Correction Factors for Design Point Selection Compared to Off-Design...	150

7.3	Comparison of Numerical and Experimental Losses from the Present Study	152
7.4	Sources of Data from the Literature	155
7.5	Reynolds Number Correction	157
7.5.1	Introduction	157
7.5.2	Development of New Reynolds Number Correction Formula.....	159
7.5.3	Effect of Proposed Reynolds Number Correction	165
7.5.4	Choice of Reference Reynolds Number	166
7.5.5	Future Development of the Reynolds Number Correction	168
7.6	Subsonic Mach Number Correction	169
7.6.1	Introduction	169
7.6.2	Subsonic Mach Number Correction in the Kacker and Okapuu Loss System.....	170
7.6.3	Estimation of the Incompressible Limit.....	173
7.6.4	Dependence of Incompressible Limit on the Testing Facility	176
7.6.5	Evaluation of Subsonic Correction Factor from Kacker and Okapuu Loss System.....	179
7.6.6	Onset of Shock Losses Within the Blade Passage	183
7.6.7	Suggested Improvements to the Subsonic Mach Number Design Correction	184

7.6.8 Discussion and Recommendations for Future Development of Subsonic Mach Number Loss Corrections.....	184
Chapter 8 Conclusions and Recommendations.....	187
8.1 Conclusions.....	187
8.2 Recommendations for Future Work.....	190
References	194
Appendix A Three-Hole Probe Calibration.....	201
A.1 Calibration Procedure.....	201
A.2 Calibration Results	204
Appendix B Pressure Transducer Calibrations	206
Appendix C SL2 Geometry	208
Appendix D Mixed-Out Computational Results for SL2 Cascade	211
Appendix E Mixed-Out Experimental Results for SL2 Cascade	213
Appendix F Performance Data at Design Incidence for Several Cascades from the Literature	214

List of Tables

Table 2.1 Nomenclature of Turbine Blade	6
Table 2.2 Summary of Experimental Investigations on the Effect of Mach Number on Midspan Performance	12
Table 3.1 Ranges of the Transducers Used in This Study	39
Table 3.2 Summary of Measured Values and Associated Uncertainties.....	44
Table 3.3 SL2 Geometric and Design Flow Parameters	45
Table 5.1 Mesh Quality Criteria.....	94
Table 7.1 Summary of Data Sources from Literature	156
Table B.1 Pressure Transducer Calibration Coefficients.....	207
Table C.1 SL2 Coordinates.....	208
Table C.2 Blade Surface Static Tap Locations	210
Table D.1 Mixed-Out Performance Data for CFD Simulations on SL2 Cascade at a Constant Reynolds Number of 611,000	211
Table D.2 Mixed-Out Performance Data for CFD Simulations on SL2 Cascade at a Constant Mach Number of 0.49	211
Table D.3 Mixed-Out Performance Data for CFD Simulations on SL2 Cascade at a Constant Mach Number of 0.77	212

Table D.4 Mixed-Out Performance Data for CFD Simulations on SL2 Cascade with Mach Number and Reynolds Number Corresponding to an Exit Pressure of 1atm	212
Table D.5 Mixed-Out Performance Data for CFD Simulations on SL2 Cascade with Mach Number and Reynolds Number Corresponding to Wind Tunnel Conditions	212
Table E.1 Mixed-Out Performance Data for SL2 Cascade.....	213
Table F.1 Performance Data for HS1A Cascade (Corriveau, 2005; Jouini, 2000)	214
Table F.2 Performance Data for HS1C Cascade (Corriveau, 2005)	215
Table F.3 Performance Data for HS1D Cascade (Corriveau, 2005).....	215
Table F.4 Performance Data for HS2 Cascade from Carleton Facility (Jeffries, 2000).....	216
Table F.5 Performance Data for HS2 Cascade from VKI Rhode-St.-Genève, Belgium (RG) Facility (Kiock et al. 1986)	216
Table F.6 Performance Data for HS2 Cascade from DFVLR Goettingen, West Germany (GO) Facility (Kiock et al. 1986)	217
Table F.7 Performance Data for HS2 Cascade from Braunschweig, West Germany (BS) Facility (Kiock et al. 1986)	217
Table F.8 Performance Data for SL1 Cascade (Taremi 2010)	217
Table F.9 Performance Data for SL2 Cascade (Taremi 2010)	218
Table F.10 Performance Data for CNPM Cascade (Perdichizzi, 1990).....	218

Table F.11 Incompressible Limits of Reynolds Number Corrected Total	
Pressure Loss Coefficient.....	219
Table F.12 Onset Mach Number of Shock Losses	219

List of Figures

Figure 2.1 Flow Features in an Axial Turbine Blade Passage (Adapted From Jeffries 2000 by Corriveau 2005)	5
Figure 2.2 Terminology of Turbine Blade and Cascade Geometry.....	6
Figure 2.3 Enthalpy-Entropy Diagram for a Turbine Cascade Flow (Denton 1993).....	9
Figure 2.4 Variation of Various Loss Coefficients with Mach Number in Air When Total Pressure Loss Coefficient is 0.1 (Equations 2.1-2.4)	10
Figure 2.5 Shock Wave-Boundary Layer Interaction (Adapted from Japikse and Baines 1994 by Corriveau 2005)	13
Figure 2.6 Variation of Midspan Kinetic Energy Loss Components with Mach Number for a Test Cascade (Mee et al. 1992)	15
Figure 2.7 Base Pressure Correlation (Sieverding 1980)	17
Figure 2.8 Variation of Total Pressure Losses with Reynolds Number (Ladwig and Fottner 1993 as Reproduced by Jeffries 2000)	18
Figure 2.9 Energy Loss Variation with Reynolds Number at Different Freestream Turbulence Intensities for Blade Profiles T104, T105, and T106 (Hoheisel et al. 1987 as Reproduced by Corriveau 2005)	20
Figure 2.10 Variation of Losses with AVR (Rodger 1992).....	22
Figure 2.11 Predicted Loss Coefficient for Nozzle Blades (Ainley and Mathieson 1951).....	23

Figure 2.12 Predicted Loss Coefficient for Impulse Blades (Ainley and Mathieson 1951)	24
Figure 2.13 Trailing Edge Correction Factor (Ainley and Mathieson 1951)	25
Figure 2.14 Trailing Edge Energy Loss Coefficient (Kacker and Okapuu 1982).....	28
Figure 2.15 Variation of K_p with M_2 for Several Values of M_1/M_2	30
Figure 3.1 High Speed Wind Tunnel.....	32
Figure 3.2 Air Storage Tanks and Location of Control and Shutoff Valves.....	34
Figure 3.3 Cascade Test Section and Ejector-Diffuser.....	35
Figure 3.4 Cascade Test Section.....	35
Figure 3.5 Probe Calibration Rig.....	36
Figure 3.6 Dimensions of the Three-Hole Probe (reproduced from Islam 1999)	40
Figure 3.7 Probe Pitchwise Traverse Gear	41
Figure 3.8 Location of Upstream and Downstream Static Taps with Blades Numbered	42
Figure 4.1 Control System Schematic	48
Figure 4.2 Control Software Flow Diagram	51
Figure 4.3 Sample Responses with the New Control System on the Main Wind Tunnel.....	55
Figure 4.4 Sample Blowing Pressure Responses for Old Control System on the Main Wind Tunnel (Corriveau 2005).....	55

Figure 4.5 Variation of Mach Number, Blowing Pressure, and Static Pressure for the New Control System on the Main Wind Tunnel at a Mach Number of 0.69	56
Figure 4.6 Sample Responses with the New Control System on the Calibration Rig	57
Figure 4.7 Sample Responses with the Old Control System on the Calibration Rig	57
Figure 4.8 Response of the Control System on the Calibration Rig at a Target Mach Number of 0.8 Demonstrating the Result of the Valve Dead Band	60
Figure 4.9 Undershoot of the Target Mach Number with Compensation.....	62
Figure 4.10 Repeatability of the Control System on the Calibration Rig at a Target Mach Number of 0.4.....	63
Figure 4.11 Control System Data while the Data Acquisition System is Running	65
Figure 4.12 Influence of K_P on the System Response of the Main Wind Tunnel	67
Figure 4.13 Influence of K_I on the System Response of the Main Wind Tunnel.....	68
Figure 4.14 Influence of K_D on the System Response of the Main Wind Tunnel.....	69
Figure 4.15 Influence of the Target Mach Number on the System Response of the Main Wind Tunnel.....	70
Figure 4.16 Sample Blowing Pressure Responses for Old Control System on Main Wind Tunnel (Corriveau 2005).....	73
Figure 4.17 Blowing Pressure Response for New Control System on Main Wind Tunnel with Subsonic Target Mach Numbers.....	74

Figure 4.18 Blowing Pressure Response for New Control System on Main Wind Tunnel with Supersonic Target Mach Numbers	74
Figure 4.19 Comparison of the Settling Time for the Old and New Control Systems	76
Figure 4.20 Comparison of the Variation in Mach Number for the Old and New Control Systems.....	77
Figure 4.21 Estimated Uncertainty in the Measured Mach Number	83
Figure 4.22 Estimated Uncertainty in Loss Coefficient Assuming No Losses	84
Figure 5.1 CFD Test Cases in this Study	88
Figure 5.2 Example Mesh of the Fluid Domain.....	92
Figure 5.3 Close Up of the Mesh around the Trailing Edge	92
Figure 5.4 Boundary Conditions Used in the Simulations	95
Figure 5.5 Turbulence Intensity at Inlet of the Fluid Domain Using the CFX Default Settings.....	97
Figure 5.6 Turbulence Intensity at Inlet of the Fluid Domain Using Appropriate Settings.....	98
Figure 5.7 Blade Surface Isentropic Mach Numbers for the Fixed Reynolds Number of 611,000	100
Figure 5.8 Pressure Distribution at Mach 0.64	100
Figure 5.9 Shear Stresses Demonstrating Separation at Mach 0.89	101
Figure 5.10 Pressure Distribution at Mach 0.89 with Contour Lines Indicating Density Gradients.....	101

Figure 5.10 Transition Location at a Constant Reynolds Number of 611,000.....	104
Figure 5.11 Displacement Thickness and Shape Factor at a Mach Number of 0.77 and Reynolds Number of 611,000.....	105
Figure 5.12 Velocity Profile at the Location of Maximum Shape Factor at a Mach Number of 0.77 and Reynolds number of 611,000.....	105
Figure 5.13 Displacement Thickness at a Constant Reynolds Number of 611,000	106
Figure 5.14 Shape Factor at a Constant Reynolds Number of 611,000	107
Figure 5.15 Total Pressure Loss Coefficient at a Constant Reynolds Number of 611,000	108
Figure 5.16 Exit Flow Angle at a Constant Reynolds Number of 611,000.....	109
Figure 5.17 Wake Profiles at 1.4 C_x for a Constant Reynolds Number of 611,000...	111
Figure 5.18 Isentropic Surface Mach Numbers at Constant Mach Numbers of 0.49 and 0.77.....	112
Figure 5.19 Detailed View of the Isentropic Surface Mach Numbers after the Suction Peak at an Exit Mach Number of 0.49	113
Figure 5.20 Detailed View of the Isentropic Surface Mach Numbers after the Suction Peak at an Exit Mach Number of 0.77	113
Figure 5.21 Influence of Reynolds Number on Transition Location for Constant Mach Numbers of 0.49 and 0.77	114
Figure 5.22 Displacement Thickness Variation at a Constant Mach Number of 0.49	115

Figure 5.23 Displacement Thickness Variation at a Constant Mach Number of 0.77	116
Figure 5.24 Shape Factor Variation at a Constant Mach Number of 0.49	117
Figure 5.25 Shape Factor Variation at a Constant Mach Number of 0.77	117
Figure 5.26 Velocity Profile at the Location of the Maximum Shape Factor for a Mach Number of 0.77 and Reynolds Number of 200,000	118
Figure 5.27 Total Pressure Loss Coefficient at Constant Mach Numbers of 0.49 and 0.77	119
Figure 5.28 Influence of Reynolds Number on Exit Flow Angle for Constant Mach Numbers of 0.49 and 0.77	120
Figure 5.29 Wake Profiles at 1.4 C_x for Constant Mach Numbers of 0.49 and 0.77	121
Figure 5.30 Comparison of Blade Loadings for Constant Reynolds Number of 611,000 and Simulations which Approximated Wind Tunnel Conditions	123
Figure 5.31 Transition Location for a Constant Reynolds Number of 611,000 Compared to the Simulations which Approximated Wind Tunnel Conditions....	124
Figure 5.32 Transition Location for Constant Mach Numbers of 0.49 and 0.77 Compared to the Simulations which Approximated Wind Tunnel Conditions....	124
Figure 5.33 Variation of Displacement Thickness for the Simulations Approximating Wind Tunnel Conditions.....	125
Figure 5.34 Variation of Shape Factor for the Simulations Approximating Wind Tunnel Conditions.....	126

Figure 5.35 Total Pressure Loss Coefficient at Constant Mach Numbers of 0.49 and 0.77 Compared to the Simulations Approximating Wind Tunnel Conditions.....	127
Figure 5.36 Total Pressure Loss Coefficient at a Constant Reynolds Number of 611,000 Compared to the Simulations Approximating Wind Tunnel Conditions.....	128
Figure 5.37 Exit Flow Angle at a Constant Reynolds Number of 611,000 Compared to the Simulations which Approximated Wind Tunnel Conditions....	129
Figure 5.38 Wake Profiles at 1.4 C_x at a Constant Mach Number of 0.77 Compared to the Simulations Approximating Wind Tunnel Conditions.....	130
Figure 6.1 Experimental Test Cases Compared to CFD Test Cases Simulating Wind Tunnel Conditions.....	134
Figure 6.2 Location of Teflon Support.....	136
Figure 6.3 Exit Flow Angle Variation with Exit Mach Number for Experiment Compared to CFD with Reynolds Number Corresponding to Constant Exit Pressure	137
Figure 6.4 Illustration of Wake Centre Correction	138
Figure 6.5 Results of Upstream Uniformity Check.....	139
Figure 6.6 Variation of AVDR with Exit Mach Number	140
Figure 6.7 Results of Periodicity Check: Total Pressure Loss Coefficient.....	142
Figure 6.8 Results of Periodicity Check: Axial-Velocity-Density Ratio and Exit Flow Angle	142

Figure 6.9 Blade Loadings for Experiment Compared to CFD for Several Mach Numbers	144
Figure 6.10 Total Pressure Loss Coefficient Variation with Exit Mach Number for Experiment Compared to CFD Simulating Wind Tunnel Conditions	145
Figure 6.11 Selected Experimental Wake Profiles.....	146
Figure 6.12 Comparison of Selected Experimental and CFD Wake Profiles	147
Figure 7.1 Experimental Test Cases Compared to CFD Test Cases which Simulated Wind Tunnel Conditions	153
Figure 7.2 Total Pressure Loss Coefficient for Experiment Compared to CFD which Simulated Wind Tunnel Conditions.....	154
Figure 7.3 Comparison of Loss Prediction for SL2 CFD Test Cases Which Simulated Wind Tunnel Conditions and at Constant Reynolds Number of 600,000	158
Figure 7.4 Tentative New Reynolds Number Profile Loss Correction Compared to Existing Corrections in Common Use.....	163
Figure 7.5 Reynolds Number Correction Compared to CFD Results for SL2 with Constant Mach Numbers of 0.49 and 0.77.....	164
Figure 7.6 Losses Corrected for Reynolds Number Effects for CFD Test Cases Which Simulated Wind Tunnel Conditions and at Constant Reynolds Number of 600,000	165
Figure 7.7 Comparison of Total Pressure Loss Coefficient in SL2 Cascade With and Without the Proposed Reynolds Number Correction	166

Figure 7.8 Kacker and Okapuu Prediction of Exit Mach Number Effect on Total Pressure Loss Coefficient for Several Values of M_1/M_2	171
Figure 7.9 Kacker and Okapuu Prediction of Exit Mach Number Effect on Total Pressure Loss Coefficient for Several Cascades	172
Figure 7.10 Kacker and Okapuu Prediction of Flow Acceleration Effect on Total Pressure Loss Coefficient for Several Cascades	173
Figure 7.11 Estimate of the Incompressible Limit of the Reynolds Number Corrected Total Pressure Loss Coefficient for HS1C	176
Figure 7.12 Estimation of the Incompressible Limit for HS2 Based on Data from Four Different Wind Tunnels.....	177
Figure 7.13 Ratio of Reynolds Number Corrected Total Pressure Loss Coefficient to Incompressible Limit for the HS2 Cascade from Four Different Wind Tunnels.....	178
Figure 7.14 Variation of Y_{corr} with Mach number for SL2 Showing Onset of Shock Losses	180
Figure 7.15 Evaluation of Compressibility Correction K_P against K_{corr} Indicating Data which Included Shock Losses.....	181
Figure 7.16 Evaluation of Compressibility Correction K_P against K_{corr} Indicating Data from the SL1 and OX Cascades	182
Figure 7.17 Evaluation of Compressibility Correction K_P against K_{corr}	183

Figure A.1 Procedure to Obtain Flow Direction, Static Pressure, and Total Pressure from the Three Hole Probe Calibration (Reproduced from Argüelles Díaz et al. 2009).....	203
Figure A.2 Calibration Curves for C_α at Five Mach Numbers	204
Figure A.3 Calibration Curves for C_{P0} at Five Mach Numbers	204
Figure A.4 Calibration Curves for C_{Ps} at Five Mach Numbers.....	205
Figure B.1 Transducer Calibration Data and Calibration Curves.....	207

List of Symbols

A	Area
A*	Throat area
a	Speed of sound
AVDR	Axial-Velocity-Density Ratio $\left(= \frac{\int_0^1 (\rho_2 V_{ax,2})_{MS} d\left(\frac{y}{s}\right)}{\int_0^1 (\rho_1 V_{ax,1})_{MS} d\left(\frac{y}{s}\right)} \right)$
AVR	Axial-Velocity Ratio $\left(= \frac{\int_0^1 (V_{ax,2})_{MS} d\left(\frac{y}{s}\right)}{\int_0^1 (V_{ax,1})_{MS} d\left(\frac{y}{s}\right)} \right)$
C	True chord length
C _b	Base pressure coefficient $\left(= \frac{P_b - P_o}{0.5 \rho V_o^2} \right)$
C _f	Skin friction coefficient $\left(= \frac{\tau_w}{\frac{1}{2} \rho_e u_e^2} \right)$
C _x	Axial chord length
H	Boundary layer shape factor $\left(= \frac{\delta^{**}}{\theta} \right)$
h	Specific enthalpy or blade span
i	Incidence $\left(= \alpha_1 - \alpha_{1,des} \right)$
k	Turbulent kinetic energy
K _P	Mach number loss correction factor or control system proportional gain
K _I	Control system integral gain
K _D	Control system derivative gain
L _t	Turbulence length scale

M	Mach number $\left(= \frac{u}{a} = \sqrt{\frac{2}{(\gamma-1)} \left(\left(\frac{P_0}{P_s} \right)^{\frac{\gamma-1}{\gamma}} - 1 \right)} \right)$
M_{is}	Isentropic Mach number $\left(= \sqrt{\frac{2}{(\gamma-1)} \left(\left(\frac{P_{01}}{P_s} \right)^{\frac{\gamma-1}{\gamma}} - 1 \right)} \right)$
o	Throat opening
P	Pressure
Q, q	Dynamic pressure $(= P_0 - P_s)$
R_H	Hub radius
R_T	Tip radius
Re	Reynolds number $\left(= \frac{\rho_2 V_2 C}{\mu} \right)$
Re_{θ}	Boundary layer momentum thickness Reynolds number $\left(= \frac{\rho_e V_e \theta}{\mu_e} \right)$
$Re_{\theta t}$	Boundary layer momentum thickness Reynolds number for transition
S	Entropy
s	Pitchwise spacing
t_{TE}	Trailing edge thickness
Tu	Turbulence intensity
u	Velocity
V	Velocity or voltage
x	Axial coordinate
Y	Total pressure loss coefficient $\left(= \frac{P_{01} - P_{02}}{P_{02} - P_2} \right)$
y	Pitchwise coordinate

y^* Non-dimensional distance from wall $\left(= \frac{\rho_w \sqrt{\frac{\tau_w}{\rho_w}} y}{\mu_w} \right)$

Z_w Zweifel blade loading coefficient

Greek

α Flow angle

β Metal angle

γ Specific heat ratio (1.4 for air)

$\Delta\phi^2$ Kinetic energy loss coefficient $\left(= \frac{h_2 - h_{2s}}{h_{02} - h_{2s}} \right)$

δ Unguided turning, Uncertainty

δ^* Boundary layer displacement thickness $\left(= \int_0^{y_e} \left(1 - \frac{\rho u}{\rho_e u_e} \right) dy \right)$

ϵ Trailing edge wedge angle or turbulence eddy dissipation

ζ Stagger angle or energy loss coefficient $\left(= \frac{h_2 - h_{2s}}{h_{02} - h_2} \right)$

η Stage efficiency

θ Boundary layer momentum thickness $\left(= \int_0^{y_e} \frac{\rho u}{\rho_e u_e} \left(1 - \frac{u}{u_e} \right) dy \right)$

μ Dynamic viscosity

ξ Total energy loss coefficient $\left(= \frac{h_{02} - h_{02s}}{h_{02} - h_2} \right)$

ρ Density

τ Shear stress

ω Turbulence eddy frequency

Subscripts

0, T	Total (stagnation) conditions
1	Inlet
2	Outlet
2s	Value at outlet corresponding to no losses
ave	Root-mean-square average
ax	Axial
corr	Corrected to reference Reynolds number
Des	Value at design condition
e	Value at edge of boundary layer
Err	Difference between target and measured value
is	Isentropic
inc	Incompressible limit
M	Mixed-out
MS	Midspan
o	Throat opening
P	Profile
ref	Reference value
S	Static conditions
Target	Desired value for control system to produce
TET	Trailing edge thickness
TH	Theoretical
w	Value at wall or blade surface

Abbreviations

AMDC	Ainley and Mathieson and Dunham and Came
CFD	Computational Fluid Dynamics
DAQ	Data acquisition system
HP	High Pressure
KO	Kacker and Okapuu
LP	Low Pressure
PID	Proportional-Integral-Derivative
PS	Pressure side
SS	Suction side

Chapter 1

Introduction

The design of a gas turbine involves balancing performance, safety, and environmental concerns. This has led engine manufacturers to optimise every component of the engine to maximise efficiency while achieving the power requirements and, especially in the case of aero engines, reducing weight. Modern engines are frequently designed such that the pressure ratio across the turbine causes the flow to reach transonic conditions. In the early stages of design, the axial turbine is optimised through empirical correlations that can predict the performance of the turbine. As the flow physics are better understood, these correlations can be improved, thus allowing better optimisation of the turbines.

Turbomachinery aerodynamics investigations are typically performed with either cascade or cold flow rotating test rigs. While rotating test rigs more closely recreate engine conditions, cascade testing provides many advantages including easier instrumentation and a simpler flow structure. This is especially valuable for studies at midspan, where the flow structures are simpler. Cascade tests are used, among other things, to investigate the effect on losses of different operating conditions such as varying Mach number, Reynolds number or blade incidence.

In addition to experimental studies, modern computational fluid dynamics (CFD) programs are used to gain further understanding of the flow physics within a turbine. Provided the CFD codes are validated against experimental results, the CFD results can also be used to improve the performance correlations.

Carleton University has been conducting experimental and computational studies on axial turbines and developing correlations for many years. For over a decade, these studies have included testing in a high-speed linear cascade wind tunnel. Part of this study has included the design of a new control system for this wind tunnel. This is an intermittent wind tunnel of the blow-down type. Because these studies are focused on the compressibility effects, the new system controls the Mach number.

The present study is concerned with the profile losses measured at the midspan of a turbine cascade for a large range of subsonic Mach numbers. There were two primary goals of this study. The first goal was to develop the improved wind tunnel control system that controls Mach number at the exit of the cascade. The second goal was to evaluate the effect of subsonic compressibility on midspan losses within a turbine blade row. This second goal was achieved through both experimental and CFD investigations. These results were combined with data from the open literature to develop a tentative correlation for the compressibility effects on losses. Because Reynolds number effects were of a similar magnitude to the compressibility effects, a tentative new correlation for Reynolds number effects was also developed. These tentative correlations rely on the simulations for a single

cascade to separate the Reynolds number effects from the compressibility effects, and thus may require further modification before they can be used for general profile loss prediction.

The thesis is divided as follows. Chapter 2 reviews the literature that is most relevant to the present study. The following chapter outlines the experimental apparatus with details on the wind tunnel, instrumentation and the cascade geometry that was tested. Chapter 4 provides details on the improved wind tunnel control system that was developed. A computational study was performed to assist in interpreting the experimental results and to extend the range of test cases outside the capabilities of the experiment. The method and results of these simulations are presented in Chapter 5. The experimental results are presented in Chapter 6. In Chapter 7, the numerical and experimental results are compared to one another as well as to data from the open literature. The cumulative results are then used to develop tentative correlations for the effects of both compressibility and Reynolds number effects on profile losses. Finally, Chapter 8 provides the conclusions of the present study and recommendations for future work.

Chapter 2

Literature Review

2.1 Introduction

The present study is concerned with the effects of compressibility on the losses in axial turbines at subsonic conditions. This chapter reviews the literature pertaining to this study. Because there are a large number of factors which will influence the losses outside of those being investigated, this review will cover several issues that are not directly investigated in this study. First, the flow in an axial turbine is described. This is followed by a discussion of the aerodynamic factors which influence the losses. Finally, the most widely used correlations for predicting the losses are reviewed.

2.2 Description of the Flow in an Axial Turbine

Blade Passage

The flow within a turbine blade passage is complex. Figure 2.1 shows schematically the main features of the flow. The horseshoe vortex is the result of the inlet endwall boundary layer separating around the leading edge of the blade.

The horseshoe vortex has the shape of a horseshoe and has two legs: the pressure-side leg and the suction-side leg. Due to the blade-to-blade pressure gradient within the passage, the pressure-side leg is driven towards the suction side of the adjacent blade. This cross-passage pressure gradient causes the endwall boundary layer to roll up into the passage vortex. Because the passage vortex and pressure-side leg have the same direction of rotation, they merge into one vortex which is referred to as the passage or secondary vortex. In a rotor passage, when tip clearance is present, flow leaks from the pressure side to the suction side of the blade through the small gap between the blade and the tipwall. This leakage flow rolls up into the tip-leakage vortex as it interacts with the flow in the main passage. There is no tip clearance in the cascade used in the present study, and the flow structure on both ends of the blade will have the features shown on the hubwall in Figure 2.1.

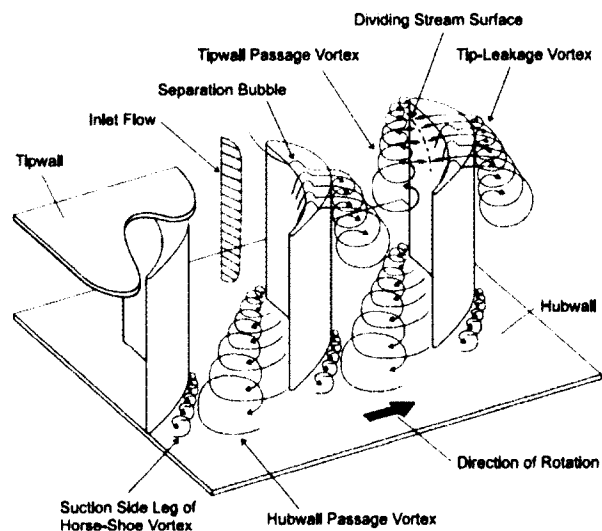


Figure 2.1 Flow Features in an Axial Turbine Blade Passage (Adapted From Jeffries 2000 by Corriveau 2005)

Figure 2.2 illustrates the nomenclature used for the blade and cascade geometry throughout this study. The parameters are defined in Table 2.1. All the angles are measured relative to the axial direction.

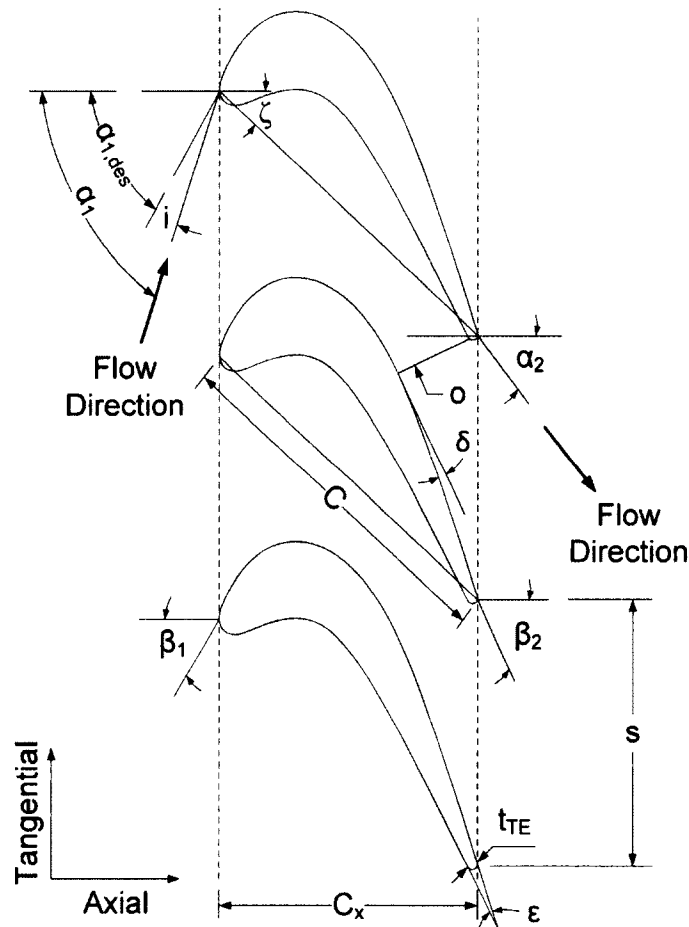


Figure 2.2 Terminology of Turbine Blade and Cascade Geometry

Table 2.1 Nomenclature of Turbine Blade

α_1	Inlet flow angle	C	True chord
$\alpha_{1,des}$	Design inlet flow angle	C_x	Axial chord
α_2	Outlet flow angle	i	Incidence angle
β_1	Inlet metal angle	o	Throat opening
β_2	Outlet metal angle	s	Pitch spacing
ζ	Stagger angle	t_{TE}	Trailing edge thickness
ϵ	Wedge angle	δ	Unguided flow turning

2.3 Decomposition of the Losses for an Axial Turbine Blade Passage

Flow features which reduce the efficiency of a turbomachine are referred to as producing losses. Because most turbomachines are characterised by nearly adiabatic flow, the loss of efficiency in a turbomachine is essentially the result of thermodynamic irreversibilities. Therefore, a discussion of losses in turbomachinery refers to the mechanisms for entropy generation (Denton 1993).

The losses are typically broken down into components based on the source of the losses: usually the components are referred to as profile losses, secondary (or endwall) losses, and tip leakage losses. The components are assumed to be independent, are evaluated separately, and are summed to obtain the resultant overall losses. However, the loss sources are seldom truly independent (Denton 1993). The present study is concerned with the flow at the midspan of a turbine cascade. Therefore, only the profile losses will be considered. Nonetheless, all three loss sources are discussed here briefly.

Profile Losses refer to the entropy generated within the region of two-dimensional flow away from the flow features generated at the endwalls. The profile losses are generated in the blade surface boundary layers and the shock waves that form as the sonic condition is approached. The additional losses due to the sudden expansion at the trailing edge of the blade and subsequent mixing-out of

the flow are also frequently included in the profile losses, although they are sometimes treated separately as trailing edge losses.

Secondary Losses, also known as the endwall losses, refer to the losses generated on the annulus walls as well as the losses due to the mixing of the passage vortex and the suction-side leg of the horseshoe vortex.

Tip-Leakage Losses are the losses associated with the leakage flow between the blade tip and the tipwall. These losses are generated by the viscous flow within the tip gap, mixing of the gap flow with the passage flow, and the mixing-out of the tip-leakage vortex.

2.4 Loss Coefficients

There are several loss coefficients used to indicate the losses in a turbine blade passage. These loss coefficients are defined based on the enthalpy-entropy diagram in Figure 2.3. The most commonly used is the total pressure loss coefficient Y , which is defined as

$$Y = \frac{P_{01} - P_{02}}{P_{02} - P_2} \quad 2.1$$

The total energy loss coefficient ξ , also called the total enthalpy loss coefficient, is also quite common, and is defined as

$$\xi = \frac{h_{02} - h_{02s}}{h_{02} - h_2} \quad 2.2$$

Additionally, the energy or enthalpy loss coefficient ζ , is sometimes seen, and is defined as

$$\zeta = \frac{h_2 - h_{2s}}{h_{02} - h_2} \quad 2.3$$

The kinetic energy loss coefficient $\Delta\phi^2$ is also in use, and is defined as

$$\Delta\phi^2 = \frac{h_2 - h_{2s}}{h_{02} - h_{2s}} = 1 - \frac{V_2^2}{V_{2,is}^2} \quad 2.4$$

All four of these loss coefficients can be expressed in terms of any of the other loss coefficients and the Mach number. Figure 2.4 shows the variation of the loss coefficients with Mach number for air at a constant total pressure loss coefficient of 0.1. This is not intended to suggest the total pressure loss coefficient will be constant with Mach number, but rather to highlight the different trends in the loss coefficients. It is important to note that at the incompressible limit three of these loss coefficients have the same value. Further, of the loss coefficients presented here, the total pressure loss coefficient has the highest value for any given Mach number.

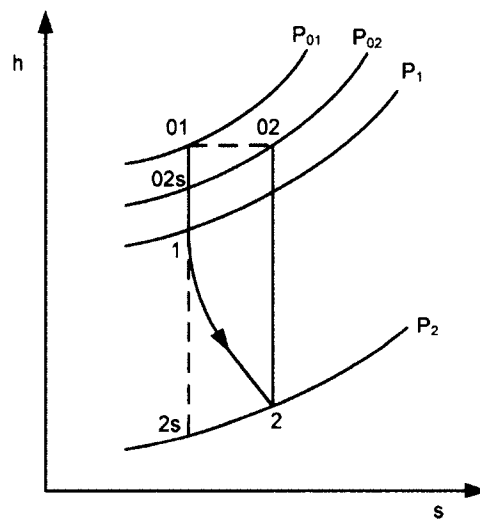


Figure 2.3 Enthalpy-Entropy Diagram for a Turbine Cascade Flow (Denton 1993)

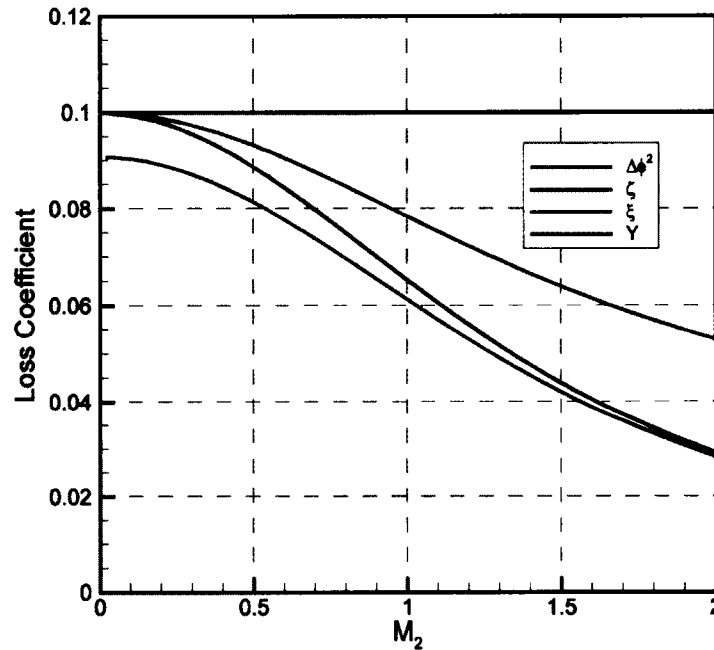


Figure 2.4 Variation of Various Loss Coefficients with Mach Number in Air When Total Pressure Loss Coefficient is 0.1 (Equations 2.1-2.4)

2.5 Aerodynamic Influences on Midspan Losses

2.5.1 Compressibility Effects on Midspan Losses

The effects of compressibility on the losses can be separated into the effect of shock waves within the flow and the effect of density variation within the flow. Both of these effects will be a function of Mach number. Once the flow has choked, that is, the flow has reached the sonic condition at the throat of the blade passage, the inlet Mach number will remain constant while the exit Mach number can continue to rise. For this reason, the compressibility effects within a turbine are mostly correlated with the exit Mach number. However, Kacker and Okapuu (1982) recognise that

shocks can be present in flows with large inlet Mach numbers, and provide a method for predicting losses due to inlet shocks.

Shock waves in a turbine passage affect the losses in two ways. First, losses are produced directly through the entropy rise which occurs across any shock wave. Second, the interaction of the shock wave with the blade-surface boundary layer can have an effect on the behaviour of the boundary layer and thus on its losses. While this study is concerned with subsonic exit Mach numbers, and while shock waves are only present for flows which reach supersonic conditions, shock waves can appear locally in the blade passage for exit Mach numbers as low as 0.6 (Corriveau 2005).

The shock wave-boundary layer interaction has attracted a great deal of attention in analytical and experimental studies due to the difficulty in predicting the effects of shocks on transition and separation. A comprehensive review of this phenomenon can be found in Delery and Marvin (1986). The shock wave-boundary layer interaction occurs when a shock from the trailing edge meets the suction surface of the adjacent blade. Depending on the strength of the shock, it may cause a separation bubble to form, as illustrated in Figure 2.5. If the shock is strong enough, the flow may separate without reattaching, which will result in high losses.

Because this study is focused on the effect of Mach number on midspan performance, a summary of the experimental investigations on this effect has been compiled in Table 2.2.

Table 2.2 Summary of Experimental Investigations on the Effect of Mach Number on Midspan Performance

Author(s)	Type of Test	Steady or Unsteady	Loss Component(s) Investigated	Parameters Varied				Values of Parameters Investigated				Comments or Conclusions
				M	Re	Tu	i (°)	M	Re × 10 ⁻⁵	Tu (%)	i (°)	
Boyle et al. 2002	Turbine Vane; Linear Cascade	Steady	P	✓		✓		0.3 - 0.9		1.0, 10.0	Design	
Carscallen et al. 2009	Linear Cascade	Unsteady	P	✓				0.3 - 1.4		4.0	Design	-blunt trailing edge -study vertical structures and total temperature redistribution
Corriveau and Sjolander 2006	HP Turbine; Linear Cascade	Steady	P	✓	✓		✓	0.5 - 1.3	4.0 - 12.0	0.8	-10 to 10	-3 cascades with different loading -front loading: higher losses
Coton et al. 2001	LP Turbine; Linear Cascade	Steady	P	✓	✓			0.6 - 0.9	1.9 - 6.8		Design	-study influence of solidity
Haller and Camus 1984	HP Turbine Rotor; Linear Cascade	Steady	P	✓				0.9 - 1.25	8.5	0.5	Design	-study film cooling penalty on performance
Hoheisel et al. 1987	Linear Cascade	Steady	P	✓	✓	✓	✓	0.3 - 0.95	1.0 - 11.0	0.8, 2.7, 5.1, 7.1	-38 to 12	-study loading influence on loss -aft loading: lower losses
Jeffries 2000	Linear Cascade	Steady	P	✓			✓	0.5 - 1.2		4.0	-10 to 15	-same blade profile as Kiock et al. (1986)
Jouini et al. 2002	HP Turbine; Linear Cascade	Steady	P	✓			✓	0.5 - 1.25		4.0	-10 to 14	-study influence of inlet metal angle
Kiock et al. 1986	Linear Cascade	Steady	P	✓				0.3 - 1.3			Design	-same profile tested in four different wind tunnels
Li et al. 2002	Steam Turbine; Linear Cascade	Steady	P	✓			✓	0.4 - 1.15			-25 to 35	-propose modified shock correlation
Mee et al. 1992	Linear Cascade	Steady	P	✓	✓			0.6 - 1.2	5.0 - 20.0	4.1	Design	-investigate contribution of different loss components
Moustapha et al. 1993	Turbine Vane; Linear Cascade	Steady	P,S	✓				0.3 - 1.3			Design	-cascade with low aspect ratio (h/c = 0.64)
Perdichizzi 1990	Steam Turbine Rotor; Linear Cascade	Steady	P,S	✓				0.2 - 1.6			Design	
Song et al. 2007	Steam Turbine; Linear Cascade	Steady	P	✓	✓		✓	0.2 - 0.8	1.8 - 9.0	2.0	-60 to 35	-3 cascades with different solidity
Štátný et al. 1997	Linear Cascade	Steady	P	✓			✓	0.6 - 1.5			-70 to 30	
Zhang et al. 2005	Turbine Vane; Linear Cascade	Steady	P	✓		✓		0.4 - 0.7		1.7, 5.4, 8.2	Design	-wakes more sensitive to turbulence intensity at low Mach numbers

Abbreviations: P: Profile Loss i: Incidence Re: Reynolds Number
 S: Secondary Loss M: Mach Number Tu: Turbulence Intensity

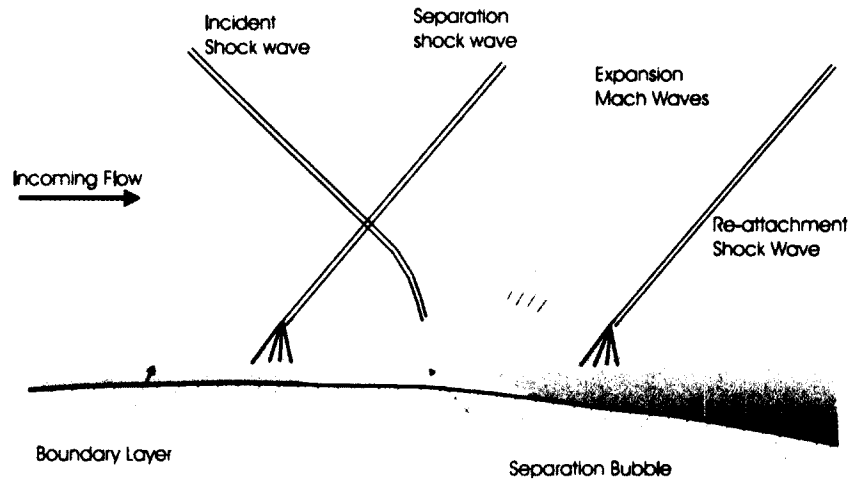


Figure 2.5 Shock Wave-Boundary Layer Interaction (Adapted from Japikse and Baines 1994 by Corriveau 2005)

In addition to shock waves, compressibility effects also affect the losses through the density variation in the flow, as mentioned above. These effects will affect the losses by altering the growth of the boundary layer and by modifying the mixing process. These effects are of importance to this study, since they will be the cause of any changes to the losses due to compressibility effects even in the absence of shocks.

The losses in the boundary layer can be related to shear stress, as this will be the source of entropy generation due to viscous friction. Specifically, Denton (1993) derives an expression for the local rate of entropy creation per unit volume within a two-dimensional boundary layer as

$$\dot{S}_v = \frac{1}{T} \tau \frac{dV}{dy} \quad 2.5$$

Denton (1993) interprets this as the viscous shear work, $\tau dV/dy$, being converted to heat at temperature T . The shear stress is often indicated with the skin friction coefficient which is

$$C_f = \frac{\tau_w}{\frac{1}{2}\rho_e u_e^2} \quad 2.6$$

where τ_w = wall shear stress
 ρ_e = density at edge of boundary layer
 u_e = velocity at edge of boundary layer

Denton (1993) indicates that the skin friction, and hence entropy generation, will not be greatly affected by the Mach number in the range common to turbomachines, $0 < M < 2$. This is supported by the results of Van Driest (1952) which show that the skin friction coefficient will decrease by about 3% as Mach number increases from 0 to 2 for a laminar boundary layer in zero pressure gradient.

The process of mixing will be affected by compressibility, even if only due to the fact that any density variation in the flow will contribute to mixing as well as the velocity variation. Mee et al. (1992) made an effort to isolate the losses due to mixing downstream of the blade for a test cascade, as shown in Figure 2.6, and found that the mixing kinetic energy loss coefficient increased to a Mach number of about 0.9, decreased briefly near the sonic outlet condition, and then rose steadily for higher Mach numbers. It should be noted that a decrease in loss coefficient may not necessarily correspond to a decrease in entropy generation; where the loss coefficient is decreasing, the losses may still be increasing due to increasing velocity.

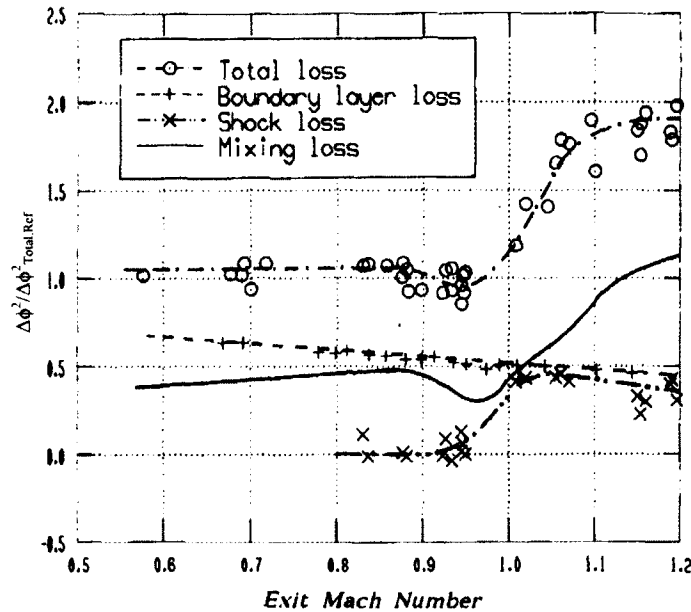


Figure 2.6 Variation of Midspan Kinetic Energy Loss Components with Mach Number for a Test Cascade (Mee et al. 1992)

2.5.2 Base Pressure Influence on Trailing Edge Losses

Using a simplified control volume analysis for incompressible flow, Denton (1993) determined that the losses due to mixing of the profile flow downstream of the trailing edge can be expressed as

$$Y_{TET} = -\frac{C_b t_{TE}}{o} + \frac{2\theta}{o} + \left(\frac{\delta^* + t_{TE}}{o}\right)^2 \quad 2.7$$

where $C_b = \frac{P_b - P_o}{0.5\rho V_o^2}$ = base pressure coefficient

θ = boundary layer momentum thickness

δ^* = boundary layer displacement thickness

t_{TE} = trailing edge thickness

o = throat opening

While this equation is only valid for incompressible flows, it highlights the primary parameters on which the trailing edge losses will depend. The first term represents the losses due to the base pressure at the trailing edge, the second term represents the losses due to the mixing out of the boundary layers, and the third term represents the losses from the sudden expansion of the flow in the trailing edge region. The losses due to the base pressure are associated with the separation and subsequent mixing of the pressure and suction side streams at the trailing edge of the blade.

While various analytical techniques have been developed to predict the boundary layer properties, the base pressure is usually predicted based on empirical data. Perhaps the most well known correlation for predicting the base pressure was developed by Sieverding et al. (1980). This correlation is a function of the downstream static pressure, trailing edge wedge angle ϵ , and the unguided turning downstream of the throat δ . This correlation can be seen in Figure 2.7. Alternatively, Denton and Xu (1990) suggest that an inviscid Euler solver will provide a good estimate of base pressure.

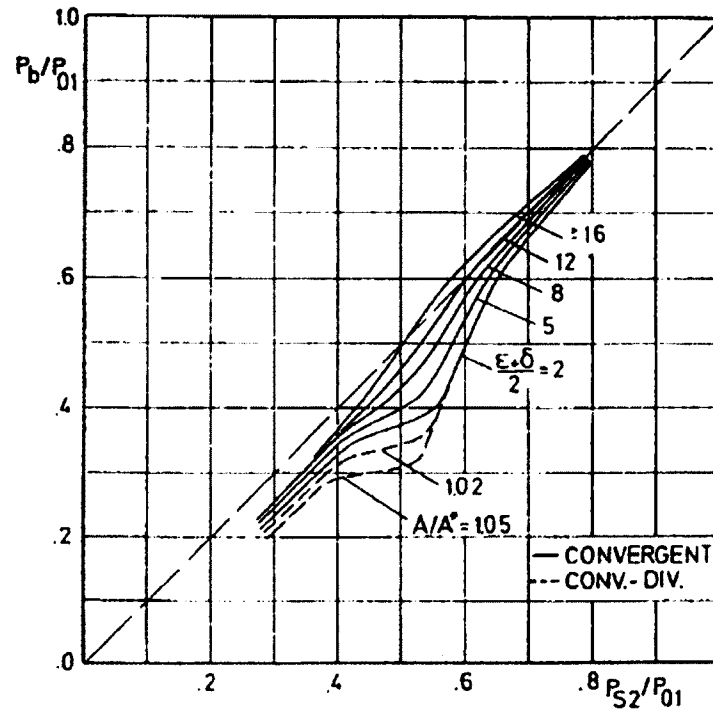


Figure 2.7 Base Pressure Correlation (Sieverding 1980)

2.5.3 Influence of Reynolds Number on Midspan Losses

The Reynolds number, which indicates the ratio of the inertial forces to the viscous forces, is defined throughout this study based on the exit flow conditions and the true chord of the blade $\left(Re_2 = \frac{\rho_2 V_2 C}{\mu}\right)$. This is the same definition of Reynolds number used in the loss correlation developed by Kacker and Okapuu (1982). The effects of Reynolds number on losses have been studied by many researchers. Typical variation in the total pressure loss coefficient can be seen in Figure 2.8.

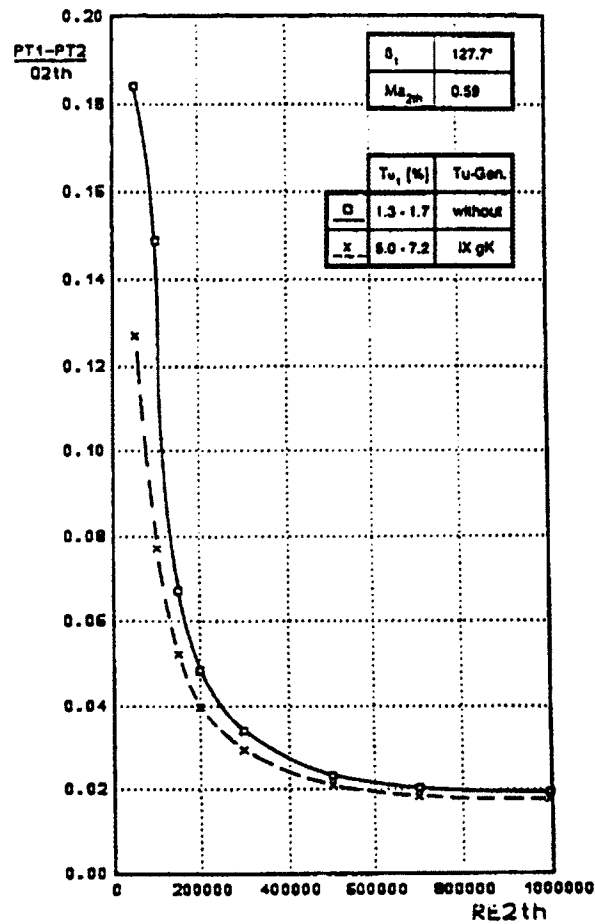


Figure 2.8 Variation of Total Pressure Losses with Reynolds Number (Ladwig and Fottner 1993 as Reproduced by Jeffries 2000)

While an increase in Reynolds number might be expected to decrease the losses simply by nature of the viscous forces becoming less dominant, the Reynolds number effect on losses is mostly attributed to the movement of the transition location as discussed by Hourmouziadis (1989) and Mayle (1991). At high Reynolds numbers, well above those seen in Figure 2.8, transition occurs near the leading edge, and there may be turbulent separation near the trailing edge which will produce mixing losses in addition to the losses generated in the shear layer. As the

Reynolds number is decreased, turbulent separation disappears and the transition location moves towards the trailing edge. The movement of the transition location will reduce the losses as less of the blade surface boundary layer is turbulent. The losses will be at a minimum in this range of Reynolds numbers where there is no separation. As the Reynolds number is decreased, the transition location will move beyond the laminar separation point and a separation bubble will form. This separation bubble will have the effect of increasing the losses. As the Reynolds number is further reduced, the transition location, and thus the reattachment point of the separation bubble, will move towards the trailing edge. The losses will increase as the size of the separation bubble increases. As the transition location moves towards the trailing edge, it will reach a point where the separated flow cannot reattach. This will result in a dramatic increase in the losses.

2.5.4 Influence of Free-Stream Turbulence on Midspan Losses

In an engine, the turbulence intensities can be large. For example, Binder et al. (1989) measured midspan turbulence intensities up to 8.0% in a multistage low-pressure (LP) turbine. The turbulence levels will be even higher in a high-pressure (HP) turbine immediately after the combustor. Many studies have investigated the effect of turbulence intensity on the performance of a turbine blade. The results from Hoheisel et al. (1987), shown in Figure 2.9, demonstrate the loss behaviour with Reynolds number and turbulence intensity. In particular, Figure 2.9 shows that the losses increase with turbulence intensity only in the higher range of Reynolds

numbers. At low Reynolds numbers around 100,000, for the cascades in Figure 2.9, the turbulence intensity does not show any clear influence on the losses. Studies such as those performed by Mayle (1991) indicate that the effect of the turbulence intensity on the boundary layer is to change the Reynolds number at which transition occurs.

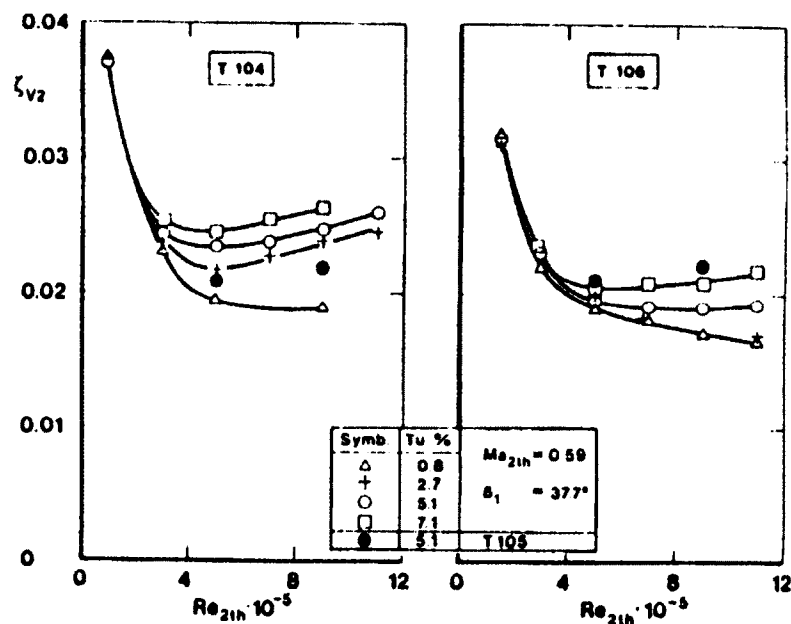


Figure 2.9 Energy Loss Variation with Reynolds Number at Different Freestream Turbulence Intensities for Blade Profiles T104, T105, and T106 (Hoheisel et al. 1987 as Reproduced by Corriveau 2005)

2.5.5 Axial-Velocity-Density Ratio (AVDR)

The Axial-Velocity-Density-Ratio (AVDR) is often used to quantify the level of two-dimensionality of the flow through a blade row. It is defined as

$$AVDR = \frac{\int_0^1 (\rho_2 V_{ax,2})_{MS} d\left(\frac{y}{S}\right)}{\int_0^1 (\rho_1 V_{ax,1})_{MS} d\left(\frac{y}{S}\right)} \quad 2.8$$

The AVDR represents the ratio of the mass flow rate per unit span at the blade exit to that at the inlet. Hence it is a measure of the average contraction or expansion of a streamtube at midspan. In two-dimensional flow, the AVDR will be equal to 1.0. However, because the AVDR is an average measure, an AVDR of 1.0 does not necessarily mean the flow is two-dimensional. If the flow at midspan has regions of contraction as well as expansion in the spanwise direction, the AVDR may equal 1.0, despite the flow not being two-dimensional.

There is relatively little published work focused on the effect of AVDR on turbine performance. Rodger et al. (1992) examined the influence of AVDR under incompressible conditions, referred to as Axial-Velocity Ratio (AVR) since the density is constant. Figure 2.10 shows their results, which show that losses decrease with increasing AVR. For compressible flows, Kiock et al. (1986) concluded that AVDR did not affect the losses between values of AVDR of 0.9 and 1.0 for the cascade in their study.

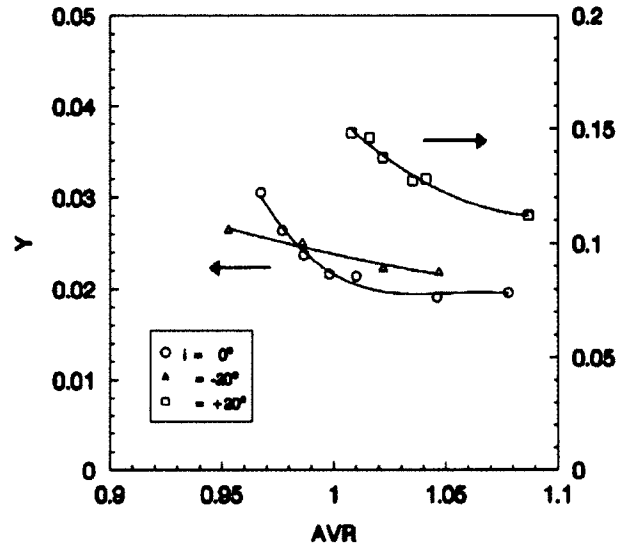


Figure 2.10 Variation of Losses with AVR (Rodger 1992)

2.6 Correlations for Profile Loss Prediction at Design Incidence

2.6.1 Ainley and Mathieson Loss System

The Ainley and Mathieson (1951) turbine loss system is of particular importance since it is the foundation of most loss correlation methods in use today. The Ainley and Mathieson method provides a prediction of all sources of loss in an axial turbine: profile losses, secondary losses and tip leakage losses at both design and off-design incidence. This review focuses on the profile loss prediction at design incidence, since this study is concerned with the midspan performance at design incidence.

The Ainley and Mathieson profile loss prediction is based on the two extreme cases of flow acceleration for the same outlet angle, namely a nozzle blade ($\beta_1=0$) which has maximum acceleration, and an impulse blade ($\beta_1=\alpha_2$) which has zero acceleration. The total pressure loss coefficient for nozzle blades and impulse blades are shown in Figures 2.11 and 2.12 respectively. For an arbitrary inlet angle between the two extremes, a weighted average is used

$$Y_{P,AM} = \left(Y_{P(\beta_1=0)} + \left(\frac{\beta_1}{\alpha_2} \right)^2 (Y_{P(\beta_1=0)} - Y_{P(\beta_1=\alpha_2)}) \right) \left(\frac{t_{max}/c}{0.2} \right)^{\frac{\beta_1}{\alpha_2}} \quad 2.9$$

where $Y_{P(\beta_1=0)}$ = profile loss coefficient for a nozzle blade,

$Y_{P(\beta_1=\alpha_2)}$ = profile loss coefficient for an impulse blade

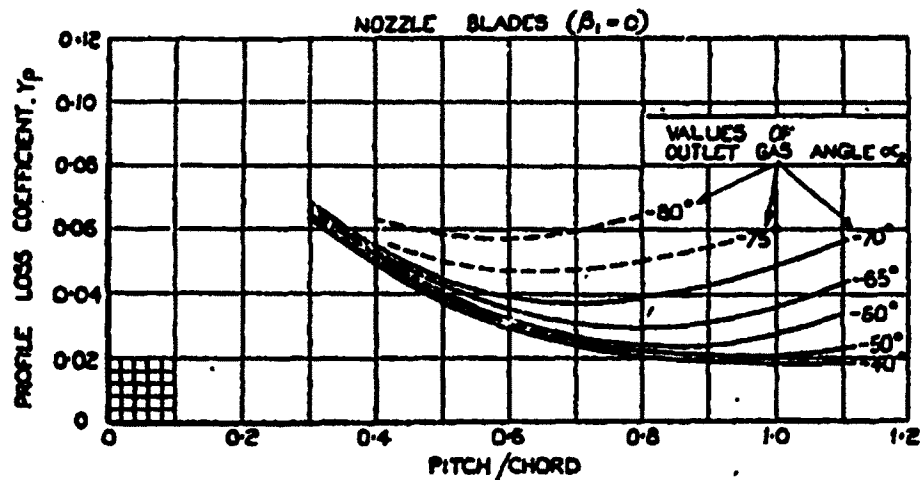


Figure 2.11 Predicted Loss Coefficient for Nozzle Blades (Ainley and Mathieson 1951)

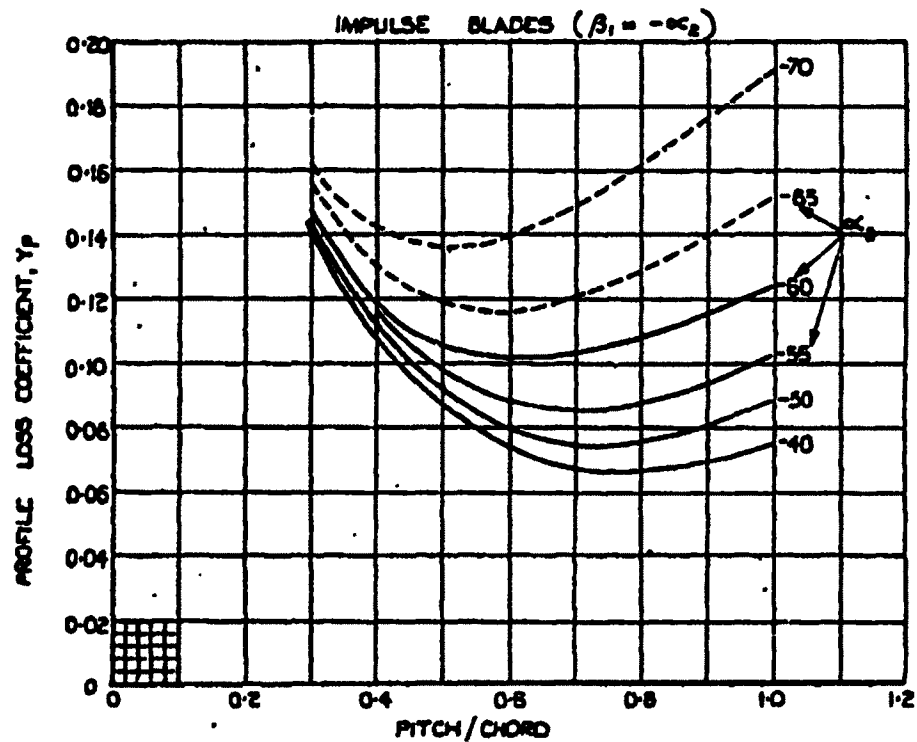


Figure 2.12 Predicted Loss Coefficient for Impulse Blades (Ainley and Mathieson 1951)

Equation 2.9 is based on the performance of blade profiles with a trailing edge thickness equal to 2 percent of the blade pitch and tested at a Reynolds number of 200,000, at Mach numbers below 0.6. Ainley and Mathieson suggest that the effects of trailing edge thickness be corrected with the factor presented in Figure 2.13. Further, it is suggested that Reynolds number effects will cause the loss in stage efficiency ($1-\eta$) to vary as $Re^{-1/5}$. The Ainley and Mathieson method assumes the total pressure loss coefficient will not be influenced by the exit Mach number.

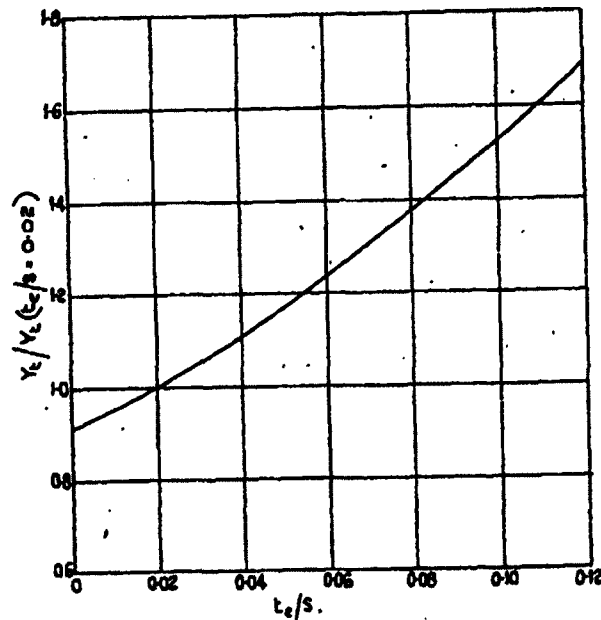


Figure 2.13 Trailing Edge Correction Factor (Ainley and Mathieson 1951)

2.6.2 Modifications to the Ainley and Mathieson System due to Dunham and Came

The loss prediction method of Ainley and Mathieson was improved by Dunham and Came (1970). This improved method is frequently referred to as the AMDC correlation. Dunham and Came made two modifications to the profile loss prediction: a new Reynolds number correction and a supersonic Mach number correction. The Reynolds number correction consists of multiplying the predicted losses from Equation 2.9 by the factor $\left(\frac{Re}{200,000}\right)^{-0.2}$. Note that this factor is applied to the loss coefficient, rather than the loss in stage efficiency $(1-\eta)$. The Mach number correction, applied when the exit Mach number exceeds 1.0, is intended to

capture the losses generated by shock waves in supersonic flow. This correction consists of multiplying the predicted losses from Equation 2.9 by

$$K_C = 1 + 60(M_2 - 1)^2 \quad 2.10$$

2.6.3 Modifications to the Ainley and Mathieson System due to Kacker and Okapuu

The AMDC loss system was further improved by Kacker and Okapuu (1982). There are five modifications to the profile loss prediction in the Kacker and Okapuu system. The trailing edge losses are predicted separately from the profile losses. For this reason, the profile losses predicted by the AMDC loss system are multiplied by 0.914 to remove the effects of trailing edge thickness. The Reynolds number correction is updated in the Kacker and Okapuu system. As well, a subsonic compressibility correction is introduced in this loss system. Also, the interpolation method between the impulse and nozzle blade losses is modified. Finally, the profile losses are multiplied by a factor of 2/3 to reflect the improvements in aerodynamic design over the three decades between the Ainley and Mathieson correlation and the Kacker and Okapuu correlation. The Kacker and Okapuu profile loss prediction is

$$Y_{P,KO} = 0.914 \left(\frac{2}{3} Y_{P,AMDC} K_P + Y_{SHOCK} \right) f(Re) \quad 2.11$$

where

$$Y_{P,AMDC} = \left(Y_{P(\beta_1=0)} + \left| \frac{\beta_1}{\alpha_2} \right| \left(\frac{\beta_1}{\alpha_2} \right) (Y_{P(\beta_1=0)} - Y_{P(\beta_1=0)}) \right) \left(\frac{t_{max}/c}{0.2} \right)^{\frac{\beta_1}{\alpha_2}} \quad 2.12$$

$f(Re)$ = the correction for Reynolds number

Y_{SHOCK} = the losses generated by shocks at the leading edge of the blade

K_p = the correction for subsonic Mach number

The trailing edge losses are predicted in a similar manner to the profile losses where separate curves are predicted for the extreme cases of impulse blades and nozzle blades, and the predicted losses are interpolated from these extremes. The predicted trailing edge energy loss coefficient for nozzle and impulse blades are shown in Figure 2.14. The interpolation of these curves is provided by

$$\Delta \phi_{TET}^2 = \left(\Delta \phi_{TET(\beta_1=0)}^2 + \left| \frac{\beta_1}{\alpha_2} \right| \left(\frac{\beta_1}{\alpha_2} \right) (\Delta \phi_{TET(\beta_1=\alpha_2)}^2 - \Delta \phi_{TET(\beta_1=0)}^2) \right) \quad 2.13$$

In compressible flow, the energy loss coefficient can be converted to the total pressure loss coefficient using

$$Y_{TET} = \frac{\left(1 - \frac{\gamma-1}{2} M_2^2 \left(\frac{1}{1 - \Delta \phi_{TET}^2} - 1 \right) \right)^{-\left(\frac{\gamma}{\gamma-1}\right)} - 1}{1 - \left(1 + \frac{\gamma-1}{2} M_2^2 \right)^{-\left(\frac{\gamma}{\gamma-1}\right)}} \quad 2.14$$

In incompressible flow, Equation 2.14 reduces to

$$Y_{TET} = \frac{1}{1 - \Delta \phi_{TET}^2} - 1 \quad 2.15$$

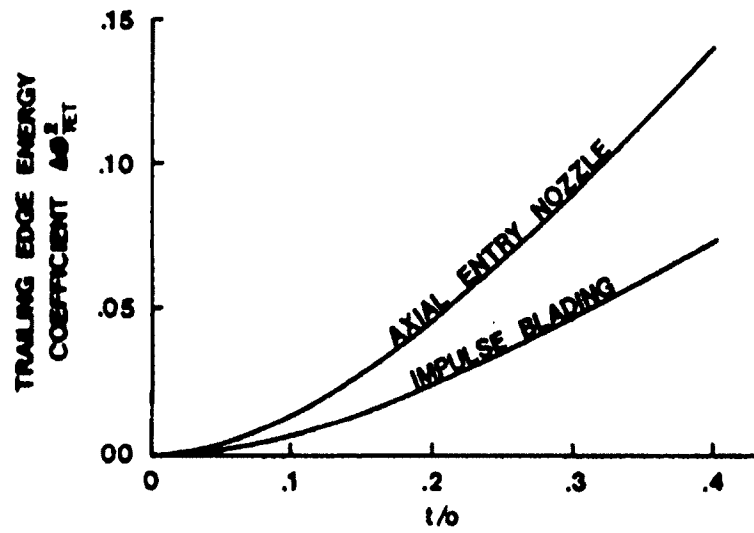


Figure 2.14 Trailing Edge Energy Loss Coefficient (Kacker and Okapuu 1982)

The Reynolds number correction in the Kacker and Okapuu correlation is varied depending whether the suction side flow is expected to be primarily laminar, transitional, or turbulent. The Reynolds number independence in the transitional regime is an approximation to the complex loss coefficient variation in this range.

The Reynolds number correction is

$$f(Re) = \begin{cases} \left(\frac{Re}{2 \times 10^5}\right)^{-0.4} & , Re \leq 2 \times 10^5 \\ 1 & , 2 \times 10^5 < Re \leq 10^6 \\ \left(\frac{Re}{10^6}\right)^{-0.2} & , Re > 10^6 \end{cases} \quad 2.16$$

The subsonic compressibility correction is divided into two parts. The first is the inlet shock loss prediction. This loss can arise at relatively low inlet Mach numbers due to the high acceleration around the leading edges. Because the inlet Mach numbers tend to be highest at the hub, the inlet shock prediction is based on the Mach number at the hub. The shock loss at the hub is predicted to be

$$\left(\frac{\Delta P_0}{q_1}\right)_{HUB} = 0.75(M_{1,HUB} - 0.4)^{1.75}, M_{1,HUB} > 0.4 \quad 2.17$$

Since this loss is concentrated around the hub, a longer blade will be less affected.

To correct for this, the average shock loss for the blade is taken to be

$$\left(\frac{\Delta P_0}{q_1}\right)_{SHOCK} = \left(\frac{R_H}{R_T}\right) \left(\frac{\Delta P}{q_1}\right)_{HUB} \quad 2.18$$

Finally, since this prediction is based on the inlet dynamic pressure, the total pressure loss coefficient, which is based on the outlet dynamic pressure, can be obtained with

$$Y_{SHOCK} = \left(\frac{\Delta P}{q_1}\right)_{SHOCK} \left(\frac{P_1}{P_2}\right) \frac{1 - \left(1 + \frac{\gamma - 1}{2} M_1^2\right)^{\frac{\gamma}{\gamma - 1}}}{1 - \left(1 + \frac{\gamma - 1}{2} M_2^2\right)^{\frac{\gamma}{\gamma - 1}}} \quad 2.19$$

The second part of the subsonic compressibility correction is intended to correct for the effects of channel flow acceleration. In particular, the increased acceleration at higher Mach numbers was seen to cause suppression of local separations and thinning of boundary layers. The Mach number correction, applied when the exit Mach number is greater than 0.2, is

$$K_P = 1 - \left(\frac{M_1}{M_2}\right)^2 (1.25(M_2 - 0.2)) \quad 2.20$$

Since the present study is concerned with evaluating and improving the prediction of losses in subsonic flow, this correction is of particular importance. It is also important to note that K_P will take a value of zero when both M_1/M_2 and M_2 have a value of 1, that is for an impulse blade with a choked outlet flow. This is illustrated in Figure 2.15. As seen from Equation 2.11, this has the effect of predicting zero

profile losses for the impulse turbine geometry. This is clearly incorrect. While the impulse geometry is not normally used in gas turbine engines, it is physically realisable. It is obviously undesirable to have a correlation that gives erroneous results at a condition that is unlikely to occur but is nevertheless physically realisable. In Chapter 7, the subsonic Mach number correction, Equation 2.20 is investigated further and an attempt is made to develop an improved correction.

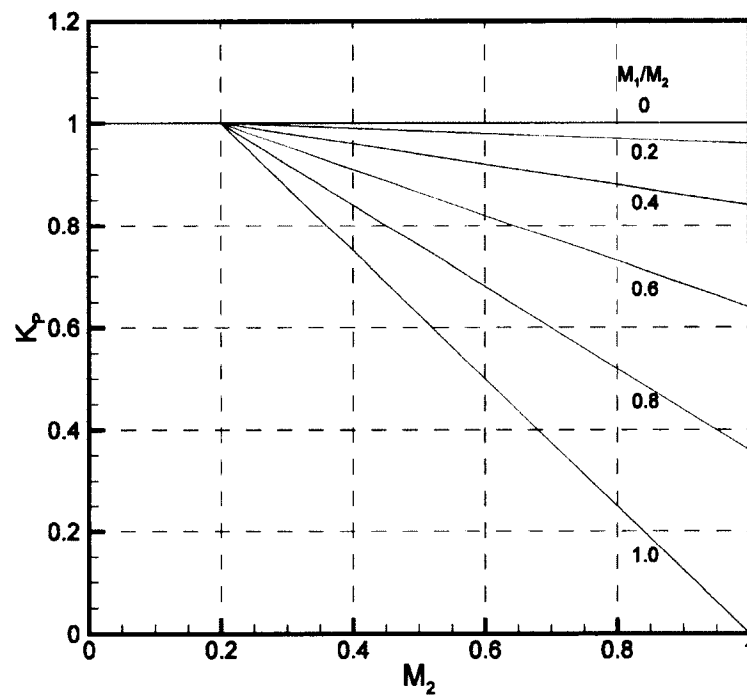


Figure 2.15 Variation of K_p with M_2 for Several Values of M_1/M_2

Chapter 3

Experimental Set-up and Measurement

Methods

3.1 Introduction

This study uses the Pratt & Whitney Canada high speed wind tunnel, shown in Figure 3.1. This is a blow-down type of wind tunnel used for transonic turbine cascade research. The wind tunnel has been described in detail by Corriveau (2005). While this chapter describes the wind tunnel and the details of the changes made to the set-up, the interested reader should refer to Corriveau (2005) for a more general description. The changes that have been made include the addition of a probe calibration rig, the simultaneous use of eleven pressure transducers instead of one pressure transducer in a multiplexer, the replacement of the data acquisition system, and the implementation of the new control system based on Mach number designed in this study. The design of this new control system is described in detail in Chapter 4. This chapter also describes the cascade tested in this study. This

cascade has been designated SL2 since it was originally used in a study on secondary losses.

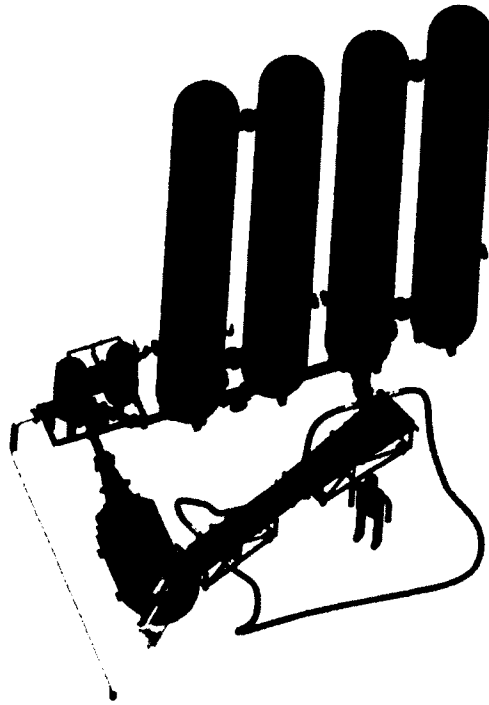


Figure 3.1 High Speed Wind Tunnel

3.2 High Speed Wind Tunnel

3.2.1 Air Supply

The wind tunnel air tanks are pressurised by a Broom-Wade model VC500 two-stage intercooled positive displacement compressor capable of providing air pressurised to about 690kPa (100psi(g)). At the exit of the compressor, the air is passed through a reversed flow aftercooler to bring the air temperature from above

100°C to about 27°C. The air is then passed through a water separator to remove the excess moisture.

As the air in the tanks is discharged through the test section, the temperature of the air in the tanks, and thus the total temperature in the test section, decreases continuously due to the expansion. Additionally, the air is accelerated through the cascade, further reducing the static temperature of the air. If the static temperature falls below the dew point of the air, condensation will occur. This can cause condensation shocks within the blade passages which are undesirable. Because of this, the compressed air must be dried before being sent to the tanks. This is accomplished with a Comp-Air Kellogg model CDH520 regenerative desiccant dryer which reduces the dew point of the air to below -45°C. This will prevent the formation of condensation up to a Mach number of 1.2.

Once the air has been pressurised and dried, it is sent to the air storage tanks. There are two sets of two storage tanks as seen in Figure 3.2. The four tanks have a combined volume of about 26m³.

Two control valves and two shutoff valves are placed as shown in Figure 3.2 to control the air flow from the tanks into the cascade test section and the probe calibration rig. The shutoff valves are 15.2cm (6in) butterfly valves that are opened and closed by pneumatic actuators. The control valves are 10.16cm (4in) and 5.08cm (2in) ball valves for the cascade test section and probe calibration rig respectively. The control valves are discussed in further detail in Section 4.2.5.

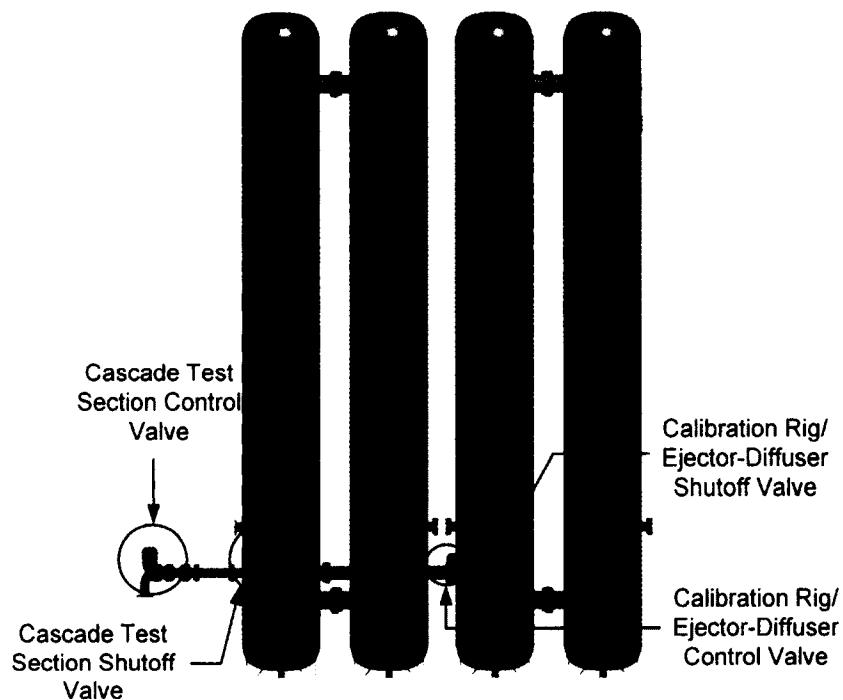


Figure 3.2 Air Storage Tanks and Location of Control and Shutoff Valves

3.2.2 Cascade Test Section

The cascade test section and ejector-diffuser assembly are shown in Figure 3.3. The test section is shown in greater detail in Figure 3.4. The ejector-diffuser assembly can be used to control the downstream static pressure, and thus the downstream Reynolds number, independently of the Mach number. The ejector system was not used in this study. Because the diffuser exhausts to atmospheric pressure, the static pressure downstream of the cascade will be below atmospheric.

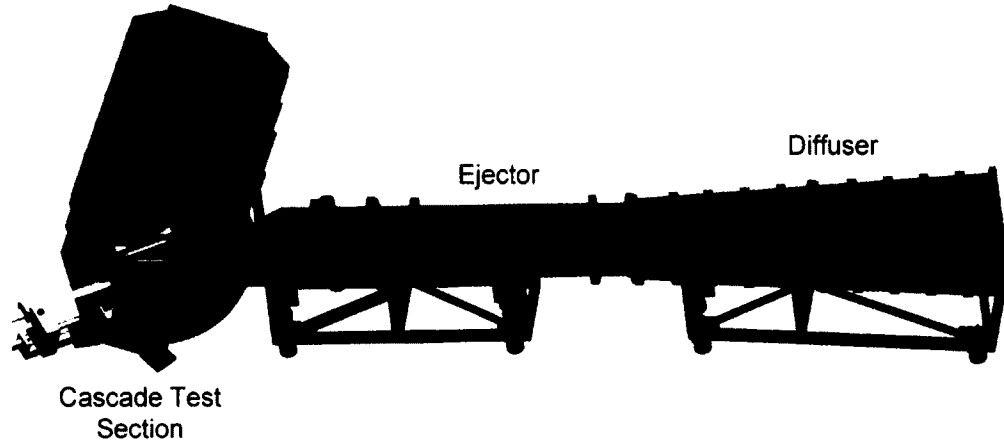


Figure 3.3 Cascade Test Section and Ejector-Diffuser

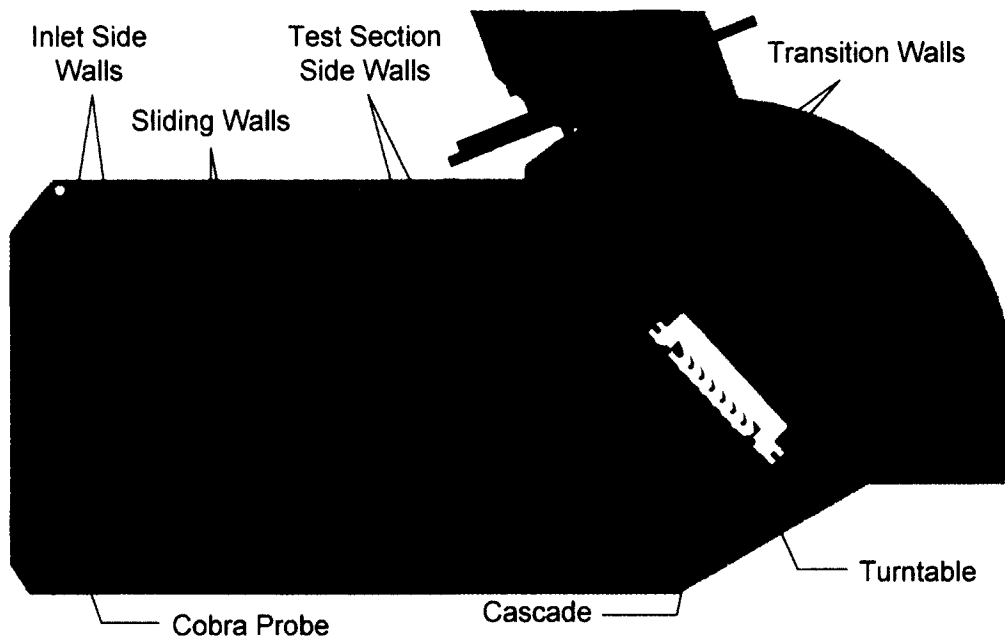


Figure 3.4 Cascade Test Section

The turntable allows the incidence of the cascade to be varied. The turntable which is mounted on a worm and gear can be rotated to yield incidence angles of $\pm 20^\circ$. While incidence of the cascade was not varied in this study, the turntable allows the inlet angle to be set to within $\pm 0.5^\circ$ using a protractor.

With the new wind tunnel control system outlined in Chapter 4, the range of possible Mach numbers is from 0.1 to about 1.3. For a cascade with a chord of 25.4mm, this Mach number range results in Reynolds numbers between 100,000 and 1,000,000 when the ejector system is not in use. In this study, the Mach number is varied between 0.2 and 1.0. Typically, the cascades tested in this facility have chords between 25mm and 40mm, while the blade span is fixed at 61mm.

3.2.3 Probe Calibration Rig

The probe calibration rig is a new addition to the laboratory since it was last detailed by Corriveau (2005). This calibration rig, shown in Figure 3.5, is used to generate the characteristics of a probe at pitch and yaw angles from -30° to 30° at subsonic Mach numbers, as outlined in Appendix A.

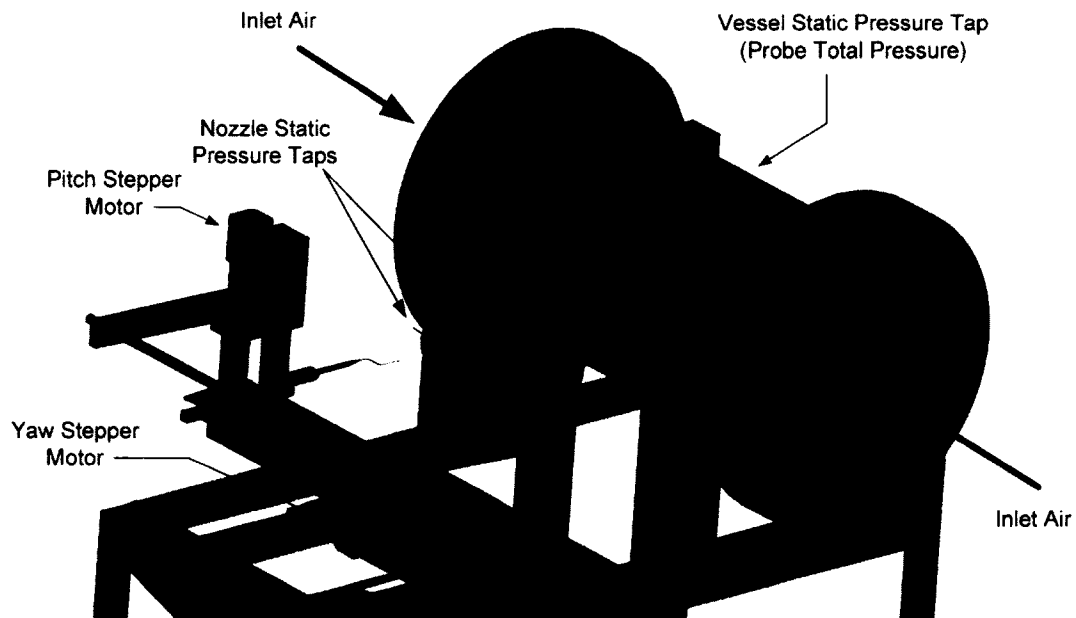


Figure 3.5 Probe Calibration Rig

Currently, the calibration rig is equipped with a contracting nozzle and thus it is possible to calibrate probes at subsonic Mach numbers only. Steady calibration jets have been demonstrated for Mach numbers from 0.2 to 0.94.

The calibration rig is capable of rotating a probe in both pitch and yaw directions by up to $\pm 30^\circ$. This is accomplished with two Vexta PK245-01AA stepper motors which are capable of 1.8° steps which are geared down to steps of 0.01° with a Velmex A5990TS rotary table. Because the steps are geared down, backlash in the stepper motor is essentially negligible. Typical backlash in this model of rotary table is about $3'20''$ (0.056°). Because this study used a three-hole probe which can only determine the angle in one direction, only the yaw motion was needed to calibrate the probe. However, the capability of both pitch and yaw calibration is present for probes that require calibration in both directions such as seven-hole pressure probes.

The calibration rig receives air from the same hoses that can be used for the ejector system. The air in the settling chamber exhausts to the laboratory through a contracting nozzle with a bellmouth inlet. Because the hoses face one another within the settling chamber, the turbulence level of the calibration rig is expected to be significant, although the turbulence intensity has not been measured at high Mach numbers. Preliminary measurements using a normal-wire anemometer suggest the turbulence intensity is about 2% at Mach numbers of 0.5 (Scribner 2011). The turbulence level in the cascade testing is also expected to be fairly high: Corriveau (2005) measured turbulence intensities of 3.5% to 3.8% in the inlet flow

to the cascade. The total pressure of the calibration rig is measured with the static tap on the top of the settling chamber. This static pressure is corrected to the total pressure of the calibration jet based on the centre hole of the three-hole probe when the probe is aligned with the flow. The static pressure of the air flow produced by the calibration rig is measured on either side of the probe using the static taps noted on Figure 3.5.

3.3 Instrumentation

3.3.1 Pressure Transducers

Eleven Druck PDCR 22 pressure transducers are used for all the pressure measurements in the wind tunnel. The use of eleven transducers allows for simultaneous measurements which removes the need for a Scanivalve multiplexer as used by Corriveau (2005). These transducers have a variety of ranges, as summarised in Table 3.1. The transducers are calibrated at least once a year with a Druck DPI 605 Pressure Calibrator using the procedure outlined in Appendix B. This calibration relates the voltage output by the transducers to a pressure through a linear correlation.

Table 3.1 Ranges of the Transducers Used in This Study

Designation	Serial Number	Range (psi)	Differential/Absolute
Ch1	134061	100	Differential
Ch2	B6228	50	Differential
Ch3	82842/834	50	Differential
Ch4	114370	50	Differential
Ch5	B6992	100	Differential
Ch6	B3116	75	Differential
Ch7	76741	100	Absolute
Ch8	76740	100	Absolute
Ch9	134060	100	Differential
Ch10	B6202	100	Differential
Ch11	76738	50	Absolute

3.3.2 Three-Hole Probe

The pressure measurements downstream of the cascade are taken with the three-hole probe documented by Islam (1999). By using a three-hole probe the flow direction can be determined in addition to the total and static pressures from the yaw coefficient C_α , total pressure coefficient C_{P_0} , and static pressure coefficient C_{P_s} .

These coefficients are defined as

$$C_\alpha = \frac{P_2 - P_3}{P_1 - \bar{P}} \quad 3.1$$

$$C_{P_0} = \frac{P_0 - P_1}{P_1 - \bar{P}} \quad 3.2$$

$$C_{P_s} = \frac{P_0 - P_s}{P_1 - \bar{P}} \quad 3.3$$

where

$$\bar{P} = \frac{P_2 + P_3}{2} \quad 3.4$$

The values of these coefficients are determined for this probe at several subsonic Mach numbers and yaw angles between $\pm 15^\circ$ with the calibration procedure outlined in Appendix A. Because the probe calibration rig is currently unable to operate at supersonic Mach numbers, a normal shock correction was applied to the total pressure measured by the three-hole probe for Mach numbers greater than one. The dimensions of this probe are shown in Figure 3.6. The width of the probe tip is 1.37 mm which corresponds to 4.0% of the spacing of the SL2 cascade.

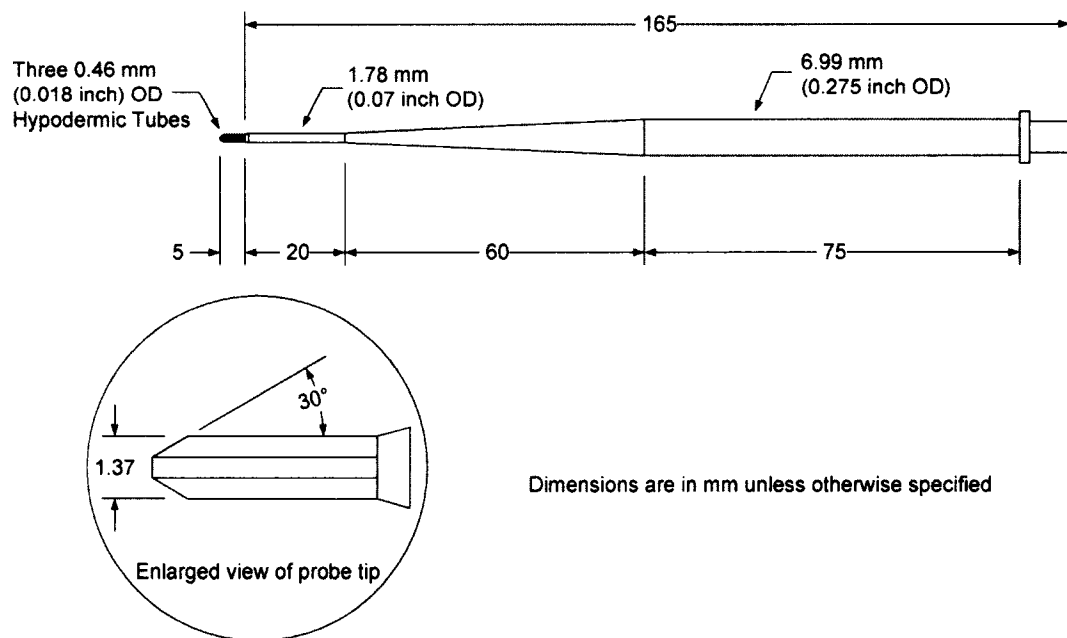


Figure 3.6 Dimensions of the Three-Hole Probe (reproduced from Islam 1999)

The movement of the probe within the cascade test section is controlled with the traversing gear shown in Figure 3.7. The three-hole probe is mounted in the

probe holder located at the end of the probe stem. The probe stem enters the test section through an opening in the transition walls downstream of the cascade. Two Teflon blocks are used to seal this opening. An additional Teflon piece is located as shown in Figure 3.7 to support the probe stem and prevent it from moving in the axial direction of the cascade. The movement of the traversing gear is driven by a stepper motor. This motor has 200 steps per revolution and a pitchwise displacement of 1.95mm per revolution. For the SL2 cascade which is used in this study, this results in a total of 3,488 steps per blade pitch. While there does not appear to be any significant backlash, the location of the probe is regularly measured to ensure there are no problems.

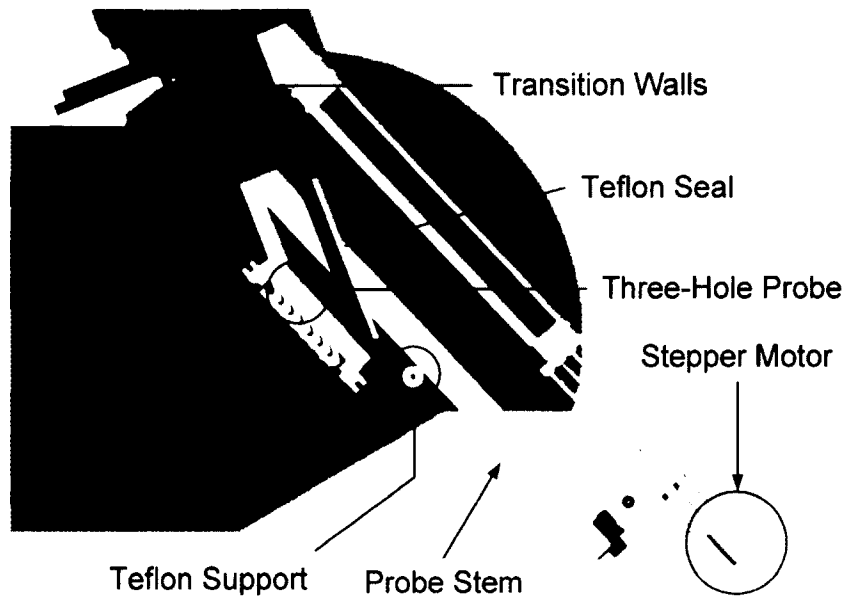


Figure 3.7 Probe Pitchwise Traverse Gear

3.3.3 Test Section Endwall Measurements

Upstream static pressures are measured with static taps on the window and downstream static pressures on the base plate of the cascade, as shown in Figure 3.8. The upstream static pressures are used to assess the upstream uniformity of the flow, as well as to measure the inlet Mach numbers of the cascade. The downstream static pressures are used to assess periodicity, provide endwall static measurements and to provide the static pressure measurement used by the new control system outlined in Chapter 4.

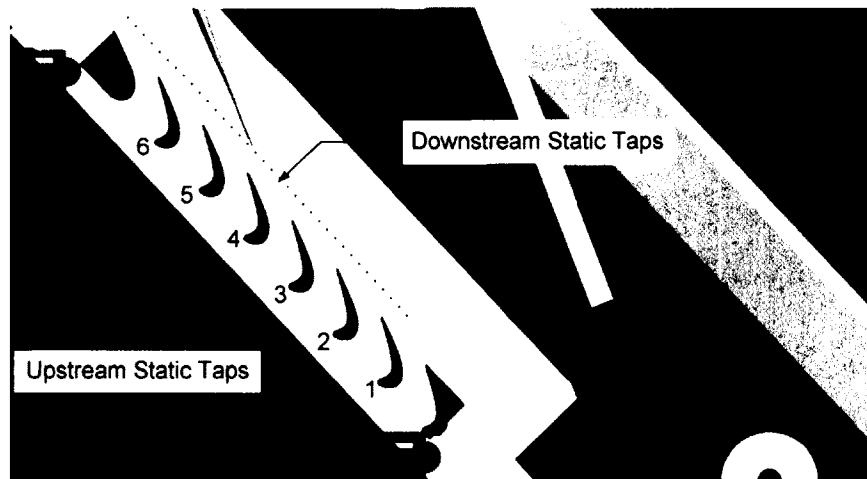


Figure 3.8 Location of Upstream and Downstream Static Taps with Blades Numbered

3.3.4 Upstream Reference Total Pressure and Temperature Measurements

Reference values of upstream total pressure and total temperature are measured using a cobra probe within which a thermocouple is mounted. The

location of this probe is indicated in Figure 3.4. The upstream total pressure is used to calculate the Mach number for the control of the wind tunnel, as well as to provide a reference upstream total pressure for the purpose of data reduction. The variation of Mach number during a run is evaluated in Chapter 4. The upstream total temperature is used in the mixing-out calculation to remove the effects of temperature variation due to the expansion of pressurised gas during the runs. During a typical traverse, the temperature can vary by as much as 25°C.

3.3.5 Data Acquisition System

The data acquisition system used by Corriveau (2005) and earlier users of the wind tunnel was replaced in 2007 by Taremi (2010). This was prompted by the poor response time of the old data acquisition system. The National Instruments PCI-6229 data acquisition card is used to read the voltages output by the pressure transducers. Similarly, the National Instruments USB-9211A data reader is used to amplify and read the voltage output from the thermocouple used to sense total temperature upstream of the cascade. The collection of this information is managed by custom software developed under LabVIEW 8. To ensure the measurements are not affected by the drift in the operating point or high frequency fluctuations such as flow turbulence, the pressure measurements used are the average of 200 samples taken at a sampling rate of 2kHz. These values were arrived at by Jeffries (2000) after an investigation of the effect of sampling time and frequency on the pressure measurements in this wind tunnel. Due to the new control system designed in

Chapter 4, these values may not be the most appropriate values. However, investigation of the sampling time and frequency is beyond the scope of this study, and will be deferred to future studies.

3.3.6 Uncertainties in Measured Values

The analysis of uncertainty in this wind tunnel performed by Corriveau (2005) remains valid. This analysis uses the method suggested by Kline and McClintock (1953) which is outlined in Section 4.6 where uncertainty at low Mach numbers is evaluated. The uncertainties for the values determined in this experiment are summarised in Table 3.2.

Table 3.2 Summary of Measured Values and Associated Uncertainties

Parameter	Range Measured	Uncertainty Range
Pressure	11.4 - 23.2 psi (74.3 - 160kPa)	$\pm 0.034 - \pm 0.070$ psi ($\pm 0.3\%$)
Inlet Flow Angle	43.5°	$\pm 1.0^\circ$ ($\pm 2.3\%$)
Outlet Flow Angle	64.3 - 70.7° ($\pm 5.0^\circ$ relative to probe centre)	$\pm 0.5^\circ$ ($\pm 0.8\%$)
Inlet Mach Number	0.098 - 0.29	$\pm 0.03 - \pm 0.01$ ($\pm 30 - \pm 3\%$)
Outlet Mach Number	0.18 - 1.08	$\pm 0.017 - \pm 0.003$ ($\pm 9.4 - \pm 0.3\%$)
Outlet Reynolds Number	150,000 - 831,000	$\pm 5,500 - \pm 80,000$ ($\pm 3.7 - \pm 9.6\%$)
Total Pressure Loss Coefficient	0.022 - 0.065	$\pm 0.048^* - \pm 0.0030$ ($\pm 218^* - \pm 4.6\%$) (*see Section 4.6.3)
AVDR	1.00 - 1.05	± 0.02 ($\pm 2\%$)

3.4 SL2 Cascade Geometry

All the results of this study were obtained using a turbine cascade designated SL2. The cascade geometry is summarised in Table 3.3 with the coordinates listed in Appendix C. This geometry was designed by Pratt & Whitney for the study by Taremi et al. (2010) which investigates the endwall flow in high-speed cascade testing. In the present work, only the midspan profile flow was measured.

Two of the blades were instrumented with static taps at midspan. The locations of the blade surface static taps are summarised in Appendix C. When the blade surface static pressures are measured, the instrumented blades are substituted for blades 3 and 5.

Table 3.3 SL2 Geometric and Design Flow Parameters

Chord Length, C	33.7mm
Axial Chord, C_x	25.4mm
Pitch Spacing, s	34.0mm
Throat Opening, o	12.0mm
Inlet Metal Angle, β_1	43.5°
Design Incidence, i_{des}	0°
Design Exit Flow Angle, $\alpha_{2,des}$	67.9°
Design Exit Mach Number, $M_{2,des}$	0.80
Design Reynolds Number, Re_{des}	611,000
Maximum Thickness, t_{max}	7.5mm
Trailing Edge Thickness, t_{tet}	1.04mm
Blade Height, h	61.0mm
Unguided Turning, δ	19.2°
Stagger Angle, ζ	41.2°
Design Zweifel Coefficient, $Z_{w,des}$	1.03

Chapter 4

Design of an Improved Wind Tunnel

Control System

4.1 Introduction

In any fluid dynamics experiment, the operating point can be completely defined by a number of non-dimensional parameters as calculated by Buckingham's Pi Theorem (Anderson 2005). For the experiments conducted in the High Speed Wind Tunnel at Carleton, the downstream Mach number is the most important non-dimensional parameter as it indicates the level of compressibility within the flow. In the past, a target Mach number was achieved by controlling the upstream total pressure of the flow. However, since the wind tunnel discharges to atmospheric pressure, the downstream static pressure, and thus the downstream Mach number, can vary with ambient conditions. A new proportional-integral-derivative (PID) control system has been developed that includes measurements of both the upstream total and downstream static pressures so that the wind tunnel control is based on the Mach number.

In addition to changing the basis for the wind tunnel control system, a number of system characteristics were identified, and appropriate compensations were built into the control where reasonable. Three of these characteristics have been compensated for through more than the PID control, namely the initial threshold voltage, valve dead band, and system undershoot.

4.2 Control System Components

4.2.1 Introduction

Most feedback control systems can be broken down into three basic parts: the sensor, the controller, and the plant. The control system created for the High Speed Wind Tunnel is broken down in this manner as shown schematically in Figure 4.1. The sensor is the differential pressure measurement used to calculate the Mach number in the wind tunnel. The controller is the control computer and the software created for the control. And the plant is the combination of the wind tunnel and the valve which regulates the flow in the wind tunnel. When this control system is used on the separate probe calibration rig, the same arrangement can be applied to the system with the differences being that the sensor measures the differential pressure in the calibration rig, and that the plant is the combination of the calibration rig and the control valve attached to the calibration rig.

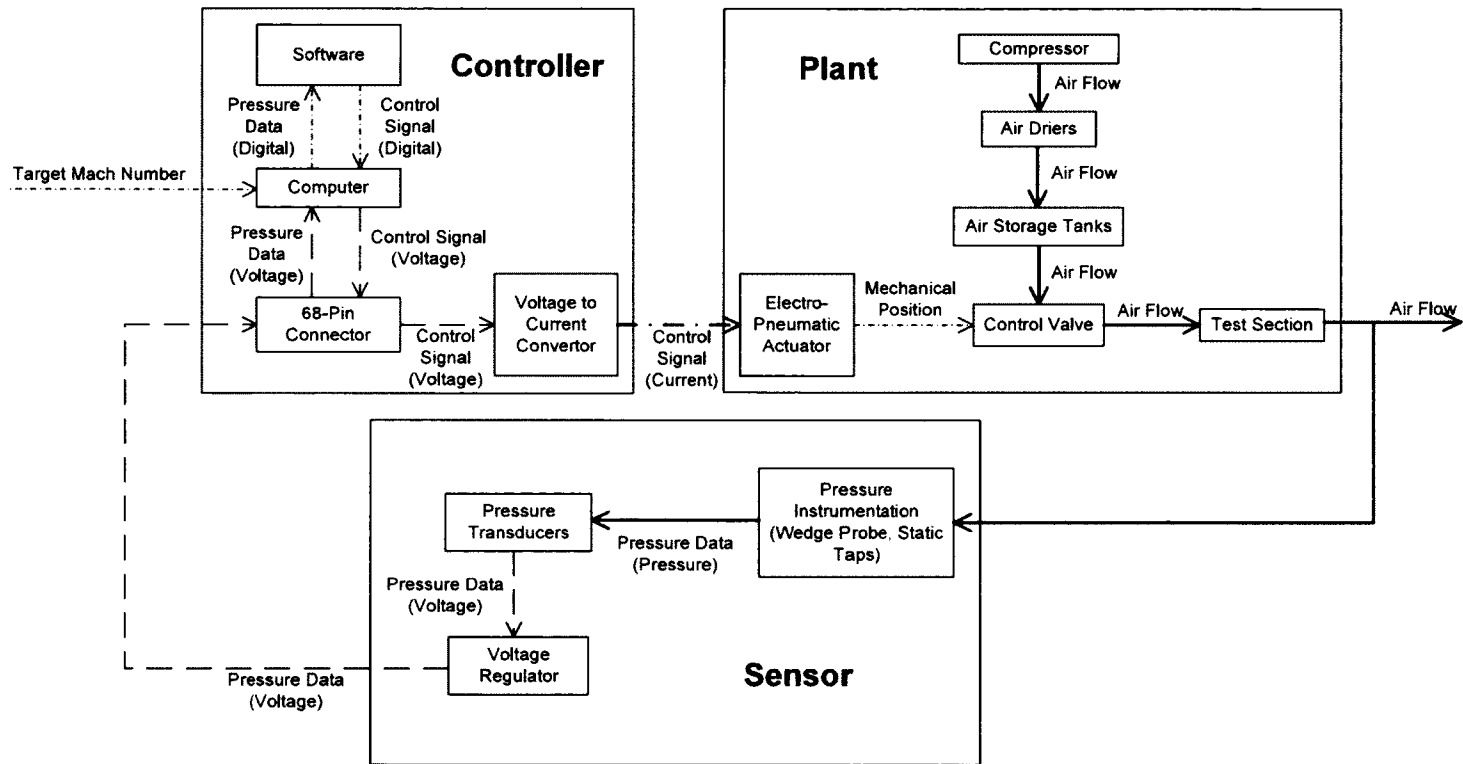


Figure 4.1 Control System Schematic

4.2.2 Pressure Measurement

The new control system measures two pressures separately to calculate the Mach number: an upstream total pressure and a downstream static pressure. These pressures are collected through the same instrumentation outlined in Section 3.3 that is used for the data acquisition system. The output of the transducers is a voltage on the order of millivolts, and is converted to a pressure through the correlations given in Appendix B. The slope of the correlation has been found to remain constant for months; however, the zero tends to be a function of many parameters which can change from day to day, such as ambient pressure, temperature, and humidity levels. As such, the zero should be corrected daily. This correction is especially important at lower Mach numbers as the equations tend to be more sensitive to errors, as outlined in Section 4.5.6. Each measurement uses the average of 200 points sampled at 2kHz as suggested by Jeffries (2000).

The Mach number is calculated from the upstream total pressure and the wall static pressure. This means that the Mach number used for control is not the actual Mach number downstream of the cascade, but rather the isentropic Mach number. There are several Mach numbers which can be used to specify the operating point: the isentropic Mach number, area-averaged Mach number, mass-averaged Mach number, and mixed-out Mach number are all commonly used. The mixed-out Mach number is the most appropriate, as it is independent of the downstream plane used for measurement. However it cannot be obtained until the data is collected, and so is inappropriate for control.

4.2.3 Data Acquisition Hardware and Software

The control computer has a National Instruments PCI-6229 data acquisition card installed. This allows the computer to read the voltage signals sent from the pressure transducers, as well as sending out a voltage signal between 0 and 10V which is used to position the valve. The computer uses software written in LabVIEW 8 to determine the appropriate output signal based on the input signal. While the output signal from the computer is a voltage signal from 0 to 10V, the actuator installed on the valve requires a current signal between 0 and 20mA to operate. The conversion is done with an Omega OM7-39-02-C voltage to current convertor.

4.2.4 Control Software

The operation of the control software is illustrated in Figure 4.2. The feedback loop for the software starts by measuring the current time, then reading the total and static pressures. Since there is the possibility of a delay in reading the pressures, the time used by the software can be slightly off. This delay occurs when using the data acquisition system (DAQ) because the control software has to wait for the DAQ to finish its measurements before the control software can take measurements as outlined in Section 4.3.6. Since these pressures are read as voltages, the pressure transducer calibrations must be applied so the Mach number can be calculated.

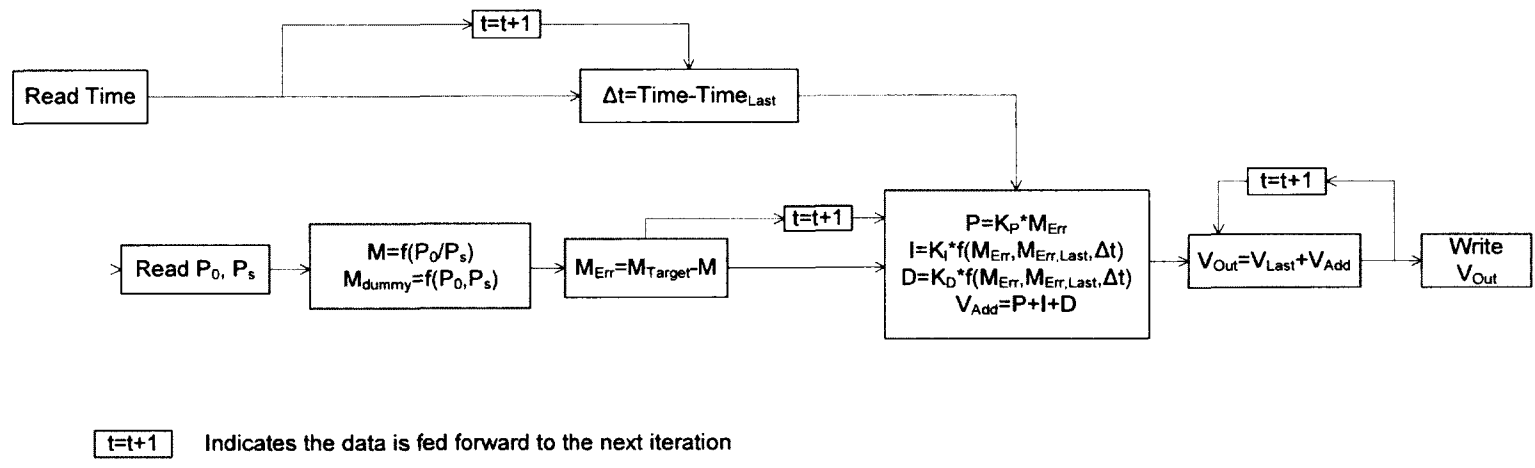


Figure 4.2 Control Software Flow Diagram

The control software then calculates the Mach number from the total and static pressures, as well as a dummy Mach number which is defined as

$$M_{Dummy} = \text{sign}(P_0 - P_s) \sqrt{\frac{2}{(\gamma - 1)} \left(\left(\frac{P_0}{P_0 - |P_0 - P_s|} \right)^{\frac{\gamma-1}{\gamma}} - 1 \right)} \quad 4.1$$

This dummy Mach number is used during the start-up of the wind tunnel when the total pressure measurement may read lower than the static pressure measurement. This is simply due to errors in the measurements of pressures that are very similar in magnitude, and is not indicative of any physical phenomenon. Using this dummy Mach number prevents the system from trying to calculate the square root of a negative number. Equation 4.1 has the advantage that it will produce the actual Mach number where the total pressure is greater than the static pressure. As well, because the dummy Mach number will be negative where the total pressure is read lower than the static pressure, the dummy Mach number will always be less than the target when it is not producing the actual Mach number. This will prompt the control system to open the valve, which is the appropriate response. The software is programmed to use the dummy Mach number for control until the Mach number reaches a value of 0.05 at which point the total pressure has been found to read consistently higher than the static pressure.

Once the software has calculated the true Mach number, it calculates the error, which is the difference between the Mach number and the target Mach number. This error, as well as the error from the previous Mach number, is used with Equation 4.2 to calculate the adjustment to the output control voltage. K_P , K_I ,

and K_D are gains used to give the tunnel operator control over the system response. Recommended values for the gains are outlined in Section 4.4. These gains are multiplied by an appropriate power of ten to make their magnitude generally fall between one and ten.

$$V_{Add} = K_P \cdot M_{Err} \cdot 10^{-2} + K_I \cdot \left(\frac{M_{Err} + M_{Err,Last}}{2} \cdot \Delta t \right) \cdot 10^{-4} + K_D \cdot \left(\frac{M_{Err} - M_{Err,Last}}{\Delta t} \right) \cdot 10^2 \quad 4.2$$

As outlined in Section 4.3, the software also compensates for the initial threshold voltage, valve dead band, and system undershoot.

4.2.5 Control Valves

The High Speed Wind Tunnel has two test sections which can be controlled by the control system. The test section in which cascade testing is performed is referred to as the main wind tunnel. The test section in which probe calibration is performed is referred to as the calibration rig. The main wind tunnel control valve is a 10.16cm (4in) Neles-Jamesbury model 815L ball valve. The control valve on the calibration rig was replaced during the implementation of the new control system because of the difficulties in achieving acceptable control. The calibration rig control valve on the old system was a 10.16cm (4in) Foxboro V9000 ball valve, while the new valve is a 5.08cm (2in) Neles-Jamesbury segmented ball valve. Both valves are positioned with a Neles-Jamesbury model QP2C electro-pneumatic positioner. This positioner accepts a current between 0 and 20mA as the input

signal, where 0mA corresponds to the fully closed position and 20mA is the fully open position.

4.3 Characteristics of the System Response

4.3.1 Introduction

In general, the response of the Mach number during a run was found to be that of a critically damped second-order system. Figure 4.3 shows typical responses of the main wind tunnel at several Mach numbers. Due to the complicated nature of the wind tunnel, there are a number of special features of the system response. One of the most apparent characteristics seen in Figure 4.3 is that the time for the target Mach number to be achieved increases for lower Mach numbers. Also, after reaching the target Mach number, there is some slight oscillation. In the main wind tunnel this is not a very pronounced oscillation: for example, in each of the three responses in Figure 4.3, the oscillation was below about ± 0.011 . Typical responses of the blowing pressure for the main wind tunnel for the old control system can be seen in Figure 4.4. While the blowing pressure cannot be directly compared to the Mach number, Figure 4.5 shows the response of the blowing pressure, static pressure, and Mach number for the new control system at a Mach number of 0.69. The new system clearly has less oscillation than the old system. Thus the new control system has improved the control of the main wind tunnel.

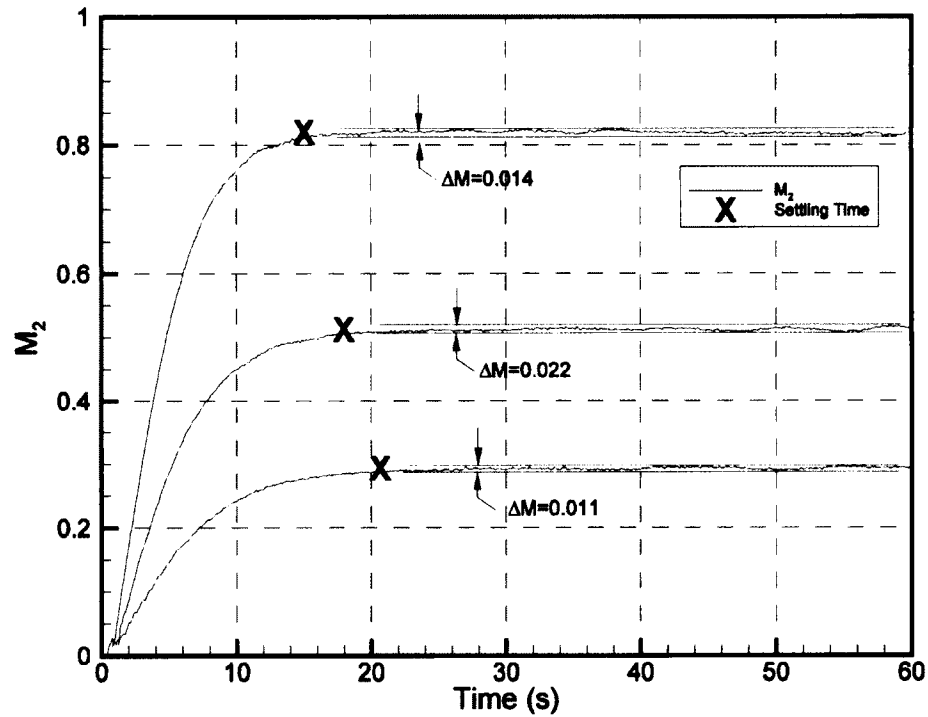


Figure 4.3 Sample Responses with the New Control System on the Main Wind Tunnel

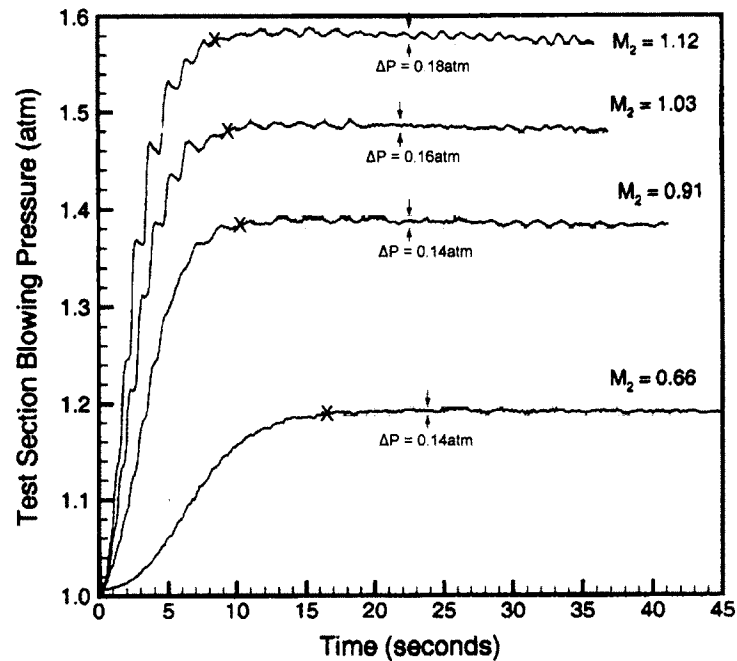


Figure 4.4 Sample Blowing Pressure Responses for Old Control System on the Main Wind Tunnel (Corriveau 2005)

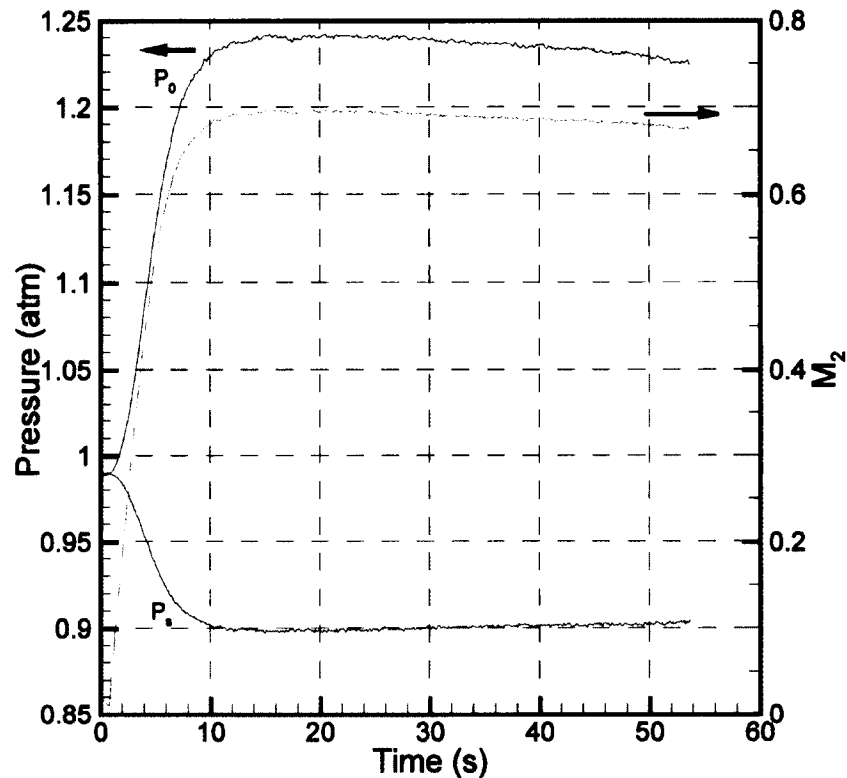


Figure 4.5 Variation of Mach Number, Blowing Pressure, and Static Pressure for the New Control System on the Main Wind Tunnel at a Mach Number of 0.69

Figure 4.6 shows typical responses on the calibration rig. Again, the increased settling time at lower Mach numbers is evident. However, the oscillations after reaching the target Mach number are much more pronounced. The period of the oscillations changes somewhat with Mach number. This can be contrasted with typical responses on the calibration rig with the old control system as seen in Figure 4.7. The behaviour of increased settling time with lower target Mach number is much more pronounced for the old control system, and the period of the oscillations show a significant increase at lower Mach numbers. Thus, the new control system has noticeably improved the control in the calibration rig.

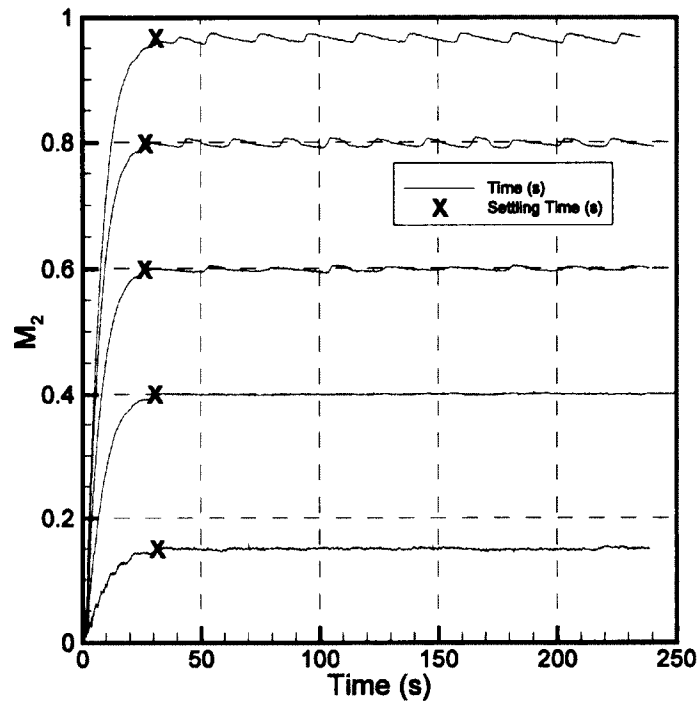


Figure 4.6 Sample Responses with the New Control System on the Calibration Rig

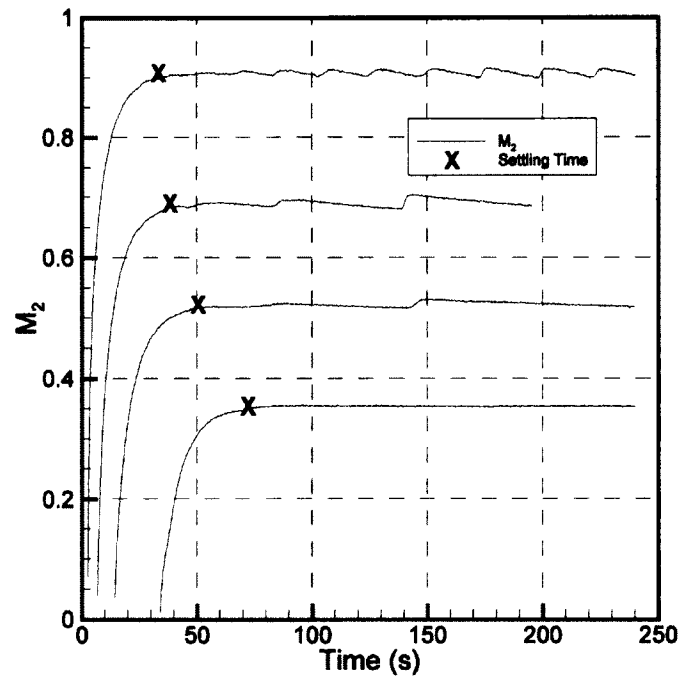


Figure 4.7 Sample Responses with the Old Control System on the Calibration Rig

4.3.2 Initial Threshold Voltage

The valves used in the High Speed Wind Tunnel do not produce air flow until some threshold level is achieved by the control voltage. This may be the result of mechanical slack being removed from the system at low control signals, or it may be that the ball valve must turn a certain angle before the opening in the ball begins to line up with the body of the valve. Regardless of the cause, air flow is not seen in the wind tunnel until some minimum voltage is output by the control computer. This voltage has been observed to be constant for a given valve. The actual voltage was easily determined by manually stepping the voltage in small increments until air flow could be heard in the wind tunnel. This characteristic of the valve is easily corrected by setting the threshold voltage as the starting value for the run. On the main wind tunnel, this voltage is 0.7V, while for the calibration rig it is 3.5V.

The improvement caused by implementing this correction is easily seen by comparing Figure 4.6 to Figure 4.7. The new system typically requires less than three seconds before there is any measured response on the calibration rig, regardless of the target Mach number. The old system requires three seconds to reach the threshold voltage at a Mach number of 0.9, while lower Mach numbers require more time. At a target Mach number of 0.35, the old system requires 34 seconds before any response is measured.

4.3.3 Valve Dead Band

When the control system requires the valve to switch between increasing and decreasing the opening, there is a small dead band where the valve does not respond. The exact mechanism for this dead band is unknown, but it is suspected to be the result of the valve sticking due to friction. Friction is suspected because the effects are not removed entirely by making the control signal change by some compensating value. In practise, the dead band can be compared to the backlash in meshing gears where the input – voltage for the valve, angle for the gear – must be changed by some finite value before the opposite sides of the teeth engage. Because the dead band is related to changing the direction of the valve motion, it is only apparent when the system response overshoots the target. This is seen on the calibration rig, where the dead band has been found to require an increase of roughly 0.3V to compensate. On the main wind tunnel, because there is no overshoot, the effects of the dead band do not require compensation.

The effect of this dead band can be seen in Figures 4.7 and 4.8. In Figure 4.8, when the Mach number is above the target, the Mach number decays somewhat due to the falling pressure in the storage tanks while the valve passes through the dead band. Once the valve has passed through the dead band, the Mach number rapidly drops below the target, at which point the control system changes the direction of the valve motion. Again, the Mach number decays somewhat due to the falling pressure in the tanks while the valve passes through the dead band. Once the valve is through the dead band, the Mach number rapidly jumps above the target, and the

whole process is repeated. The resultant response either resembles a reverse sawtooth wave or the combination of a square wave and a reverse sawtooth wave. On the old system, as shown in Figure 4.7, the valve does not fully pass through the dead band before the dropping pressure in the tanks brings the Mach number below the target. As a result, the valve passes through part of the dead band in trying to reduce the Mach number, and then has to pass through that same part of the dead band to raise the Mach number. The result is that the system response resembles a reverse sawtooth wave.

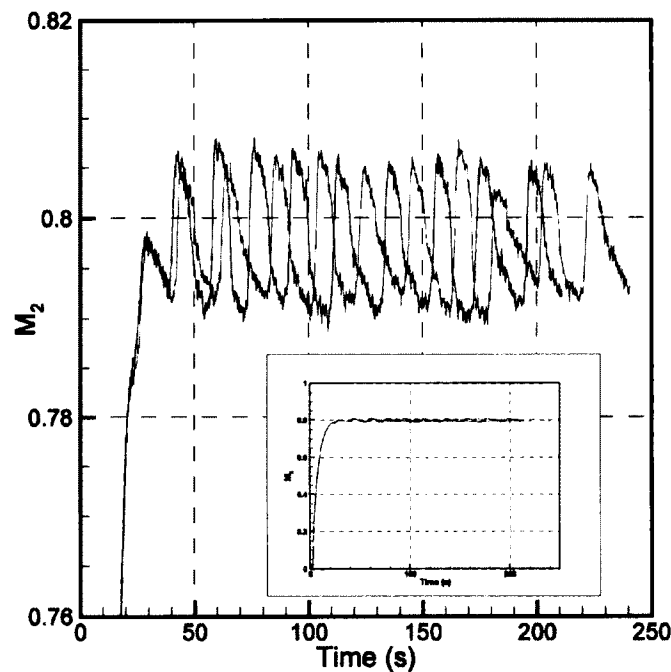


Figure 4.8 Response of the Control System on the Calibration Rig at a Target Mach Number of 0.8 Demonstrating the Result of the Valve Dead Band

4.3.4 Undershoot of Target Mach Number

This characteristic has been primarily observed on the main wind tunnel. When the wind tunnel has reached steady operation, the air storage tanks are losing pressure. As such, the appropriate opening for the valve to achieve the target Mach number is constantly increasing. The wind tunnel reaches steady operation when the rate at which the valve is opening matches the rate at which the target opening is increasing. However, the nature of the system is that this occurs at a Mach number slightly below the specified target value.

While increasing the influence of the integral part of the controller reduces this undershoot, it was found that completely removing the undershoot with the PID gains resulted in a response with unstable oscillations. To remove this remaining undershoot, upward correction proportional to undershoot percentage is built into the control software. This undershoot percentage is defined as

$$\text{Undershoot} = \frac{M_{\text{Internal Target}}}{M_{\text{Actual Target}}} - 1 \quad 4.3$$

For subsonic runs, a value of 0.01 was found to be appropriate. Higher values are appropriate for supersonic runs, although the same improvements may come from modifying the control gains. The undershoot percentage should be set to 0 when using the calibration rig.

The nature of this undershoot is demonstrated in Figure 4.9. The specified target Mach number was 0.9, the control software modified that value to an internal target Mach number of 0.909. As the system nears the target, it reduces the rate at

which it increases the output voltage. However, due to the dropping tank pressure, the target valve opening is increasing. At some point the target valve opening starts increasing faster than the output voltage is being increased. At this point the Mach number starts to drop, despite the internal target not having been reached.

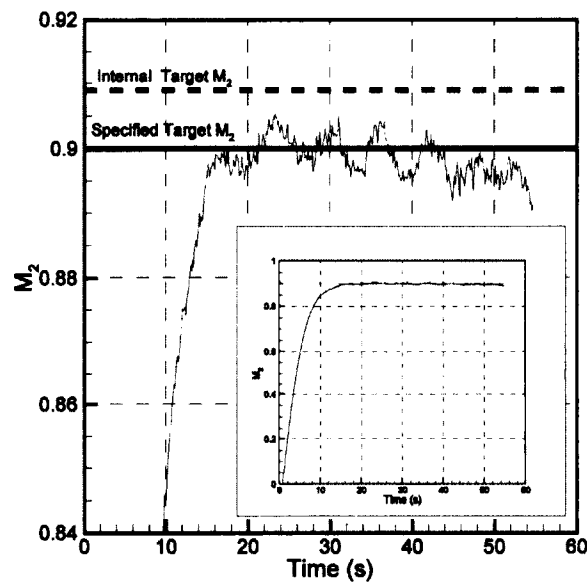


Figure 4.9 Undershoot of the Target Mach Number with Compensation

4.3.5 Repeatability

The response of the wind tunnel is not entirely repeatable. This is because there are a wide number of parameters that can change between runs. These can include air humidity, ambient temperature, storage tank pressure at the beginning of the run, and whether or not the compressor is idle at the start of the run. Figure 4.8 shows two runs for the calibration rig with identical PID gains and a target Mach number of 0.8. While the two responses drift apart, the important features are the

same. In particular, the oscillations have roughly the same period, the magnitudes of the oscillations are very similar, and the settling times are nearly identical.

At lower speeds, the repeatability of the system becomes more sensitive to small changes. This is seen in Figure 4.10 where two runs with identical PID gains show some striking differences. The black response has excellent quality, and rarely differs from the target by more than $\pm 0.5\%$ once settled. The red response takes longer for the initial oscillations to decay. After 200 seconds, the red response suddenly jumps. While the system is able to bring the Mach number back to the target and damp out the resulting oscillations, this process takes nearly 50 seconds, which illustrates the importance of monitoring the runs during data collection to ensure the wind tunnel is operating at the desired Mach number throughout the run.

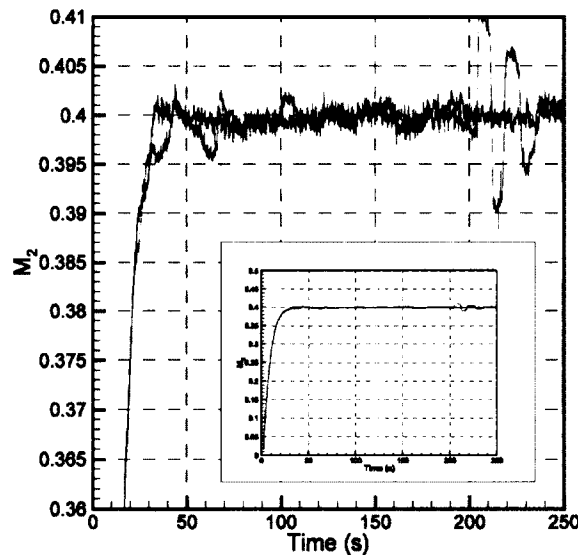


Figure 4.10 Repeatability of the Control System on the Calibration Rig at a Target Mach Number of 0.4

4.3.6 System Response During Data Collection

The control system behaves slightly differently during data collection. This is because the computer can only read one set of measurements from the data acquisition card at a time. To take this into account, the synchronisation tools of LABVIEW are used to delay the pressure measurements used for control while the data acquisition pressures are being read, and vice versa. This has the impact of roughly doubling the time interval between control adjustments every time the data acquisition system takes a measurement. Largely because the data acquisition system (DAQ) is only run once the system is maintaining a constant Mach number, the increased time interval does not result in any negative impacts on the response of the system. This is illustrated in Figure 4.11 which shows the outlet Mach number with the DAQ taking a measurement after every eight measurements by the control system. The DAQ measurements result in gaps in the control system data.

The control software does not specify that the data acquisition wait for eight measurements; this is a result of the combined time required for the probe traverse gear to step to the next location and the specified delay time before data acquisition. If this time is reduced, the number of measurements taken by the control system between DAQ measurements will change accordingly. This behaviour means the current system is not suitable for collecting continuous or high frequency data. As such, any future interest in high frequency data such as hot wire anemometry will require a separate data acquisition system to prevent interference from the control system.

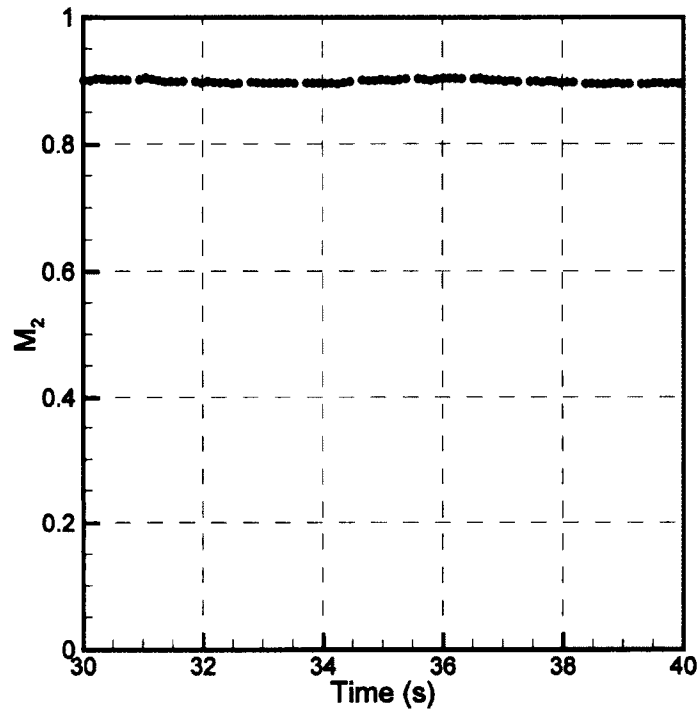


Figure 4.11 Control System Data while the Data Acquisition System is Running

4.4 Influence of PID Gains on System Response

4.4.1 Introduction

The new control system uses a proportional-integral-derivative (PID) controller to improve the system response. This gives the tunnel operator control over three control gains: the proportional gain K_P , the integral gain K_I , and the derivative gain K_D . When considering the influence of these gains on the response, high frequency fluctuations in the Mach number should be ignored as these fluctuations can be attributed to turbulence or high-frequency unsteadiness in the flow. Within the control system, these fluctuations are reduced by averaging 200

samples at 2kHz. However, the system response still exhibits some scatter which makes comparing different responses difficult. Therefore, for the purpose of evaluating the influence of the control gains, the system responses have been smoothed by averaging each measurement with the nearest 20 measurements. While flow unsteadiness could also cause low frequency fluctuations in the Mach number as well, the practice of connecting several downstream static taps to a manifold is expected largely to remove the effect of any low frequency flow features. As such, the characteristics of the smoothed response can be attributed to the control system. The Mach numbers have been normalised by the average settled Mach number as follows.

$$M_{Normalized} = \frac{M}{M_{Ave}} \quad 4.4$$

Because the oscillations and instabilities in the response tend to be sensitive to small changes in the control gains, the sample responses in this section only vary the appropriate control gain by a small amount. The discussion is still relevant to larger changes of the gains, although the behaviour of the oscillations will be harder to predict.

4.4.2 Influence of Proportional Gain, K_P

The primary influence of increasing the proportional gain is to decrease the settling time. Figure 4.12 shows the effect of changing the proportional gain on the response with a target Mach number of 0.29. While the proportional gain affects the oscillations as well, this behaviour is less consistent. When selecting appropriate

control gains, the proportional gain should generally be set first to achieve a reasonable settling time – usually between 15 and 20 seconds on the main wind tunnel, and between 25 and 30 seconds on the calibration rig. The default value of the proportional gain is set to 5 for the main wind tunnel and 4 for the calibration rig.

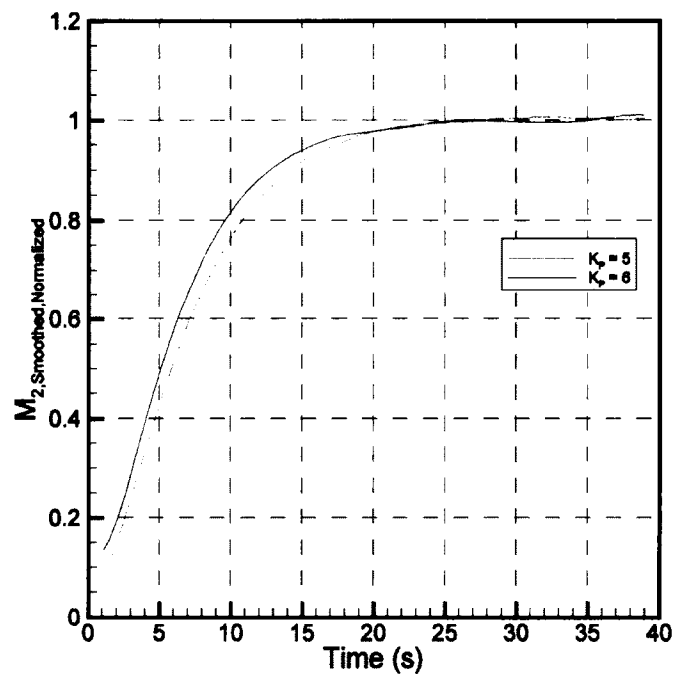


Figure 4.12 Influence of K_p on the System Response of the Main Wind Tunnel

4.4.3 Influence of Integral Gain, K_I

Increasing the integral gain decreases the settling time and usually increases the oscillations. Increasing the integral gain also reduces the system undershoot outlined in Section 4.3.4. Figure 4.13 shows the effect of changing the integral gain on the response with a target Mach number of 0.8. While the settling time is

affected, the effect of the integral gain is less important than the proportional gain since the settling time can be easily modified with the latter. For the main wind tunnel, the integral gain should be set to reduce the system undershoot as much as possible while avoiding excessive oscillations. An appropriate value has been found to generally be near that of the proportional gain. For the calibration rig, the lack of a system undershoot means that increasing the integral gain tends to be less useful, and often worsens the oscillations. For both the main wind tunnel and the calibration rig, when the oscillations of the system are unacceptable, the best solution is usually to reduce the integral gain. The default value of the integral gain is set to 6 for the main wind tunnel and 1 for the calibration rig.

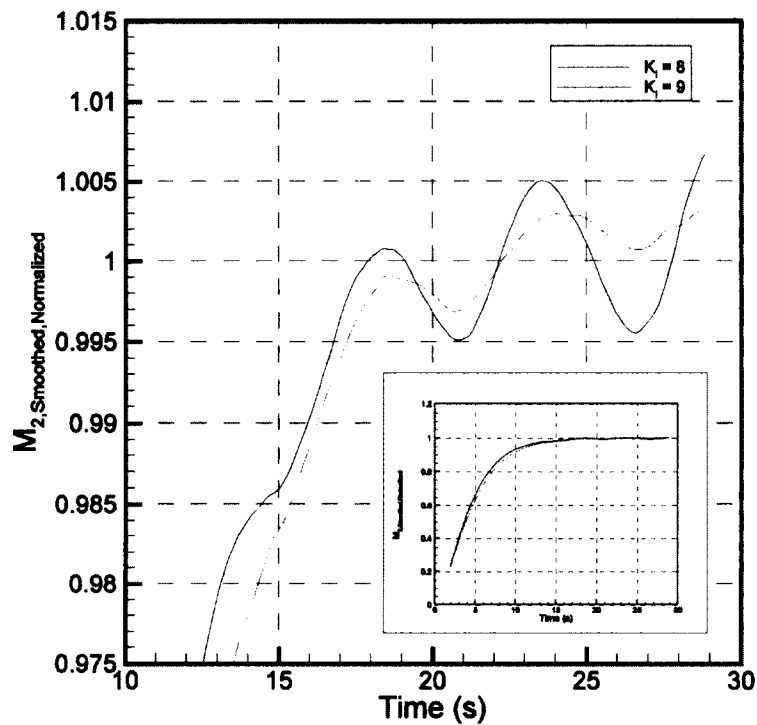


Figure 4.13 Influence of K_I on the System Response of the Main Wind Tunnel

4.4.4 Influence of Derivative Gain, K_D

Increasing the derivative gain increases the settling time as shown in Figure 4.14. The advantage of increasing the derivative gain is that it counteracts the increase in settling time caused by increasing the integral gain. While this may not seem obviously beneficial, the oscillations will often become excessive for short settling times, regardless of the gains. By using the derivative gain to counteract the effect of the integral gain on the settling time, a higher integral gain can be used to reduce the system undershoot. The default value of the integral gain is set to 2 for the main wind tunnel and 1 for the calibration rig.

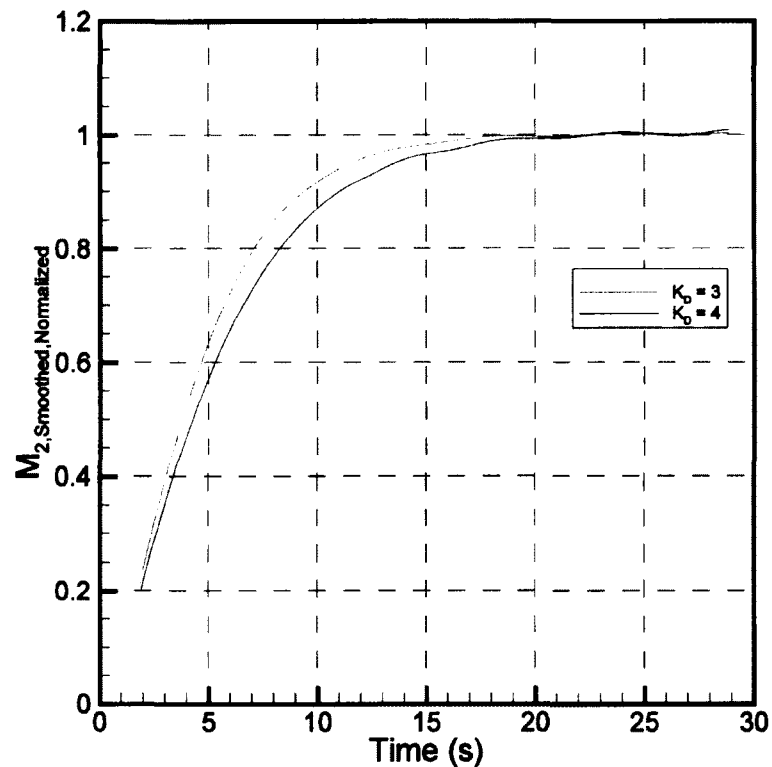


Figure 4.14 Influence of K_D on the System Response of the Main Wind Tunnel

4.4.5 Influence of Mach Number

For a given set of PID gains, the response will change depending on the target Mach number. Figure 4.15 shows three responses with the same PID gains with different target Mach numbers.

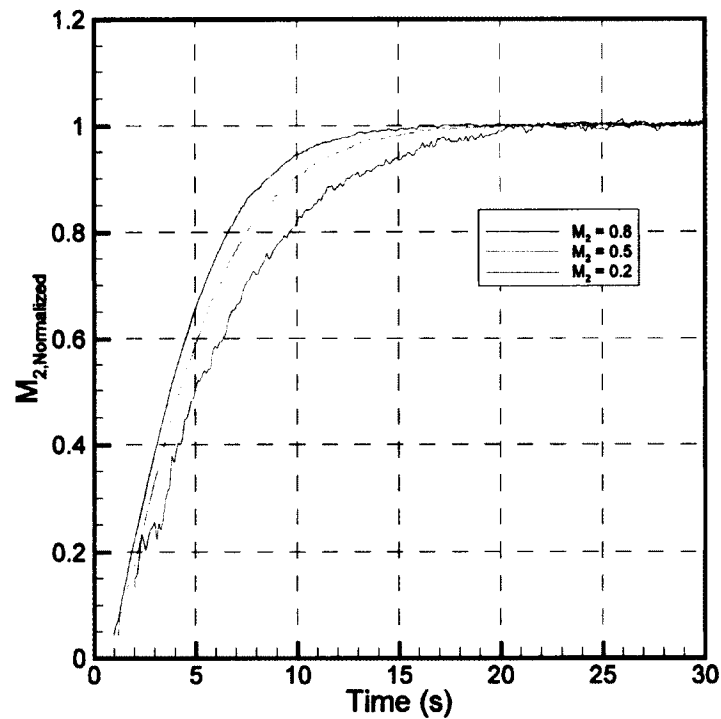


Figure 4.15 Influence of the Target Mach Number on the System Response of the Main Wind Tunnel

The principal differences between these responses are the settling times. The period of the oscillations is affected somewhat as well. On the main wind tunnel the period of oscillations increases with Mach number, while on the calibration rig the period of oscillations decreases with Mach number. The effect of the settling time increasing at lower Mach numbers is not a problem since the lower mass flow

rate results in longer run times. The effect of the oscillations changing with Mach number does mean that some Mach numbers may require changes to the control gains to obtain the desired quality of response.

4.5 Comparison to Previous Control System

4.5.1 Introduction

To quantitatively evaluate the effectiveness of the new control system, a number of runs were performed and subsequently analysed on the calibration rig with the old control system. The old system was not tested on the main wind tunnel primarily because the control quality of the calibration rig was known to be consistently poorer than that of the main wind tunnel; if a sufficient quality of control can be achieved on the calibration rig, then the control will be better on the main wind tunnel. Nevertheless, the control of the main wind tunnel with the old and new control systems can be compared qualitatively by using the sample responses of the old control system provided in Corriveau (2005). While the quality of the old control system was assessed quantitatively only on the calibration rig, the performance of the new control system has been evaluated for both the calibration rig and the main wind tunnel. This comparison of the quality of the new control system on both the calibration rig and the main wind tunnel demonstrates that the quality of the main wind tunnel control is better than that of the calibration rig. The new control system was assessed for multiple runs on the calibration rig to indicate

the repeatability of these measurements. The best and worst of these results have been included on Figures 4.19 and 4.20.

The performance of the control systems can be evaluated in a number of ways. Because the run time of the wind tunnel is one of the most limiting aspects of the facility, the settling time is of particular importance. The 99% settling time used to compare the responses is defined as the time at which the Mach number is 99% of the average settled Mach number.

Once settled, it is important that the control system maintain the target Mach number as closely as possible. To evaluate the ability of the control systems to do this, the average variation of the Mach number was calculated as

$$Variation_{Ave} = \sqrt{\frac{\sum_N (M - M_{Ave})^2}{N}} \quad 4.5$$

Two other aspects to compare are the user interface and the range of the available Mach numbers within the test section.

4.5.2 Qualitative Comparison to Previous Control System on Main Wind Tunnel

Several typical responses of the old control system on the main wind tunnel are demonstrated in Figure 4.16. Of particular importance is that the responses are characterised by small oscillations which have a period of about 1-3 seconds. These oscillations are especially noticeable as the Mach number is increased, and are attributed to the dead band discussed in Section 4.3.3. The system response of the

blowing pressure for the new control system is demonstrated in Figures 4.17 and 4.18. The oscillations which were present for the responses of the old system are greatly reduced, if not completely eliminated, in the responses of the new control system. The system response with the target Mach number of 1.2 at 15 seconds in Figure 4.18 demonstrates that variation in the blowing pressure may not lead to significant variation in the Mach number, highlighting the value of controlling the wind tunnel on Mach number rather than blowing pressure.

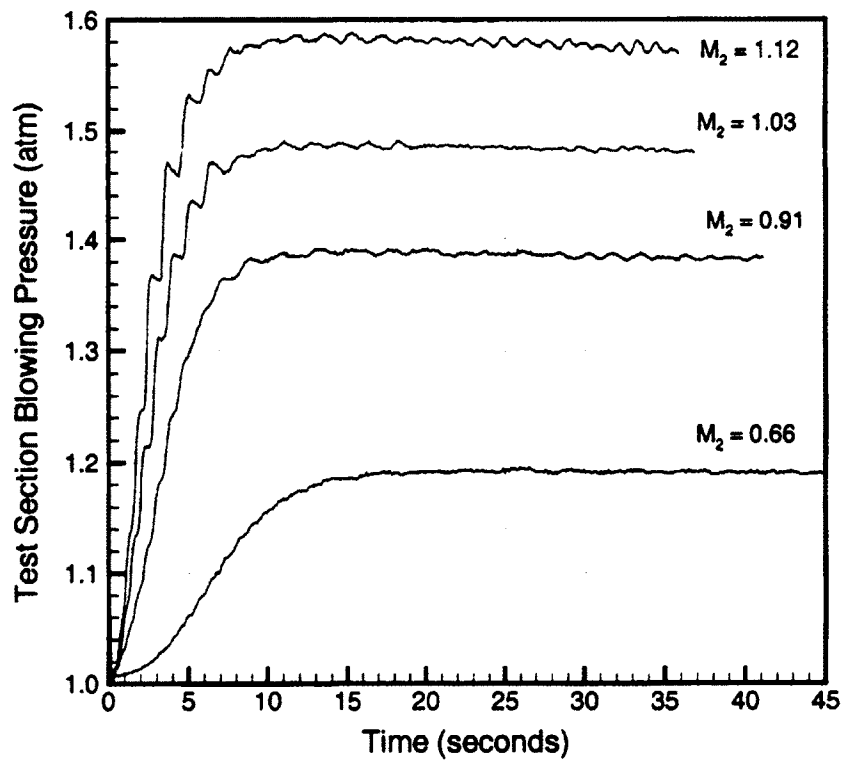


Figure 4.16 Sample Blowing Pressure Responses for Old Control System on Main Wind Tunnel (Corriveau 2005)

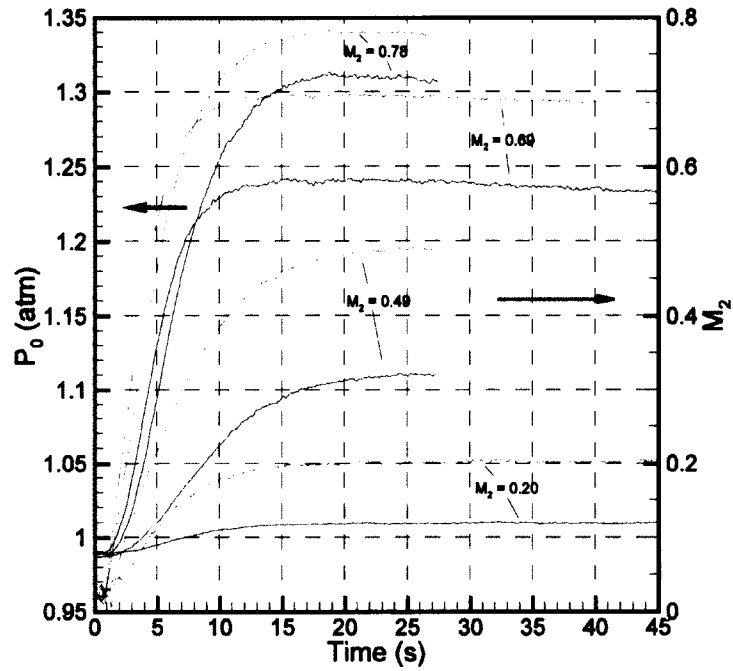


Figure 4.17 Blowing Pressure Response for New Control System on Main Wind Tunnel with Subsonic Target Mach Numbers

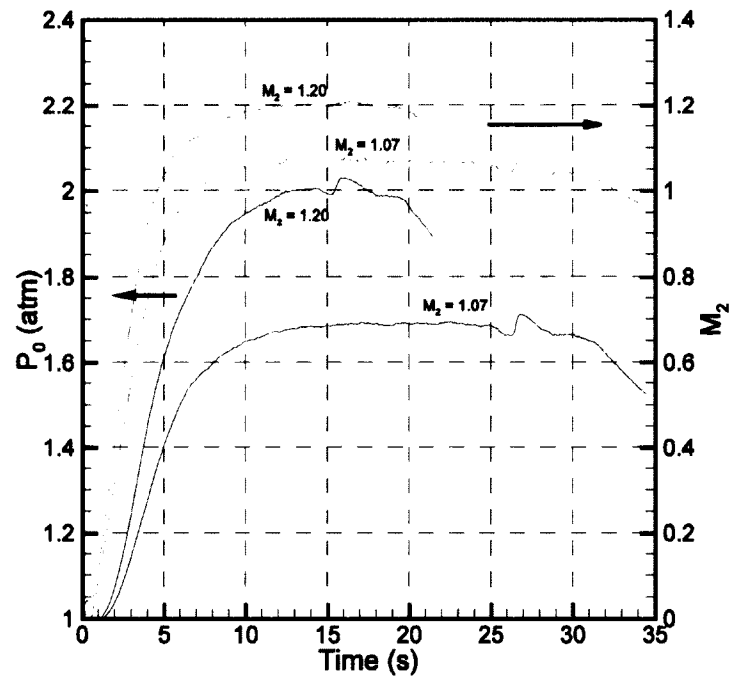


Figure 4.18 Blowing Pressure Response for New Control System on Main Wind Tunnel with Supersonic Target Mach Numbers

4.5.3 Settling Time

Figure 4.19 compares the settling time for the old and new control systems. On the calibration rig, the old control system has similar performance to the new control system at high Mach numbers, but the settling time rises quickly as the Mach number is decreased. On the calibration rig, the settling time for the new control system does not change much with Mach number, and generally stays between 25 to 30 seconds. While this time can vary from run to run, it tends to change by no more than about 5 seconds. On the main wind tunnel, the settling time for the new control system rises somewhat for low Mach numbers. Above Mach 0.5 the settling time stays between 15 to 20 seconds, while below Mach 0.5 the settling time rises a little above 20 seconds. Because minimising the settling time is important to maximise the available run time, the longer settling time at low Mach numbers is not a concern.

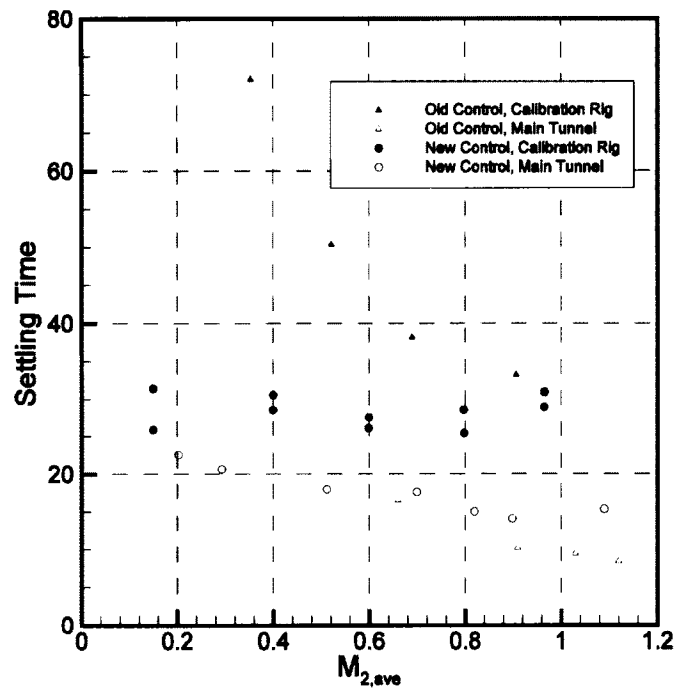


Figure 4.19 Comparison of the Settling Time for the Old and New Control Systems

4.5.4 Variation of Mach Number During the Run

The variations in the Mach number as calculated by Equation 4.5 are compared for the new and old control systems in Figure 4.20. On the calibration rig, the new control system performs better than the old one. On the calibration rig, the Mach number is generally controlled to within about $\pm 0.8\%$ of the settled Mach number. On the main tunnel, the Mach number is controlled to within $\pm 0.5\%$ of the settled Mach number. Below about Mach 0.4, the variations in Mach number increase sharply. This is largely due to the uncertainty in the data, as discussed in Section 4.5.6, and cannot be expected to improve without improved instrumentation.

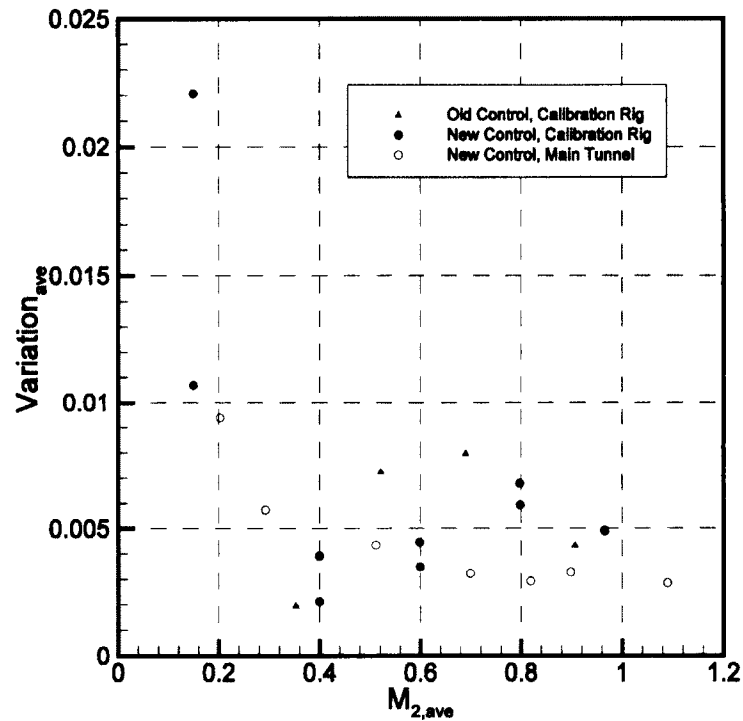


Figure 4.20 Comparison of the Variation in Mach Number for the Old and New Control Systems

4.5.5 User Interface

While the user interface for the old control system gave the user the ability to make any changes to the control necessary, it did not have much more than the bare minimum. The user interface for the new control system contains a number of advantages over the old system, two of which are of particular importance and will be outlined here. The first advantage is the ability to set the desired Mach number, rather than setting the upstream total pressure that is expected to produce the desired Mach number. The second advantage is that the new control system produces a plot of the Mach number during the run which instantly informs the user

of the quality of the run, rather than assessing each run afterwards. While these improvements may not affect the actual control during the run, they are nonetheless useful.

The increased control over the operating point is a major advantage of the new control system. Because the operating point is defined by the Mach number, the new control system has an obvious advantage. To set the Mach number on the old control system, the isentropic Mach number equations could be used to provide an estimate of the desired total pressure. However, the downstream static pressure usually varies significantly from atmospheric, meaning that setting the Mach number on the old system typically required iteration. Further, because the Mach number is sensitive to the total pressure at low Mach numbers, fine control of the target Mach number is difficult with the old control system.

The average settled Mach number with the new control system was always within 0.5% of the specified target Mach number for subsonic runs on both the main wind tunnel and the calibration rig. While the average settled Mach number during supersonic runs were not as close to the target as the subsonic runs were, the appropriate PID gains for supersonic runs have not yet been firmly established.

With the old control system, it was common practice to match the operating point by comparing the blade surface pressure measurements to CFD results. Even with the improvements of the new system, this will still be good practice. Despite the close match between the target Mach number and the settled Mach number, these Mach numbers are based on the static pressure at the wall. Additionally, the

control system is based on the isentropic Mach number; blade loading measurement allows the actual Mach number to be set up. In the calibration rig, the wall static pressure will be reasonably close to the actual static pressure experienced by the probe. In the main wind tunnel, the wall static pressure will be influenced by the complicated flow structures created by the cascade, and therefore the measured Mach number is not necessarily the desired mass-averaged or area-averaged outlet Mach number.

During the run, the user needs to know when the wind tunnel has achieved the target Mach number, as well as whether or not the operating point is being maintained well enough for the data to have the desired quality. On the old control system a number of values, including the total pressure, were output to the screen after every measurement. Since these were output in a numeric format, it was difficult to interpret the control data during the run unless something went wrong. The result is that the settling time was generally assumed to be 20 seconds on the main wind tunnel for the purposes of starting the data acquisition system, unless the total pressure was clearly different from the target at that time. The quality of the run could not be easily assessed during the run, so the control data was plotted after every run. Any problems during the run would not be detected until afterwards. With the new control system, the Mach number is plotted during the run. This allows the user to know more easily when the wind tunnel has reached the target Mach number, as well as reacting appropriately to poor quality in the

control – either by waiting for the response to stabilise before collecting data, or by ending the run immediately preventing the air tanks from discharging needlessly.

4.5.6 Range of Available Mach Numbers

The lower limit for the available Mach numbers has been greatly reduced with the new control system. The old system has never been run on the main wind tunnel below a Mach number of 0.55, while the new control system is capable of running at Mach numbers as low as 0.1. This limit is mostly due to the accuracy of the pressure measurements. The upper limit for the available Mach numbers is primarily based on the capacity of the air tanks and the geometry being tested, and so is essentially unchanged from the old system. For the SL2 cascade, this limit was found to be around a Mach number of 1.25.

4.6 Uncertainty of Data at Low Mach Numbers

4.6.1 Introduction

One of the major improvements of the new control system over the previous control system is the ability to run at much lower Mach numbers. However, because past data from this facility has always been at higher speeds, it is important to re-evaluate the uncertainty of the data collected. The uncertainty of calculated values can be estimated using the method suggested by Kline and McClintock (1953). This method states that the uncertainty for any calculated result can be calculated by

$$\delta F = \sqrt{\left(\frac{\partial F}{\partial \phi_1}\right)^2 \delta \phi_1^2 + \left(\frac{\partial F}{\partial \phi_2}\right)^2 \delta \phi_2^2 + \dots + \left(\frac{\partial F}{\partial \phi_N}\right)^2 \delta \phi_N^2} \quad 4.6$$

where F is the result being calculated,

$\phi_1, \phi_2, \dots, \phi_N$ are the independent variables from which F is calculated,

δF is the uncertainty in F, and

$\delta \phi_1, \delta \phi_2, \dots, \delta \phi_N$ are the uncertainties in the independent variables.

Equation 4.6 assumes the uncertainty in the data is normally distributed due to random noise. As such, it is important to recognise that this analysis only estimates the uncertainty due to this noise. Any systematic uncertainties will not be properly accounted for since systematic uncertainty will tend to bias the measurements in one direction, rather than distributing the measurements evenly about the correct value. However, any systematic uncertainty will be increased where there is increased uncertainty due to random noise.

Because nearly all of the results from the wind tunnel are calculated from pressure data, the uncertainty in the results is calculated from the uncertainty in the pressure. The pressure is calculated from

$$P = mV + z \quad 4.7$$

where P is the pressure,

m is the slope of the transducer calibration curve,

V is the voltage measured from the transducer, and

z is the intercept of the transducer calibration curve.

The uncertainty in the voltage was estimated to be 0.25% by Jeffries (2000) based on a sampling time of 0.1 seconds and a sampling frequency of 2kHz. The uncertainties in the pressure transducer calibrations can be estimated based on the standard deviation in the correlation coefficients calculated in Appendix B. From these uncertainties, and Equations 4.6 and 4.7, the uncertainty in the pressure measurements is estimated to be below $\pm 0.3\%$ for absolute pressures above 70000kPa (0.7bar). The lowest pressures in the wind tunnel are experienced at high Mach numbers, and did not drop below 70000kPa (0.7bar) during the current study.

4.6.2 Uncertainty in the Mach Number

The Mach number is calculated from total and static pressure using the following equation:

$$M = \sqrt{\frac{2}{(\gamma - 1)} \left(\left(\frac{P_0}{P_s} \right)^{\frac{\gamma-1}{\gamma}} - 1 \right)} \quad 4.8$$

From equations 4.6 and 4.8 the uncertainty in the Mach number reduces to

$$\delta M = \frac{\sqrt{2}(5 + M^2)}{7M} (0.003) \quad 4.9$$

This is a function of the Mach number alone, and the relationship is shown in Figure 4.21. The uncertainty increases significantly below a Mach number of about 0.3, and any data collected below this operating point should be treated with caution.

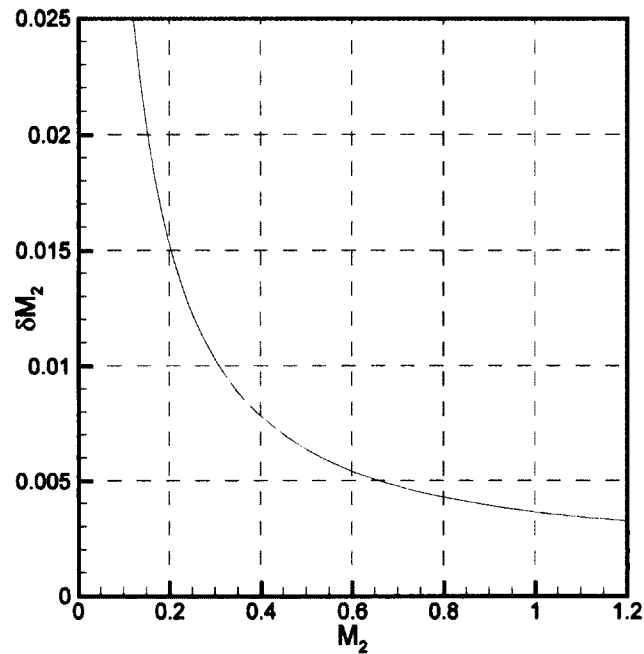


Figure 4.21 Estimated Uncertainty in the Measured Mach Number

4.6.3 Uncertainty in the Total Pressure Loss Coefficient

There are a number of coefficients used to indicate the level of the losses.

The most commonly used is the total pressure loss coefficient Y which is defined as

$$Y = \frac{P_{01} - P_{02}}{P_{02} - P_2} \quad 4.10$$

From this and equation 4.6, the uncertainty in Y can be expressed as

$$\delta Y = \frac{0.003}{(P_{02} - P_2)^2} \sqrt{P_{01}^2 (P_{02} - P_2)^2 + P_{02}^2 (P_2 - P_{01})^2 + P_2^2 (P_{01} - P_{02})^2} \quad 4.11$$

To assess the effect of Mach number on this uncertainty, the assumption is made that

$$P_{01} = P_{02} \quad 4.12$$

This assumption yields

$$\delta Y = \frac{0.003\sqrt{2}}{\left(1 - \frac{1}{\left(1 + \frac{\gamma-1}{2}M^2\right)^{\frac{\gamma-1}{\gamma}}}\right)} \quad 4.13$$

This equation is plotted in Figure 4.22. Although this estimated uncertainty is conservative, the trend clearly rises substantially at low Mach numbers.

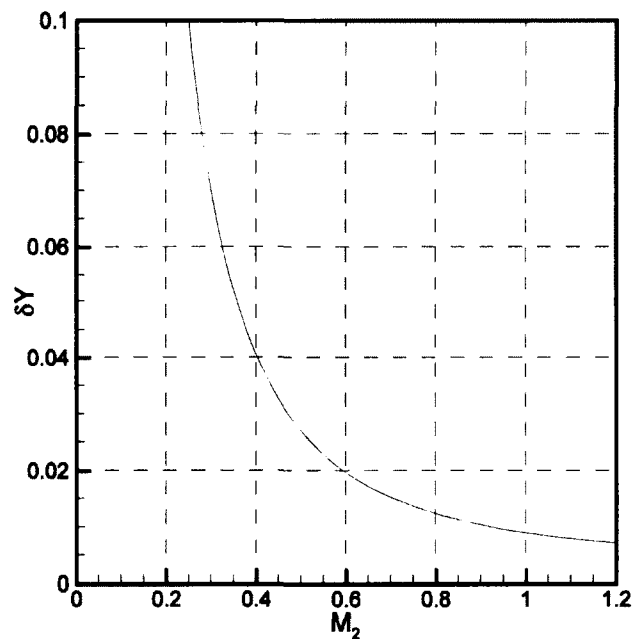


Figure 4.22 Estimated Uncertainty in Loss Coefficient Assuming No Losses

4.6.4 Uncertainty in the Integrated Pressure

Many values of interest are calculated from the integrated values of the pressures. Therefore it is useful to evaluate the effect of this integration on the uncertainty in the calculated quantity. Because the uncertainty in the pressure is a function of the pressure level, the uncertainty in the integrated pressure will depend

on the actual pressure distribution. However, by assuming that the uncertainty in each pressure is equal to the greatest uncertainty within the data, a conservative estimate for the uncertainty in the integrated pressure can be readily determined. For a set of N evenly spaced data where the uncertainty in each data point is the same, Equation 4.6 indicates that the uncertainty of the integrated value F can be estimated from

$$\delta F_{Integrated} = \frac{\sqrt{N}}{N} \delta F \quad 4.14$$

This estimate is based on the assumption that the data is normally distributed about the correct value. Any errors introduced by a single data point will tend to be compensated for by errors in the other direction from other data points. For this reason, Equation 4.14 predicts that any uncertainty will be removed by adding enough measurement points. If there is a systematic uncertainty present in the data, or if the uncertainty in the data is not normally distributed, this will not be the case. As such, while the integrated values will tend to have less uncertainty due to random noise, they should be carefully considered to remove – or at least account for – any possible systematic uncertainty.

4.7 Conclusions

The control system for the High Speed Wind Tunnel has been replaced with an improved control system. The primary motivation for this replacement was to implement a control system that operates based on the Mach number, rather than

the upstream total pressure. The improved control system allows for less variation in the Mach number during the run, as well as reduced settling time. The new control system also allows the wind tunnel to be run at Mach numbers as low as 0.1 whereas the old control system was usable only down to Mach numbers of about 0.55. The new control system's success can be partly attributed to the compensation introduced for the initial threshold voltage and the valve dead band. In addition to the improved quality of the control, the new control system includes an improved user interface.

Chapter 5

Computational Procedure and Results

5.1 Introduction

Because the Reynolds number is allowed to vary with the Mach number in the experiment, it is important to consider how much influence both the Mach number and the Reynolds number have on the results. Kacker and Okapuu (1982) suggest the influence of Reynolds number on the losses should be ignored when the Reynolds number is between 200,000 and 1,000,000; however this suggestion is prompted by the lack of quantitative information for estimating the losses in this range at the early stage in the design at which the Kacker and Okapuu loss correlations are typically used. Computational Fluid Dynamic (CFD) simulations were performed in this study in order to estimate the influence of the Reynolds number on the flow independently of Mach number, as well as to assist interpretation of the experimental results.

5.2 Test Cases

The CFD simulations in this study fall into four sets: a fixed Reynolds number set; two fixed Mach number sets; and a set which varies the Mach number while the

Reynolds number corresponds to a fixed exit pressure. The combinations of Reynolds number and Mach number are summarised in Figure 5.1. The Mach numbers and Reynolds numbers in this chapter refer to the values obtained from the wake data measured at a plane of $1.4 C_x$. The mixed-out calculation integrates the mass and momentum equations over one blade pitch, and then calculates the flow values at a downstream plane assuming mixing at constant area to uniform flow. This procedure is outlined in Jouini (2000).

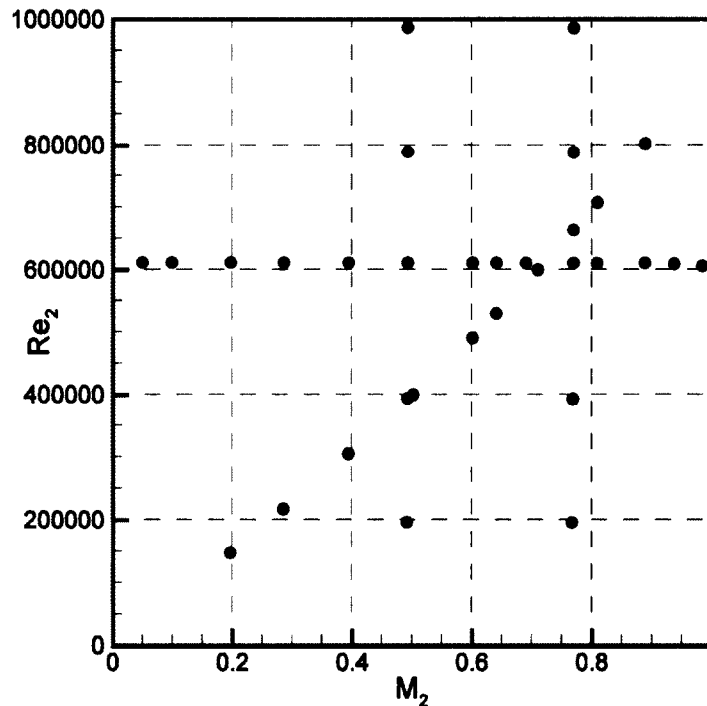


Figure 5.1 CFD Test Cases in this Study

The fixed Reynolds number set is intended to capture the effects of Mach number independent of changes in the Reynolds number. The cases in this set have a Reynolds number of $611,000 \pm 1,000$, while the Mach number ranges from 0.05 to

0.98. The Reynolds number was selected to correspond to the design condition, while the Mach number range is intended to capture the full range of compressibility effects up to the sonic condition.

The fixed Mach number sets are intended to capture the effects of Reynolds number independent of the effects of changing Mach number. Both sets have Reynolds numbers ranging from 200,000 to 1,000,000, while the Mach number is set at 0.491 ± 0.001 for one set, and 0.768 ± 0.002 for the other. The Reynolds number range for this set is based on the work of Kacker and Okapuu (1982) which found no reliable correction for the effects of Reynolds number on the total pressure loss coefficient in this range. The Mach number of 0.77 was chosen to be near the design Mach number of the geometry. The Mach number of 0.49 was chosen to indicate whether or not the influence of Reynolds number on the results is independent of Mach number.

The set with the Reynolds number corresponding to a fixed exit pressure as the Mach number varies is intended to approximate the behaviour of the wind tunnel where both the Mach number and Reynolds number vary. This was achieved by setting the exit boundary condition to have an area averaged exit pressure of 1atm. The result is that the Reynolds number will be different for each Mach number simulated. Because the CFD simulations were run before the experiment, this set was not adjusted to compensate for the fact that the pressure downstream of the cascade in the wind tunnel is lower than atmospheric due to the diffuser, especially at high Mach numbers. For this reason, additional simulations were run

after the experiment to match the experimental operating points. The results of these additional simulations are shown along the experimental results in Chapter 6 to validate the simulations. Regardless, since these additional simulations lead to the same conclusions, this chapter will only discuss the results of the simulations which approximated the wind tunnel conditions with a constant exit pressure. This set has Mach numbers ranging from 0.20 to 0.89, which resulted in the Reynolds number ranging from 150,000 to 800,000. The range of Mach numbers was the same as the fixed Reynolds number set, but the lowest and highest Mach numbers that achieved convergence were 0.20 and 0.89 respectively.

5.3 Solution Method

5.3.1 Solver

The CFD simulations in this study were all performed using version 12 of the commercial Navier-Stokes solver CFX produced by ANSYS. CFX uses the finite volume method to solve the governing equations numerically. This method involves taking a mesh of the fluid domain, and constructing control volumes around each node of the mesh. The governing equations are then integrated and discretised over each control volume. Because the solution variables and fluid properties are stored at the nodes, the values at the faces of the control volumes must be interpolated from the node values. This interpolation is done using a shape function based on the mesh element type with the exception of the advection terms of the governing

equations. There are several options available for use with the advection terms. The simulations in this study all use the specified blend factor option, with the blend factor set to 1. This choice is second-order accurate in space. To assess whether or not the simulations had reached a converged solution, the normalised residuals were monitored until they reached a value below 10^{-5} . The simulations performed were all steady-state simulations, so that the time-dependent capabilities of CFX are not used for this study. All simulations used the air ideal gas model for the fluid properties.

5.3.2 Mesh

The meshes used for the simulations were created in ICEM CFD. The meshes are hexahedral unstructured meshes. Multiple meshes were required since the simulations at higher speeds required more nodes near the blade surface to achieve satisfactory mesh quality, while the simulations at lower speeds required fewer nodes to achieve a converged solution. The meshes all had between 50,000 and 60,000 nodes. This number of nodes was found to give results essentially independent of the number of nodes; increasing the number of nodes by a factor of 1.5 changed the loss coefficient by less than 0.8% and changed the pressures in the trailing edge flow by about 0.3%. An example mesh is shown in Figure 5.2, with a close-up view of the trailing edge of the blade in Figure 5.3, to show the inflation layer used to capture the details of the boundary layer. The inflation layer contained at least 30 nodes for all meshes.



Figure 5.2 Example Mesh of the Fluid Domain

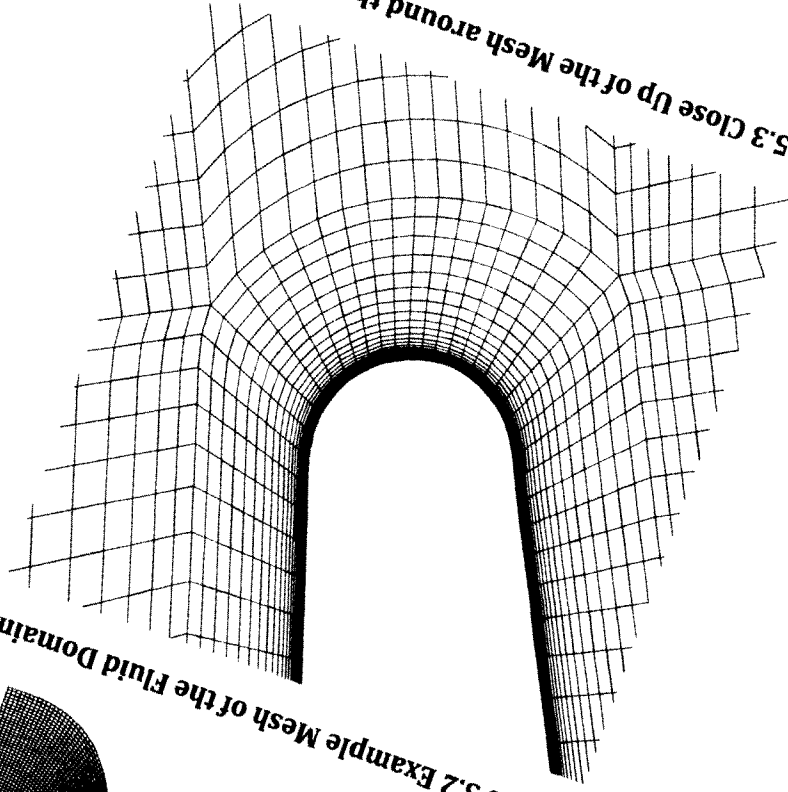


Figure 5.3 Close Up of the Mesh around the Trailing Edge

The mesh quality was assessed based on several criteria. Every hexahedral element in each mesh was assessed based on aspect ratio, minimum internal angle, volume change, and determinant. The volume change for an element refers to the ratio of the volume of the largest adjacent element to the volume of the element in question. The determinant refers to the normalised determinant of the Jacobian of each element. The quality of the mesh near the blade surface was also assessed on the criteria of y^+ and expansion ratio in the direction normal to the wall. The value of y^+ is defined as

$$y^+ = \frac{\rho_w \sqrt{\frac{\tau_w}{\rho_w}} y}{\mu_w} \quad 5.1$$

where y is the normal distance to the wall, and w denotes a value taken at the wall. The value of y^+ is a non-dimensional distance from the wall which is a measure of the turbulent-laminar ratio. The value of y^+ for the first element from the wall must be below 1 for the gamma-theta transition model used in this study to be valid. The expansion ratio refers to the change of spacing between nodes in a given direction. The limits for these criteria suggested by ANSYS and the values in the meshes used are listed in Table 5.1. The maximum aspect ratio of the meshes in these simulations was only large near the blade surface in order to resolve the boundary layer without increasing the overall node count excessively. The value of y^+ is based on the flow values as defined in Equation 5.1. As such, the value of y^+ for a given mesh tends to change with the operating point. This is the reason that the simulations at higher speeds required a finer mesh near the blade surface.

Table 5.1 Mesh Quality Criteria

Criterion	Recommended Value	Mesh Quality Achieved
Aspect Ratio	<1000	<800
Minimum Internal Angle	>18	>40
Volume Change	<2	<1.5
Determinant	>0.3	>0.7
y ⁺ of first node from wall	<1	<1
Boundary Layer Expansion Ratio	≤1.1	≤1.1

5.3.3 Boundary Conditions

Five sets of boundary conditions were required to fully constrain the flow as shown in Figure 5.4. Two-dimensional flow was simulated by using symmetry boundaries on the spanwise boundaries of the domain. A cascade of infinite blades was simulated with a translational periodic boundary condition on the pitchwise boundaries. The blade surface has a no-slip, adiabatic boundary condition. The inlet plane boundary condition specified a uniform total pressure, flow direction, total temperature, turbulence intensity, and turbulence length scale. The inlet total temperature was set to 300K. While this is slightly higher than the experiment, which has an inlet total temperature between 270K and 295K, the mixing out calculation removes the effect of upstream total temperature. The heat transfer between the air and the blade has been neglected. The turbulence intensity was set

to 4% to match the value in the wind tunnel, and the turbulence length scale was set to 15.24mm based on the measurements by Corriveau (2005). The turbulence parameters are further discussed in Section 5.3.4. Finally, the exit plane boundary condition specifies an area-averaged static pressure.

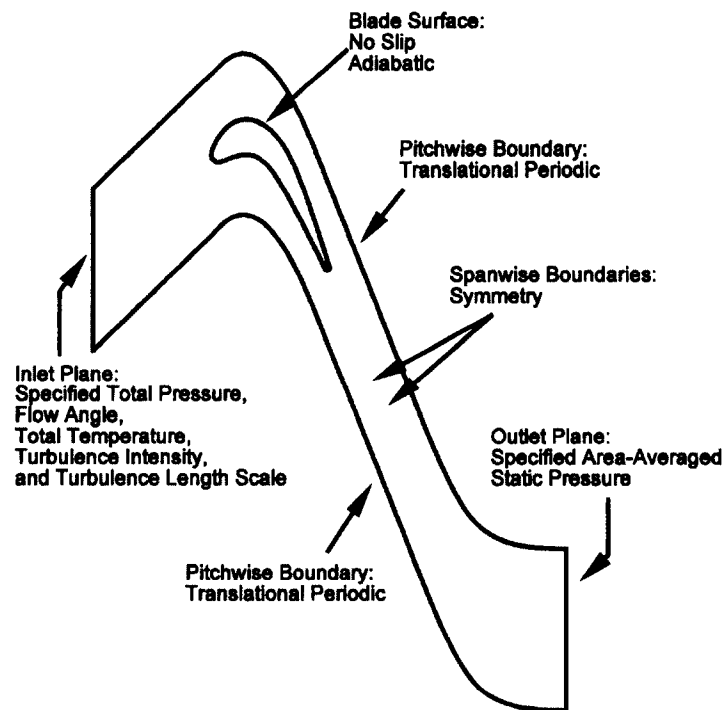


Figure 5.4 Boundary Conditions Used in the Simulations

5.3.4 Turbulence Model

The turbulence model used in these simulations is the shear stress transport model. This is a two-equation model based on the $k-\omega$ model near the blade surface and the $k-\epsilon$ model in the freestream, meaning it solves transport equations for the turbulent kinetic energy (k) throughout the flow, the turbulent frequency (ω) near

the wall, and the turbulent dissipation (ϵ) in the freestream. The transition between laminar and turbulent flow was modelled using the gamma-theta model in CFX (Langtry and Menter 2005). This model solves two additional transport equations – one for intermittency, and one for the critical momentum thickness Reynolds number, Re_{θ_t} . The value of Re_{θ_t} is compared to the estimated momentum thickness Reynolds number at every node to determine whether or not transition has occurred. This model uses an empirical correlation developed by Langtry and Menter (2005).

While the turbulence intensity was set equal to 4% at the inlet plane, early simulations were affected by a rapid dissipation of the turbulent kinetic energy. Figure 5.5 shows the turbulence intensity along the periodic boundary from the inlet plane to the leading edge of the blade for a simulation which used the default setting for medium turbulence in CFX which specifies a turbulence intensity of 5% and an eddy viscosity ratio of 10. This resulted in a length scale below 0.1mm. The turbulence intensity decays to about a quarter of the inlet value by the time it reaches the leading edge of the blade. This was corrected by specifying the length scale as being 15.24mm. The length scale (l_t) is related to the turbulent dissipation rate by

$$\epsilon = \frac{k^{\frac{3}{2}}}{l_t} \quad 5.2$$

Figure 5.6 shows the behaviour of the turbulence intensity along the periodic boundary from the inlet plane to the leading edge of the blade for the simulation

with a Mach number of 0.77 and Reynolds number of 664,000. This behaviour is typical of all results. It should be noted that the reduction in turbulence intensity in Figure 5.6 is largely a result of the accelerated flow, rather than a reduction in the turbulent kinetic energy. The turbulence parameters were selected based on the measurements by Corriveau (2005). While these measurements may not exactly match the values in the experiment, they are expected to be close.

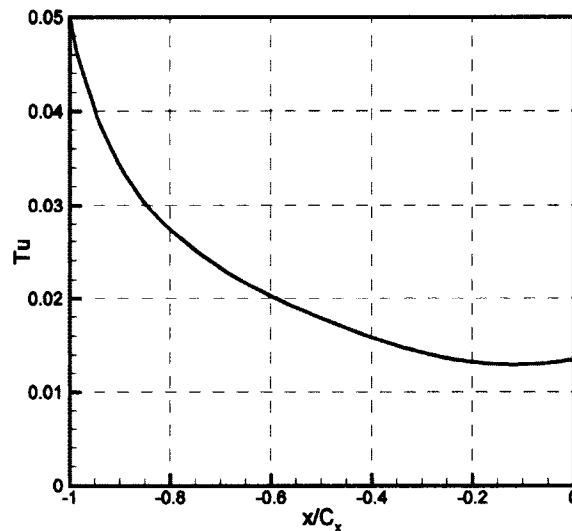


Figure 5.5 Turbulence Intensity at Inlet of the Fluid Domain Using the CFX Default Settings

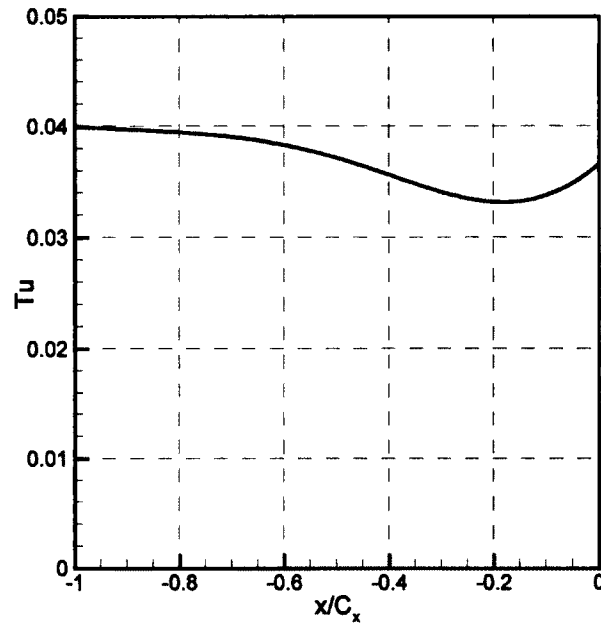


Figure 5.6 Turbulence Intensity at Inlet of the Fluid Domain Using Appropriate Settings

5.4 Mach Number Effects at a Fixed Reynolds Number

5.4.1 Introduction

This section outlines the results of the simulations with a fixed Reynolds number of 611,000. These results will demonstrate the influence of the Mach number from 0.05 to 0.98 independent of the Reynolds number effects.

5.4.2 Blade Loadings

The computed blade loadings for fixed Reynolds number cases are shown in Figure 5.7. At low Mach numbers, this blade profile has a single suction peak at about $0.35 C_x$. As the Mach number is raised, a second suction peak begins to develop shortly after $0.60 C_x$. Figure 5.8 shows the pressure distribution at Mach 0.64 where the second suction peak is beginning to develop. Above a Mach number of 0.6 this suction peak is followed by a short region where the isentropic Mach number drops quickly. This region corresponds to the location where the boundary layer is in transition from laminar to turbulent flow. While a plateau followed by a rapid drop in the surface pressure can often indicate the presence of a separation bubble, close examination of the vector field shows there is no flow reversal below Mach 0.89. The fact that the blade loadings suggest flow separation for many cases which did not separate can be explained by examining the boundary layer. This is discussed further in Section 5.4.3.

The cases at or above $M_2 = 0.89$ all had small separation bubbles. For example, the separation bubble at Mach 0.89 corresponds to the region at $0.8 C_x$ in Figure 5.9 where the shear stress is negative. This also corresponds to the region in Figure 5.10 where the pressure rises rapidly on the suction side of the blade. The contours of density gradient indicate there is a shock at this location.

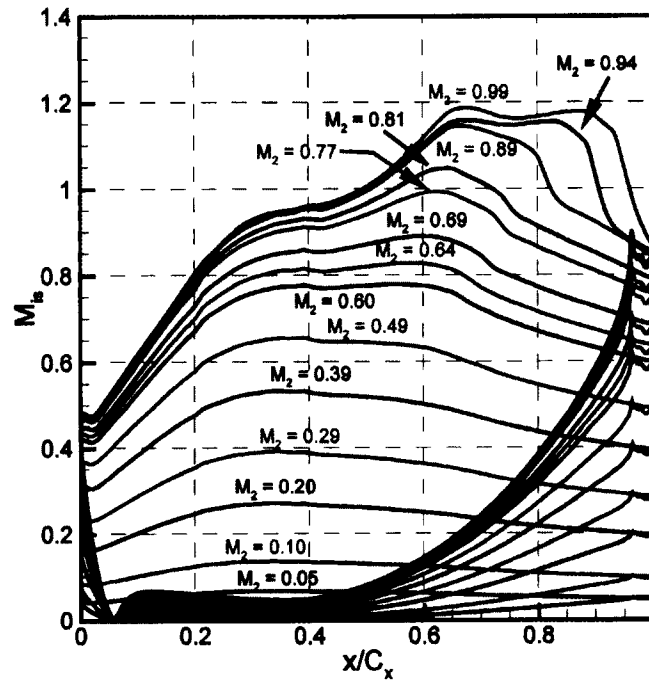


Figure 5.7 Blade Surface Isentropic Mach Numbers for the Fixed Reynolds Number of 611,000

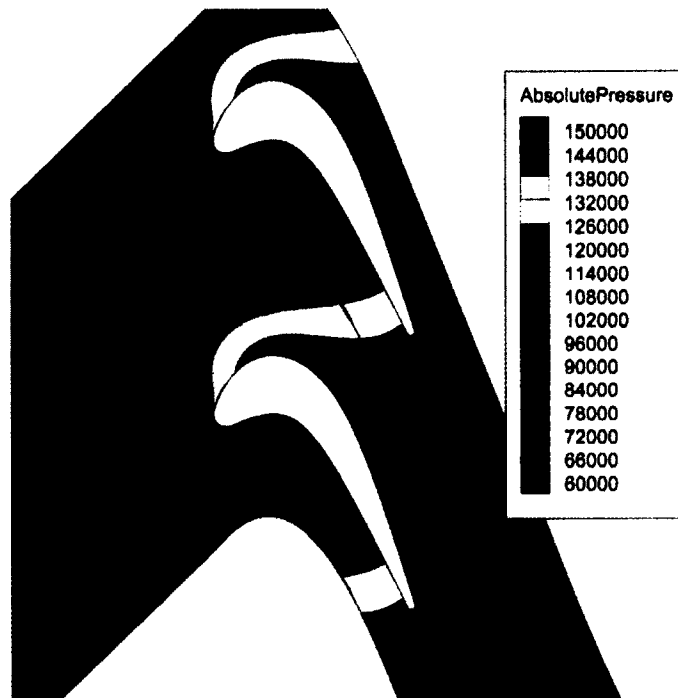


Figure 5.8 Pressure Distribution at Mach 0.64

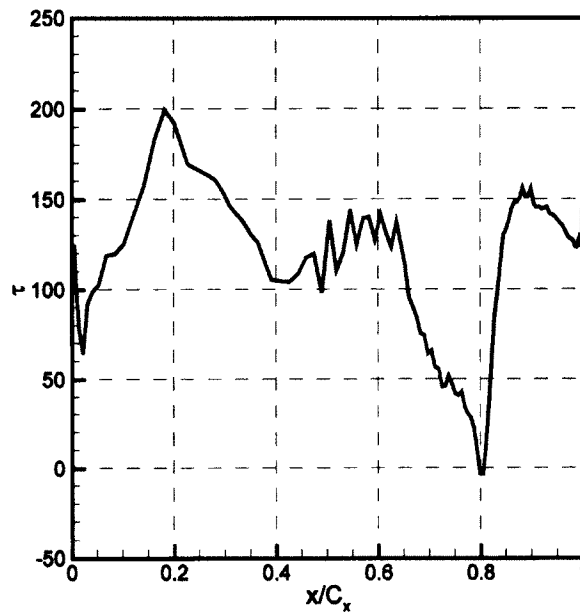


Figure 5.9 Shear Stresses Demonstrating Separation at Mach 0.89

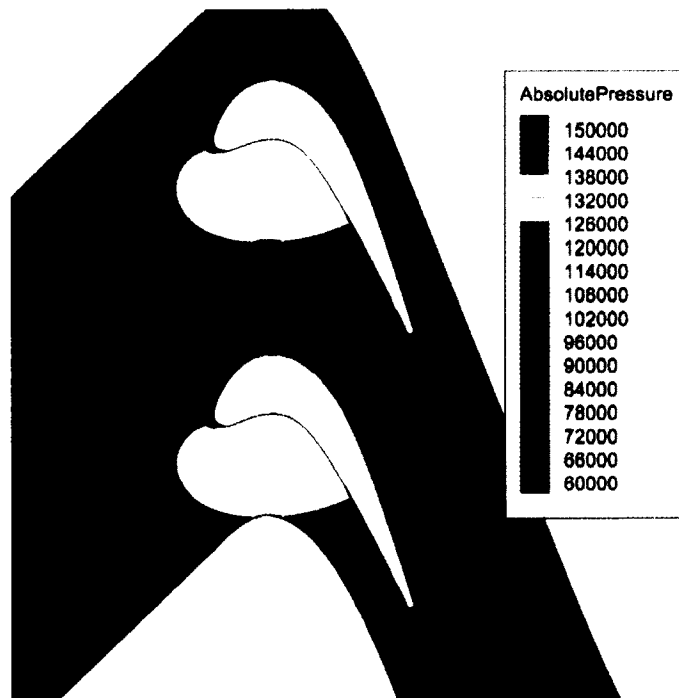


Figure 5.10 Pressure Distribution at Mach 0.89 with Contour Lines Indicating Density Gradients

5.4.3 Boundary Layer Properties

For most of the fixed Reynolds number simulations there is no reversed flow. However, the blade loadings suggest the presence of a separation bubble. This can be explained by looking at the nature of the boundary layer. Three aspects of the boundary layer are considered: displacement thickness, shape factor, and the transition location. The displacement thickness indicates the distance that the inviscid flow outside the boundary layer is displaced by the boundary layer, and therefore indicates the effective shape of the blade which determines the pressure distribution. The displacement thickness is defined as

$$\delta^* = \int_0^{y_e} \left(1 - \frac{\rho u}{\rho_e u_e}\right) dy \quad 5.3$$

where e denotes a value taken at the edge of the boundary layer.

The integration was performed through the inflation layer of the mesh from the blade surface to the location of maximum velocity. Because the inflation layer is not perfectly normal to the blade surface at all points, this means the calculated displacement thickness will have some extra uncertainty. However the inflation layer is close enough to being normal that the results will not be negatively affected. The shape factor is used to give an indication of the fullness of the velocity profile, as well as indicating if it is likely to have separated. The shape factor is defined as

$$H = \frac{\delta^*}{\theta} \quad 5.4$$

where θ is the momentum thickness which is defined as

$$\theta = \int_0^{y_e} \frac{\rho u}{\rho_e u_e} \left(1 - \frac{u}{u_e}\right) dy \quad 5.5$$

The momentum thickness is integrated in the same manner as the displacement thickness, and thus has the same associated uncertainty. In zero pressure gradient, laminar flow has a shape factor of 2.6, and turbulent flow has a shape factor of about 1.4. Laminar separation usually occurs around a shape factor of 3.5, and turbulent separation usually occurs around a shape factor of 2.4. Finally, the transition location indicates where the boundary layer has transitioned from laminar to turbulent flow. While transition occurs over a region of the blade surface, the transition location was estimated by locating the point in the boundary layer where the turbulent intermittency at the blade surface reaches a threshold value of 0.035. While it might seem intuitive to define the transition location as the location where the turbulent intermittency becomes greater than 0, the value of 0.035 was selected because CFX outputs a turbulent intermittency of 0.02 at the wall of a laminar boundary layer. This method was found to be consistent with the behaviour of the shape factor, shear stress, and turbulent kinetic energy for all simulations.

Figure 5.11 shows the influence of the Mach number on the transition location for the fixed Reynolds number set. This shows that the higher Mach numbers, which are closer to separation, transition to turbulent flow further downstream. Moreover, the Mach number clearly has a significant effect on the transition location, changing the transition location by over 37% of the axial chord between Mach numbers of 0.05 and 0.98.

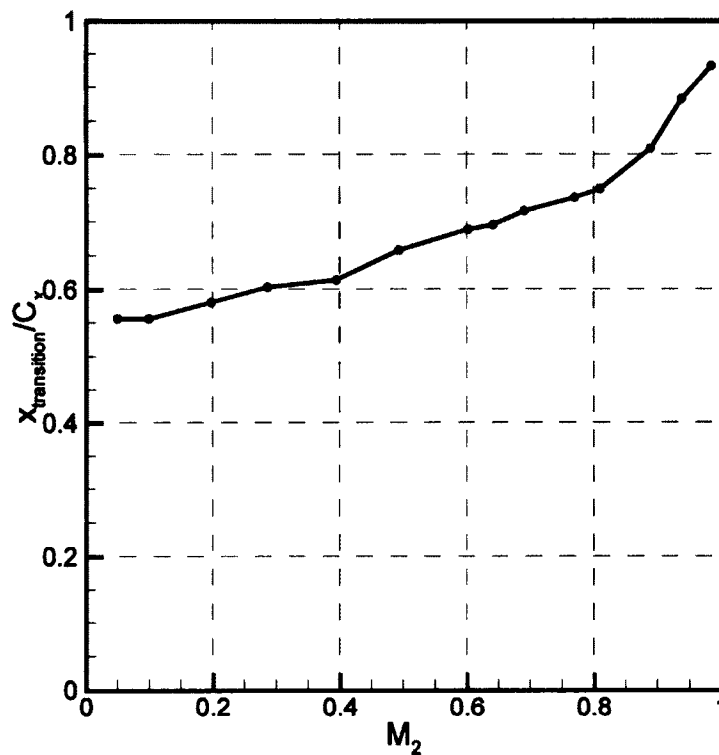


Figure 5.11 Transition Location at a Constant Reynolds Number of 611,000

Figure 5.12 shows the displacement thickness and shape factor on the suction surface at a Mach number of 0.77 with the transition location indicated by the dashed line. While the flow has not separated, the peak in displacement thickness at about $0.73C_x$ – just before the transition location – indicates that the inviscid flow is nonetheless displaced from the surface in this region. This peak is reflected in the shape factor, which suggests that the flow is approaching separation. This can be seen in Figure 5.13 which shows the velocity profile of the boundary layer at this location.

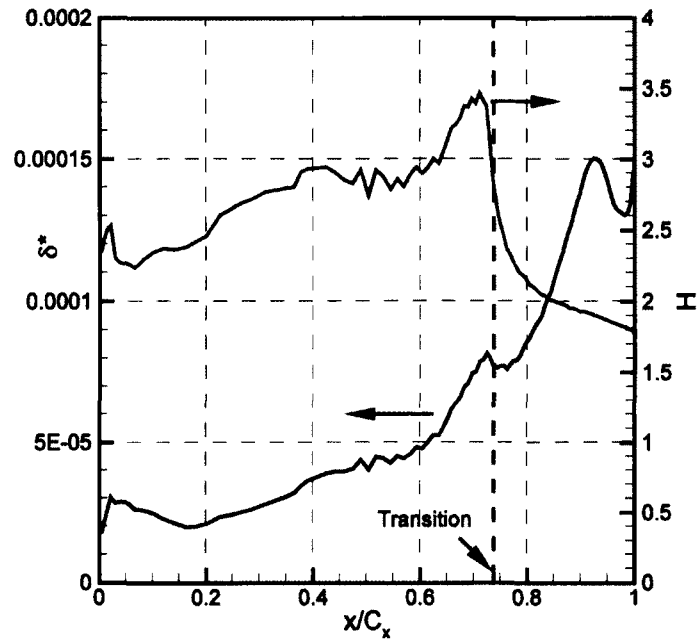


Figure 5.12 Displacement Thickness and Shape Factor at a Mach Number of 0.77 and Reynolds Number of 611,000

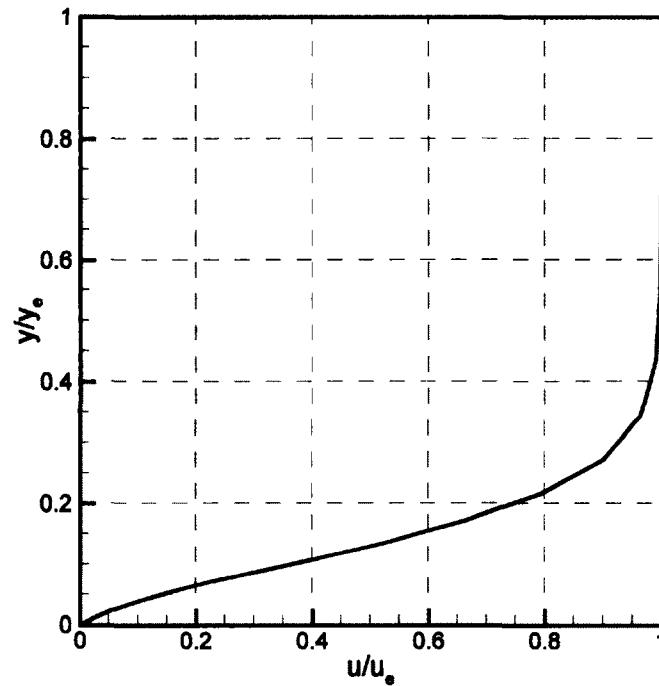


Figure 5.13 Velocity Profile at the Location of Maximum Shape Factor at a Mach Number of 0.77 and Reynolds number of 611,000

Figures 5.14 and 5.15 show the displacement thickness and shape factor on the suction surface for a few selected Mach numbers. The location of the displacement thickness peak which was located at $0.73 C_x$ in Figure 5.12 is seen to shift downstream along with the transition location as the Mach number increases, demonstrating that this boundary layer behaviour is not a result of the geometry producing deceptive results. The peak in the shape factor at $0.75 C_x$ levels off for the case with the Mach number of 0.89. This corresponds to the fact that this case has a small region of reversed flow. The lower Mach numbers, which did not have the features in the blade loadings that indicate flow separation, do not have the same peak in the shape factor as the higher Mach numbers.

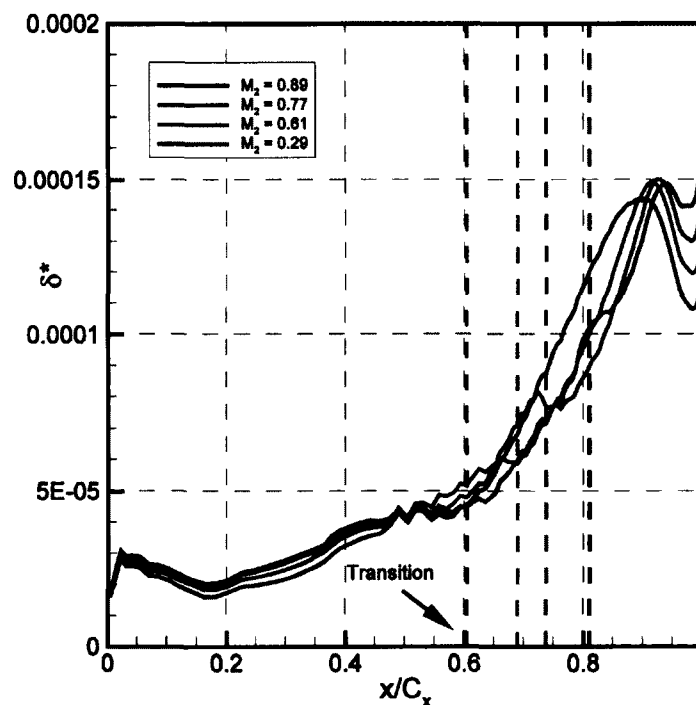


Figure 5.14 Displacement Thickness at a Constant Reynolds Number of 611,000

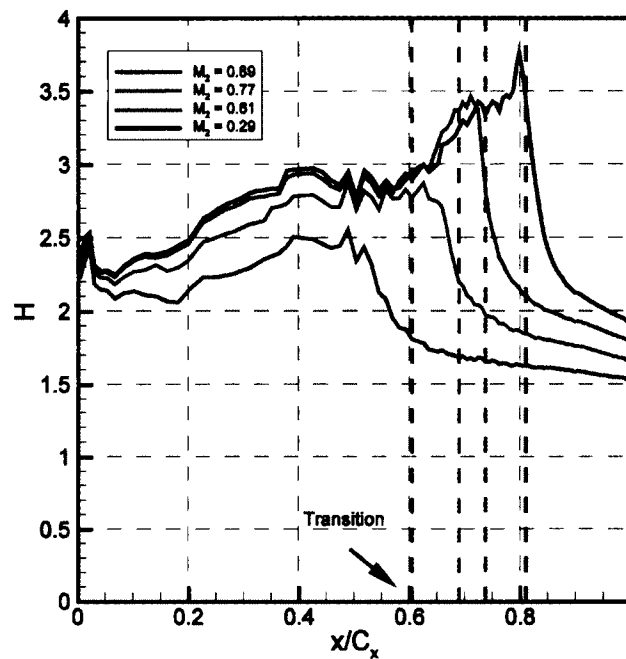


Figure 5.15 Shape Factor at a Constant Reynolds Number of 611,000

5.4.4 Losses

Figure 5.16 shows the influence of Mach number on the mixed-out total pressure loss coefficient for the fixed Reynolds number cases. With the Reynolds number fixed, the loss coefficient stays largely unchanged up to a Mach number of 0.89. Since the entropy generated in a boundary layer is proportional to the cube of the boundary layer edge velocity (Denton 1993), it seems reasonable that the second suction peak seen in the blade loadings would result in a rise in loss coefficient. However, as the transition location moves downstream, the portion of the blade wetted by laminar flow increases. Since an attached laminar boundary layer will generate less loss than an attached turbulent boundary layer, the loss

coefficient would be expected to decrease. Above $M_2 = 0.89$, the total pressure loss coefficient rises rapidly due to the appearance of shocks within the flow. Thus the influence of Mach number on total pressure loss coefficient appears to be a balance between the increased losses due to blade loading and the decreased losses due to the boundary layer moving downstream prior to the onset of shocks within the blade passage. The influence of the Mach number on the total pressure loss coefficient is not very pronounced in the fixed Reynolds number cases below a Mach number of 0.89.

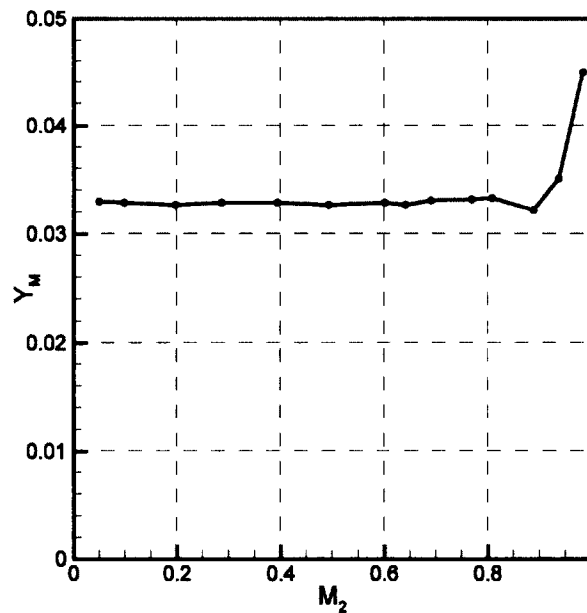


Figure 5.16 Total Pressure Loss Coefficient at a Constant Reynolds Number of 611,000

5.4.5 Flow Angles

The exit flow angle variation with Mach number for the fixed Reynolds number cases is shown in Figure 5.17. At the incompressible limit, the exit flow angle levels off at about 68.4° . As the Mach number rises to a value of 0.94, the exit flow angle increases as well. This is the expected trend, and can be largely explained by the increased blade loading at higher Mach numbers. The exit flow angle decreases by 0.15° from $M_2 = 0.94$ to 0.98. This is attributed to the effects of the separation bubble on the flow turning.

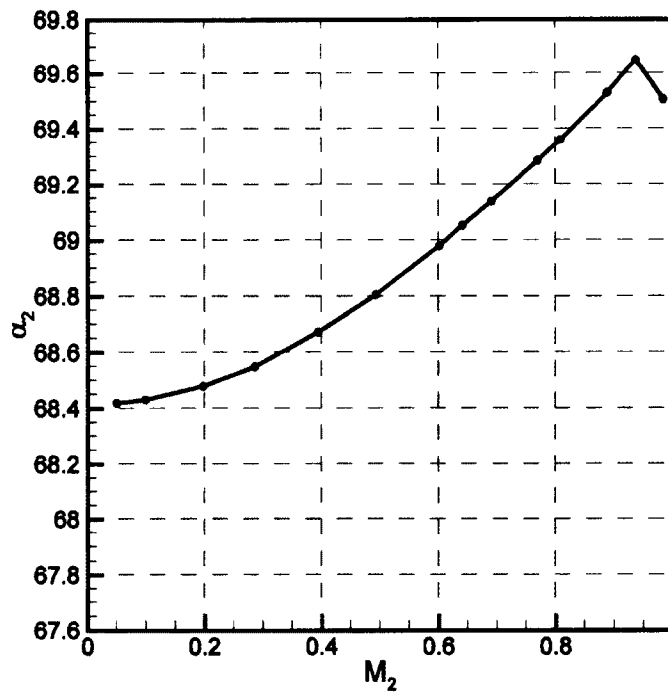


Figure 5.17 Exit Flow Angle at a Constant Reynolds Number of 611,000

5.4.6 Wake Profiles

The wake profiles for the fixed Reynolds number cases are shown in Figure 5.18. These wake profiles were extracted at the $1.4 C_x$ plane. The centre of the wake shifts in the direction of the pressure side of the blade as the Mach number is raised. This is a result of the wake convecting further in this direction due to the exit flow angle variation with the Mach number. The small region where the total pressure loss is negative, suggesting a decrease in entropy, is commonly seen in CFD results. The exact cause is uncertain, but it has been attributed both to real physical phenomena such as total temperature redistribution, and computational error such as approximations within the turbulence model. While the total pressure across the wake changes more rapidly on the suction side, this is because the wake profile data is extracted in the pitchwise direction, not normal to the flow direction. Because the suction side of the wake profile is not as far downstream of the blade as the pressure side, the wake profile indicates that less mixing has occurred on the suction side.

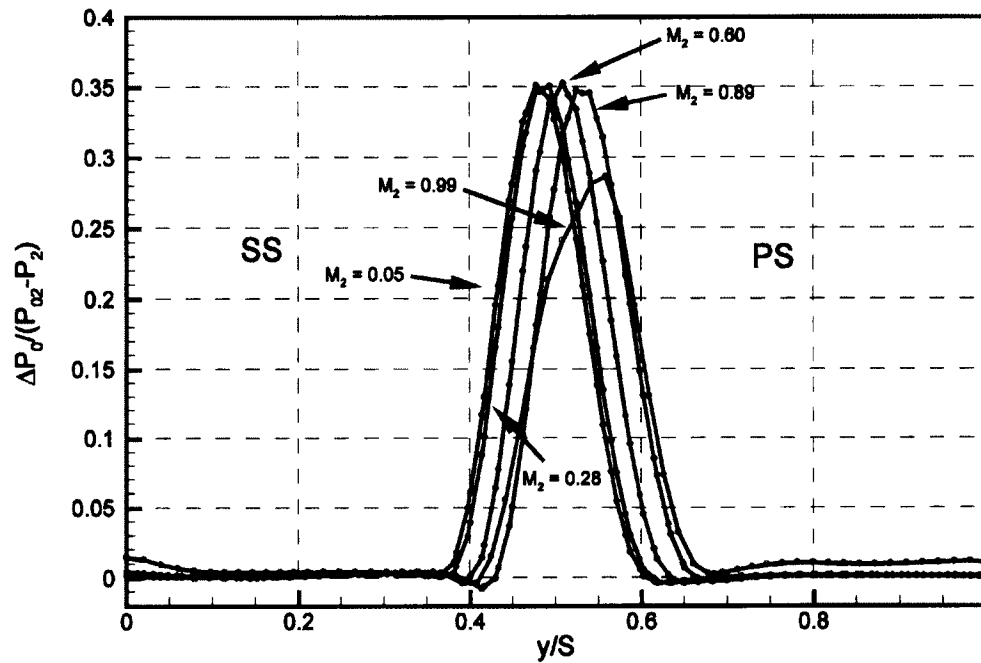


Figure 5.18 Wake Profiles at $1.4 C_x$ for a Constant Reynolds Number of 611,000

5.5 Reynolds Number Effects at a Fixed Mach Number

5.5.1 Introduction

This section outlines the results of the simulations with a fixed Mach number. These results will demonstrate the influence of Reynolds number on the flow independent of Mach number effects. The range of the Reynolds number is 200,000 to 1,000,000. These simulations were run for the Mach numbers of 0.49 and 0.77.

5.5.2 Blade Loadings

The blade loadings for the two fixed Mach number cases are shown in Figure 5.19. The arrow indicates the direction of Reynolds number increasing between 200,000 and 1,000,000. The Reynolds number only affects the blade loadings in the region of transition. Figures 5.18 and 5.19 show this region in greater detail for Mach numbers of 0.49 and 0.77 respectively. While pressure variation is consistent with a separation bubble that varies in size with Reynolds number, close inspection of the vector field indicates that the flow remains attached. The observed pressure variation is explained in Section 5.5.3.

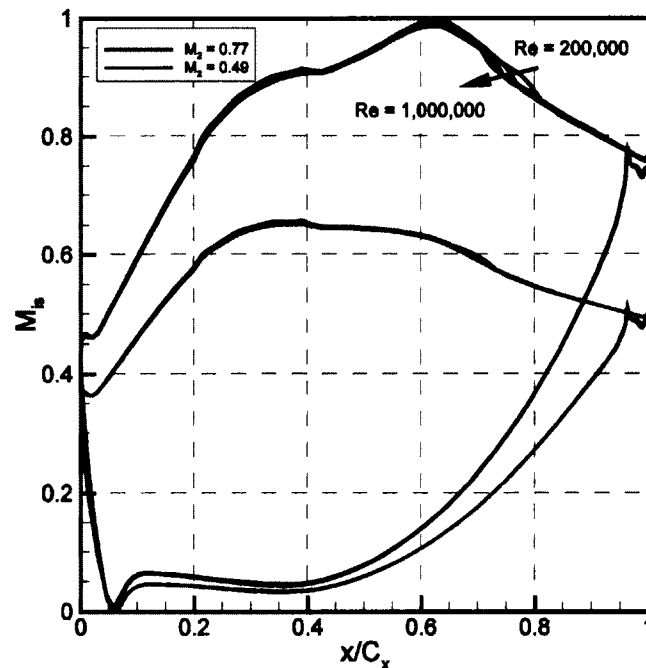


Figure 5.19 Isentropic Surface Mach Numbers at Constant Mach Numbers of 0.49 and 0.77

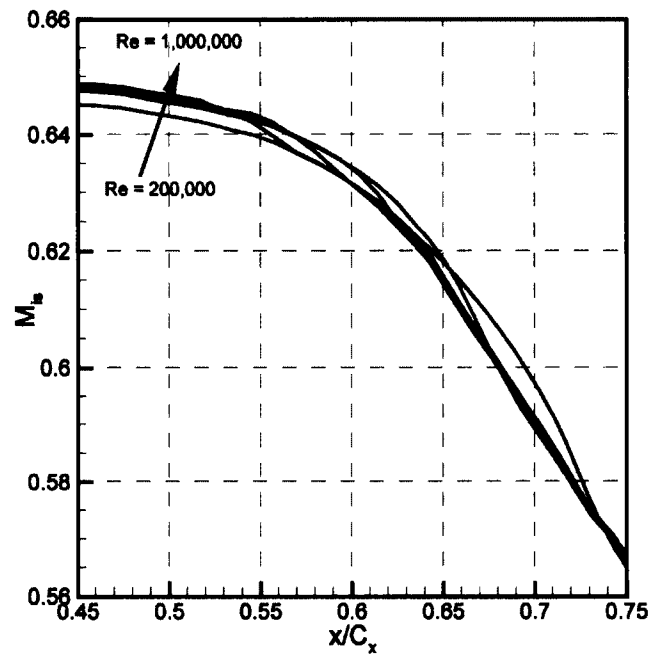


Figure 5.20 Detailed View of the Isentropic Surface Mach Numbers after the Suction Peak at an Exit Mach Number of 0.49

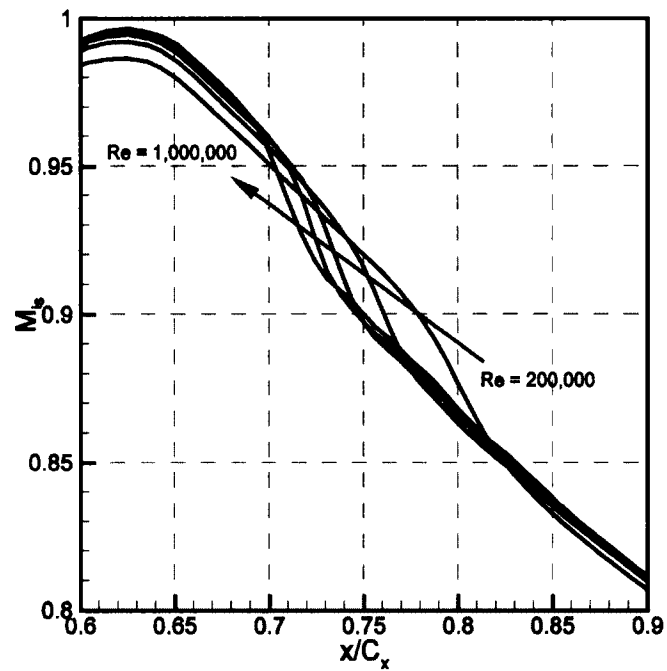


Figure 5.21 Detailed View of the Isentropic Surface Mach Numbers after the Suction Peak at an Exit Mach Number of 0.77

5.5.3 Boundary Layer Properties

Figure 5.22 shows the influence of the Reynolds number on the transition location for the fixed Mach number. The effect of increasing the Reynolds number at fixed Mach number is to cause an earlier transition. Increasing the Reynolds number from 200,000 to 1,000,000 moves the transition location upstream by about 15% and 10% of the axial chord for the exit Mach numbers of 0.49 and 0.77 respectively. This shows that the effect of Reynolds number on the transition location decreases at higher Mach numbers.

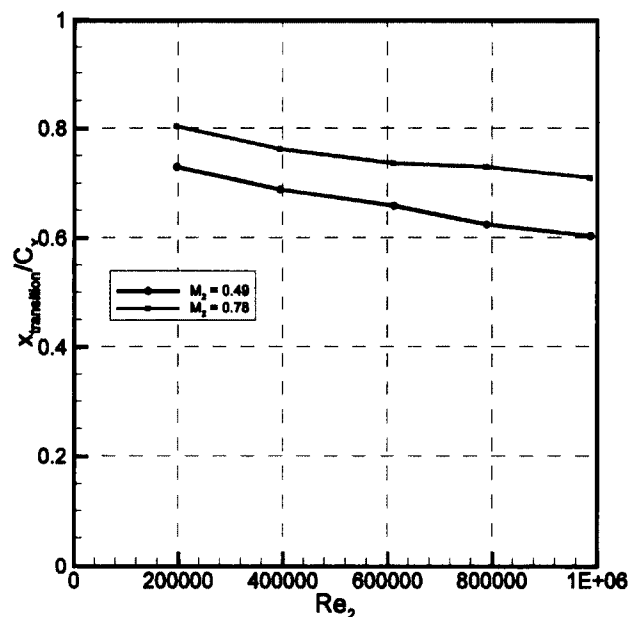


Figure 5.22 Influence of Reynolds Number on Transition Location for Constant Mach Numbers of 0.49 and 0.77

Figures 5.23 and 5.24 show the displacement thickness on the suction surface at Mach numbers of 0.49 and 0.77 respectively. Of particular importance is

the peak in displacement thickness before the transition. This peak will displace the inviscid flow, resulting in a modified pressure distribution that resembles a separation bubble as seen in Figure 5.22. At a Mach number of 0.49, this peak is clearly present at the Reynolds number of 200,000 at $0.72 C_x$. At a Mach number of 0.77, the peak in displacement thickness before the transition shifts upstream from 0.80 to $0.68 C_x$ as the Reynolds number increases from 200,000 to 1,000,000. Compared to the results in Section 5.4.3, the displacement thickness appears to be more strongly dependent on the Reynolds number than the Mach number within the range investigated. For example, the displacement thickness at $0.4 C_x$ increases by a factor of 2.20 from a Reynolds number of 1,000,000 to 200,000 at $M_2 = 0.49$ while increasing the Mach number from 0.29 to 0.89 only increases the displacement thickness at $0.4 C_x$ by a factor of 1.16.

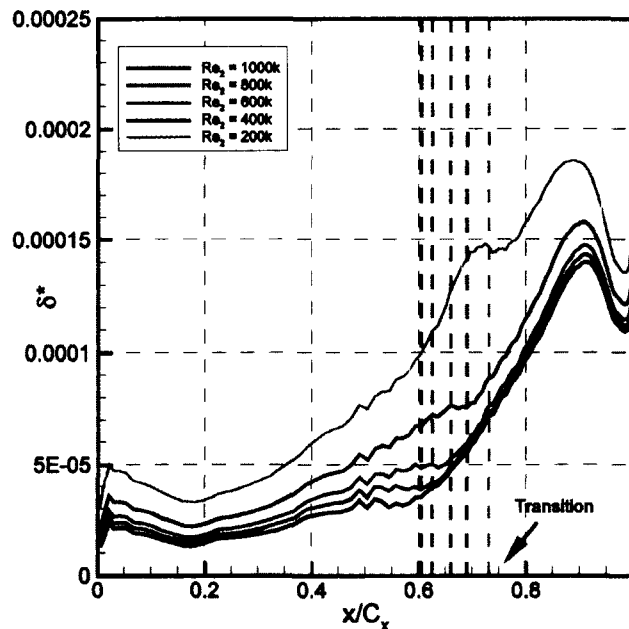


Figure 5.23 Displacement Thickness Variation at a Constant Mach Number of 0.49

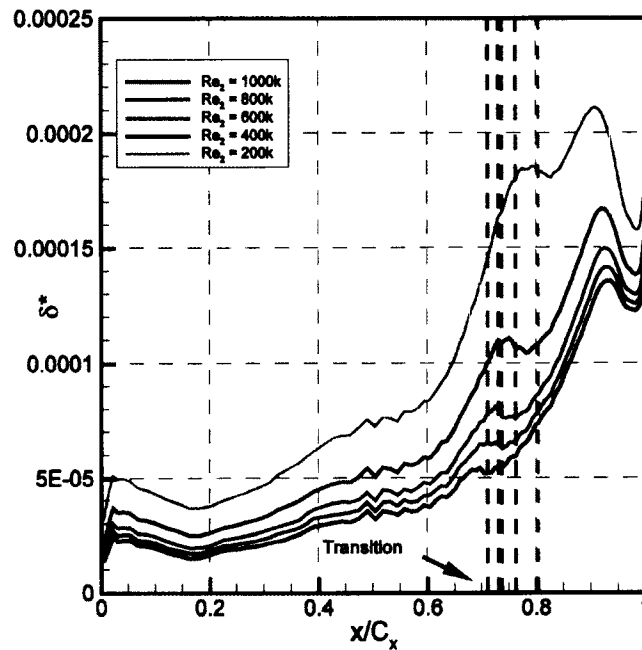


Figure 5.24 Displacement Thickness Variation at a Constant Mach Number of 0.77

Figures 5.25 and 5.26 show the shape factor on the suction surface at Mach numbers of 0.49 and 0.77 respectively. These figures show a peak in the shape factor where the flow is close to separation. At a Mach number of 0.49 the shape factor peak is not present for most of the Reynolds numbers; however, the shape factor peak is clearly present at the lowest Reynolds number for this Mach number at $0.68 C_x$. For the Mach number of 0.77 the peak in the shape factor decreases with increasing Reynolds number. At this Mach number the peak in shape factor shifts from 0.76 to $0.68 C_x$ as the Reynolds number increases from 200,000 to 1,000,000. The fact that this boundary layer is approaching separation can be seen in Figure 5.27 which shows the velocity profile of the boundary layer at $0.76 C_x$ for the Mach number of 0.77 and Reynolds number of 200,000.

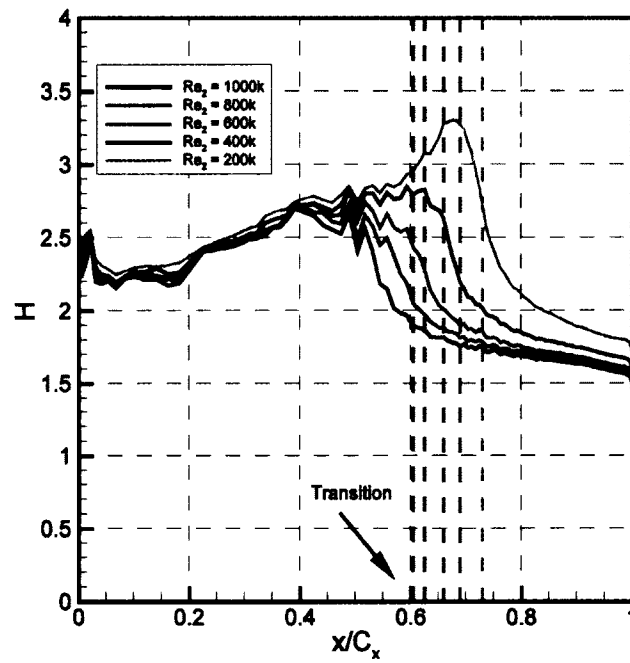


Figure 5.25 Shape Factor Variation at a Constant Mach Number of 0.49

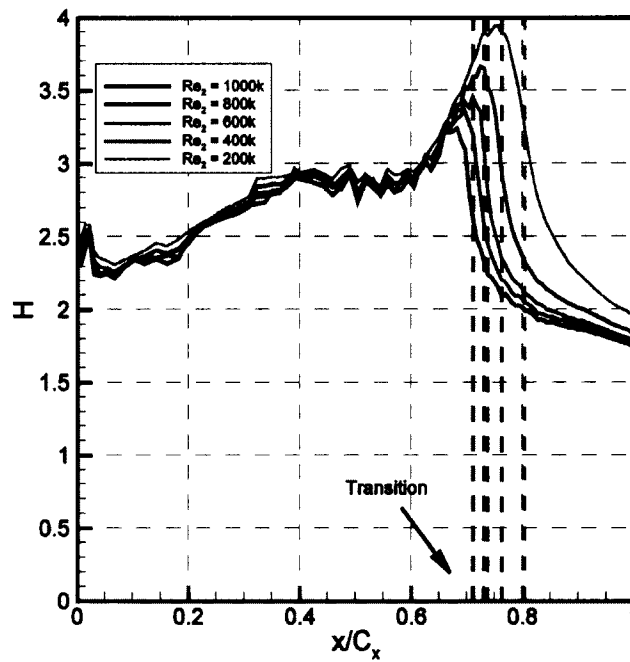


Figure 5.26 Shape Factor Variation at a Constant Mach Number of 0.77

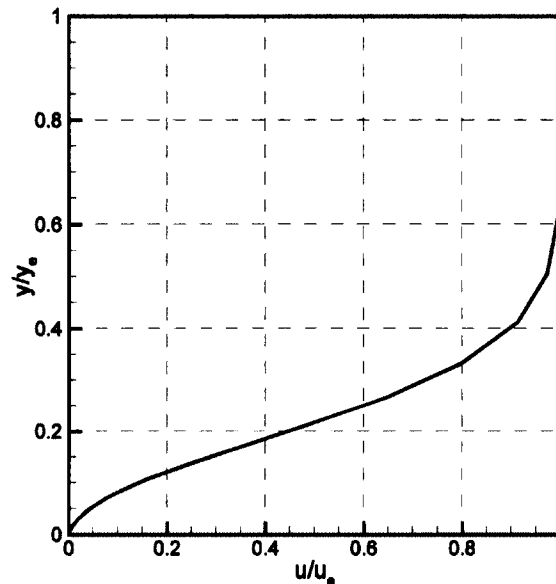


Figure 5.27 Velocity Profile at the Location of the Maximum Shape Factor for a Mach Number of 0.77 and Reynolds Number of 200,000

5.5.4 Losses

The influence of the Reynolds number on the mixed-out total pressure loss coefficient for the fixed Mach number simulations is shown in Figure 5.28. The decrease in losses with increasing Reynolds number matches the expected results since an increased Reynolds number means the viscous forces will be less significant. For both Mach numbers, the losses decrease from about 0.04 to about 0.031 as the Reynolds number is increased from 200,000 to 1,000,000. The close match of the two Mach numbers suggests that the influence of the Reynolds number on the total pressure loss coefficient is not strongly affected by the Mach number below $M_2 = 0.77$. While this result is expected to be valid at Mach numbers lower than 0.49, it is expected to change for higher Mach numbers where the presence of

shock waves will complicate the flow. Further, this result will only be valid where the transition location does not strongly affect the total pressure loss coefficient since the effect of Reynolds number on transition location was seen to change with Mach number, as shown in Section 5.5.3. These results demonstrate that the losses will change significantly between Reynolds numbers of 200,000 and 1,000,000.

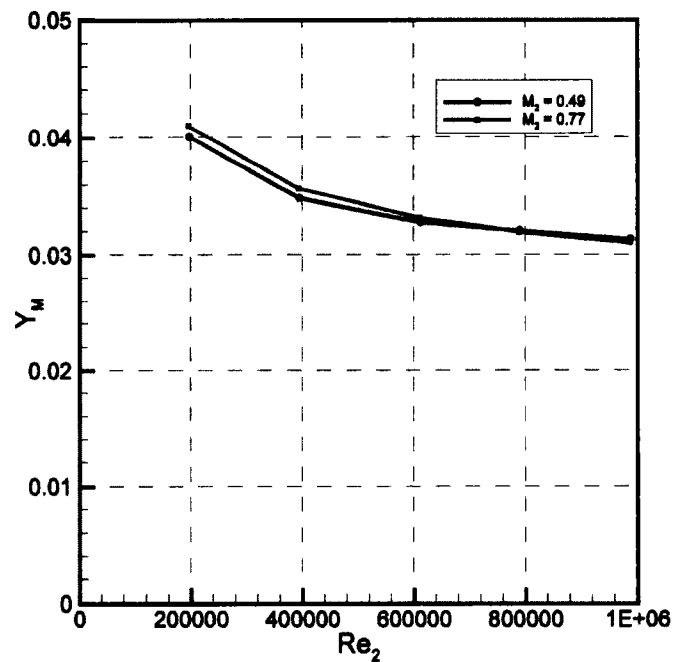


Figure 5.28 Total Pressure Loss Coefficient at Constant Mach Numbers of 0.49 and 0.77

5.5.5 Flow Angles

The Reynolds number does not significantly affect the exit flow angle for the fixed Mach number cases. For the range of Reynolds numbers examined, the change in exit flow angle is within $\pm 0.005^\circ$ for a given Mach number. This can be seen in

Figure 5.29. This demonstrates that the exit flow angle of a cascade is independent of Reynolds number within the range tested. This conclusion is only expected to be valid while the flow remains attached.

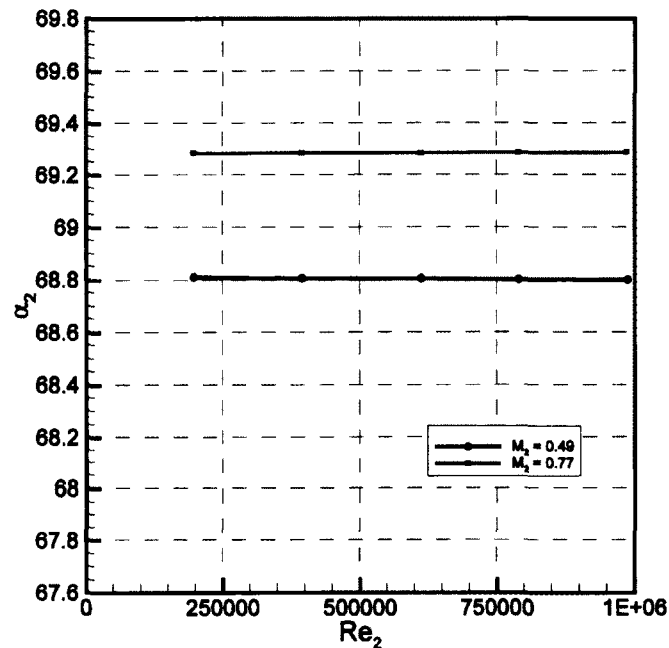


Figure 5.29 Influence of Reynolds Number on Exit Flow Angle for Constant Mach Numbers of 0.49 and 0.77

5.5.6 Wake Profiles

The wake profiles for the fixed Mach number simulations are shown in Figure 5.30. The direction of increasing Reynolds number is indicated by the arrow. As the Reynolds number increases from 200,000 to 1,000,000, the wakes get narrower and shallower. This agrees with the trend of decreased losses at increased Reynolds number. At the Reynolds number of 200,000 the wakes are more pronounced on the suction side. This is expected since the increase in the

suction side boundary layer thickness, as seen in Section 5.5.3, will increase the contribution to the losses from the suction side.

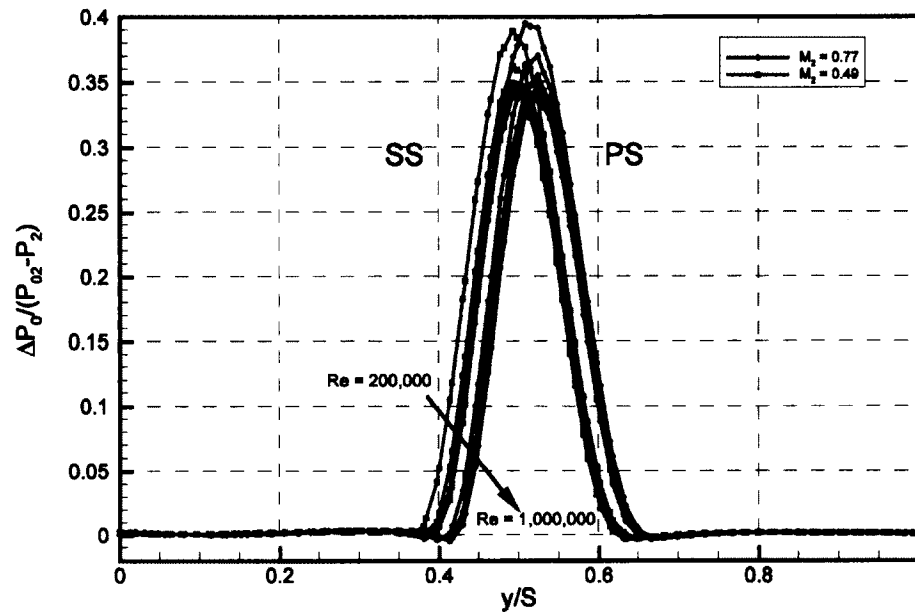


Figure 5.30 Wake Profiles at 1.4 C_x for Constant Mach Numbers of 0.49 and 0.77

5.6 Combined Mach Number and Reynolds Number Effects Corresponding to a Fixed Exit Pressure

5.6.1 Introduction

This section outlines the results of the simulations which varied the Mach number with a Reynolds number corresponding to a fixed exit pressure of 1atm. These results are intended to approximate the results in the wind tunnel which operates in a similar manner. Additional simulations were run after the experiment

to match the experimental operating points. However, since these additional simulations lead to the same conclusions, only the results of the simulations which approximated the wind tunnel conditions with a constant exit pressure will be discussed. The range of the Mach number in the simulations is 0.2 to 0.89, while the range of the Reynolds number is 150,000 to 800,000. These results will mostly be used to separate the Mach number effects from the Reynolds number effects in the wind tunnel results.

5.6.2 Blade Loadings

As discussed in Sections 5.4.2 and 5.5.2, the blade loading distributions depend strongly on the exit Mach number, and are almost entirely independent of Reynolds number effects. This is clearly seen in Figure 5.31 which compares the blade loadings for the simulations which varied the Mach number independent of Reynolds number and the simulations which approximated the wind tunnel conditions. The two sets of simulations show very little difference in the blade loadings.

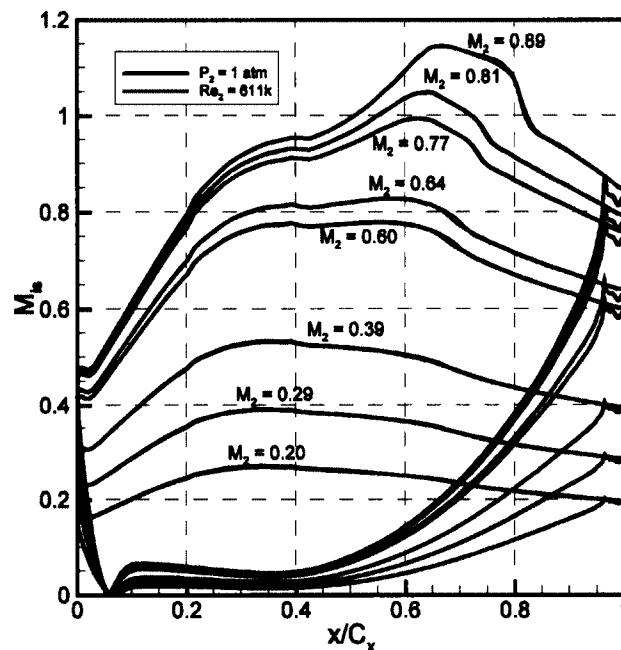


Figure 5.31 Comparison of Blade Loadings for Constant Reynolds Number of 611,000 and Simulations which Approximated Wind Tunnel Conditions

5.6.3 Boundary Layer Properties

Figures 5.32 and 5.33 compare the transition location for the simulations approximating the wind tunnel conditions to the simulations with a fixed Reynolds number and to the simulations with fixed Mach numbers respectively. In Figure 5.32 the transition location is nearly identical for the two sets of simulations above $M_2 = 0.7$ where the simulations approximating wind tunnel conditions are above a Reynolds number of 600,000. For this blade geometry, the transition location is mostly constant for the simulations approximating wind tunnel conditions as the Mach number is reduced below 0.5, where the Reynolds number is below 400,000. Figures 5.32 and 5.33 demonstrate that this is the net result of the lower Mach

number promoting earlier transition while the lower Reynolds number acts to delay the transition.

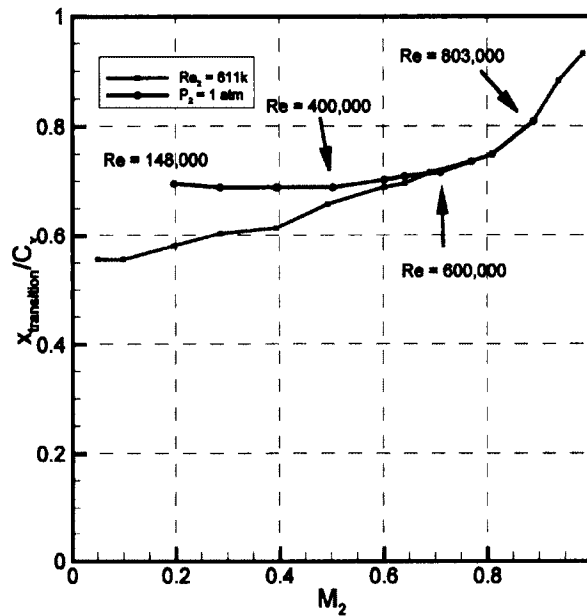


Figure 5.32 Transition Location for a Constant Reynolds Number of 611,000 Compared to the Simulations which Approximated Wind Tunnel Conditions

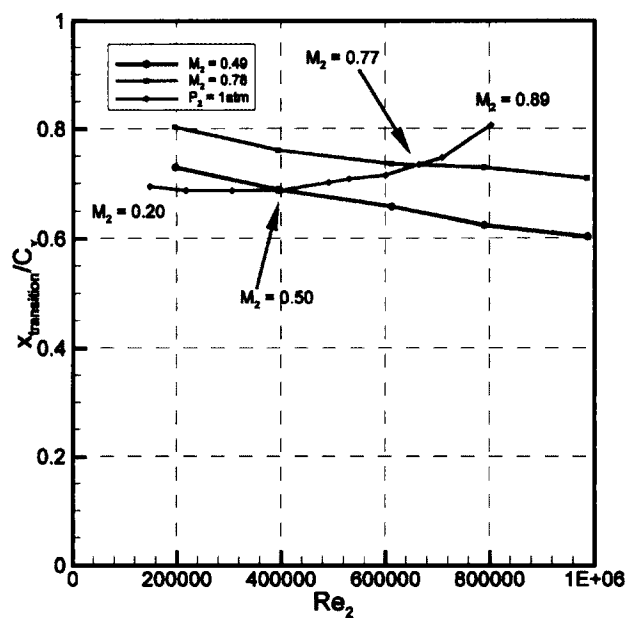


Figure 5.33 Transition Location for Constant Mach Numbers of 0.49 and 0.77 Compared to the Simulations which Approximated Wind Tunnel Conditions

Figure 5.34 shows the displacement thickness on the suction surface for a few selected Mach numbers from the set approximating wind tunnel conditions. Sections 5.4.3 and 5.5.3 demonstrate that the displacement thickness is more strongly dependent on the Reynolds number than the Mach number in the range of these simulations. This suggests the results in Figure 5.34 are primarily due to the change in Reynolds number. However, there is a peak in the displacement thickness just before the transition location. Since the Mach number and Reynolds number have a similar influence on the transition location, this feature of the displacement thickness is affected similarly by the Mach number and Reynolds number.

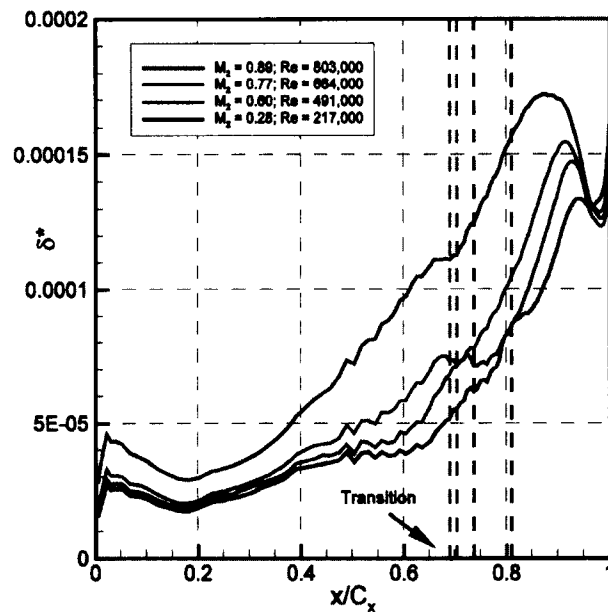


Figure 5.34 Variation of Displacement Thickness for the Simulations Approximating Wind Tunnel Conditions

Figure 5.35 shows the shape factor on the suction surface for a few selected Mach numbers from the set approximating wind tunnel conditions. Of particular

importance is whether or not there is a peak in the shape factor just before transition. Sections 5.4.3 and 5.5.3 indicate that the cases with such a peak are close to separation. Figure 5.35 clearly shows the presence of this peak at the higher Mach numbers. Since the cases with higher Mach number will also have a higher Reynolds number, and since an increased Reynolds number will delay separation, the presence of this shape factor peak in the simulations approximating wind tunnel conditions can be attributed to the effects of Mach number.

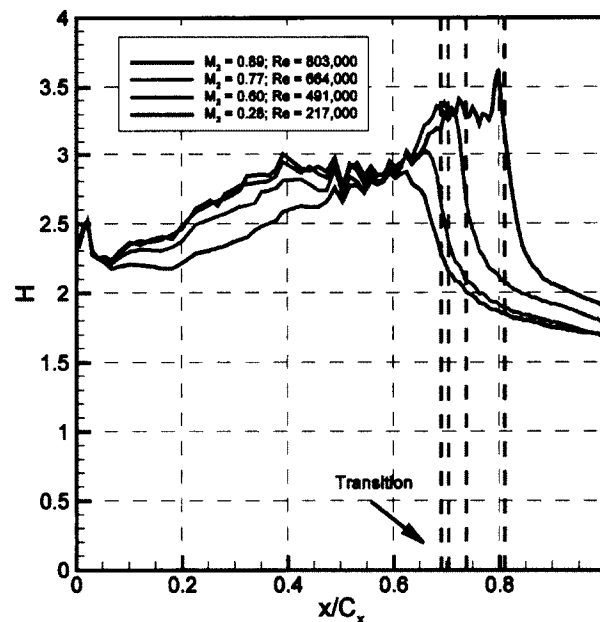


Figure 5.35 Variation of Shape Factor for the Simulations Approximating Wind Tunnel Conditions

5.6.4 Losses

As discussed in Sections 5.4.4 and 5.5.4, the total pressure loss coefficient depends more strongly on the Reynolds number than on the exit Mach number

within the range simulated. Figure 5.36 shows the variation of the mixed-out total pressure loss coefficient with Reynolds number for the simulations approximating wind tunnel conditions and the simulations with constant Mach numbers of 0.49 and 0.77. The simulations show similar trends in the total pressure loss coefficient. Figure 5.37 shows the variation of the mixed-out total pressure loss coefficient with Mach number for the simulations approximating wind tunnel conditions and the simulations with a constant Reynolds number of 611,000. This demonstrates the error that can arise from simply accepting that the wind tunnel results represent the Mach number effects.

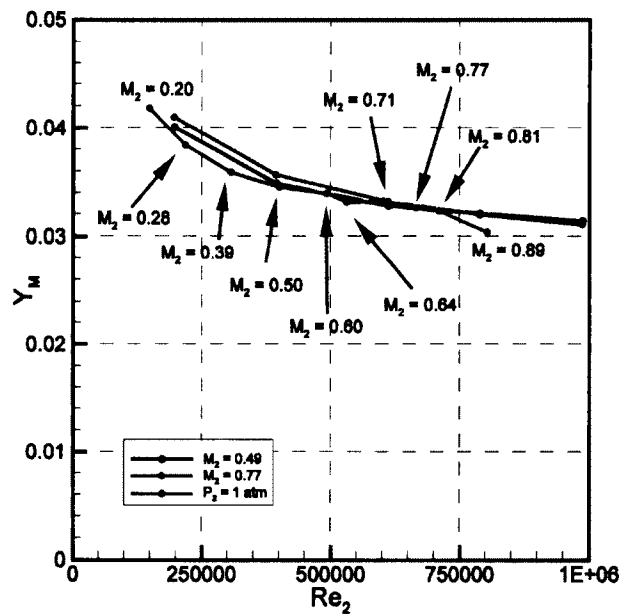


Figure 5.36 Total Pressure Loss Coefficient at Constant Mach Numbers of 0.49 and 0.77 Compared to the Simulations Approximating Wind Tunnel Conditions

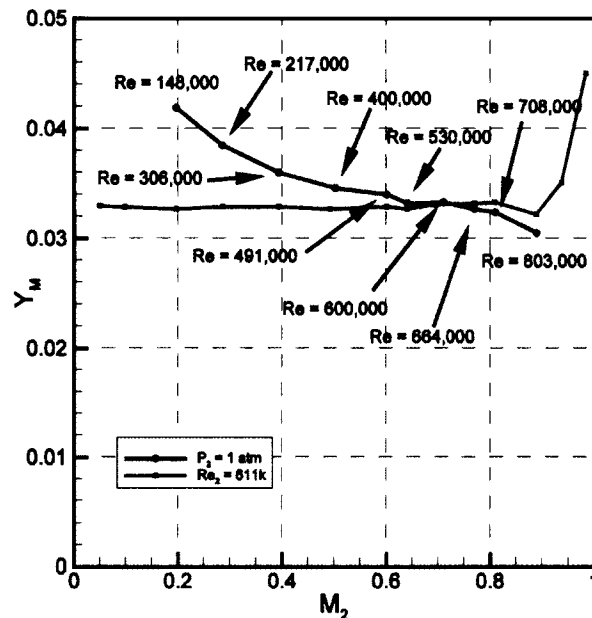


Figure 5.37 Total Pressure Loss Coefficient at a Constant Reynolds Number of 611,000 Compared to the Simulations Approximating Wind Tunnel Conditions

5.6.5 Flow Angles

As discussed in Sections 5.4.5 and 5.5.5, the exit flow angle is dependent on the exit Mach number, and is independent of Reynolds number effects. This is clearly seen in Figure 5.38 which compares the exit flow angle for the simulations which varied the Mach number independent of Reynolds number, and the simulations which approximated the wind tunnel conditions. The two sets of simulations show essentially identical results for the exit flow angle.

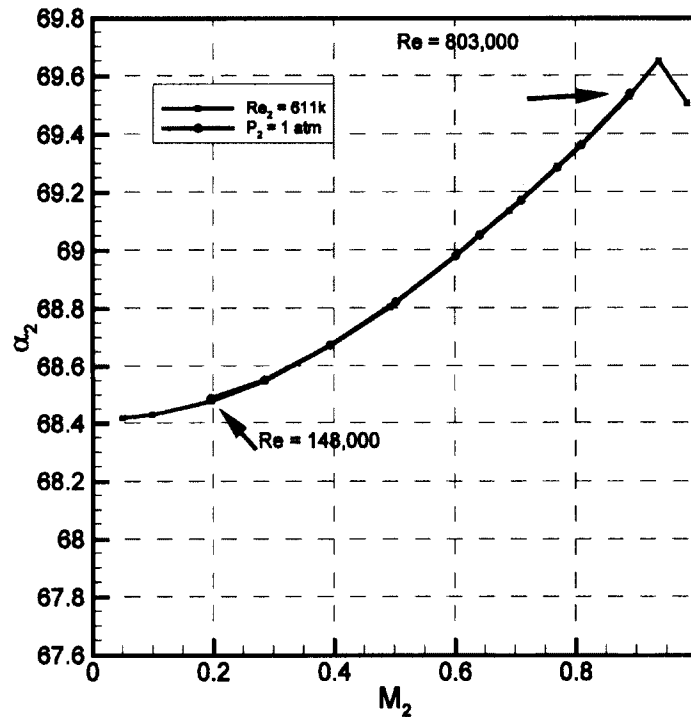


Figure 5.38 Exit Flow Angle at a Constant Reynolds Number of 611,000 Compared to the Simulations which Approximated Wind Tunnel Conditions

5.6.6 Wake Profiles

As seen in Figure 5.39, the depth of the wake profiles for the cases approximating the wind tunnel conditions are very similar to the wake profiles for the cases with a fixed Mach number of 0.77. This corresponds to the increased losses discussed in the previous section. The primary difference between the two sets is the location of the centre of the wake. As the Mach number increases in the cases approximating the wind tunnel, the wake shifts towards the pressure side.

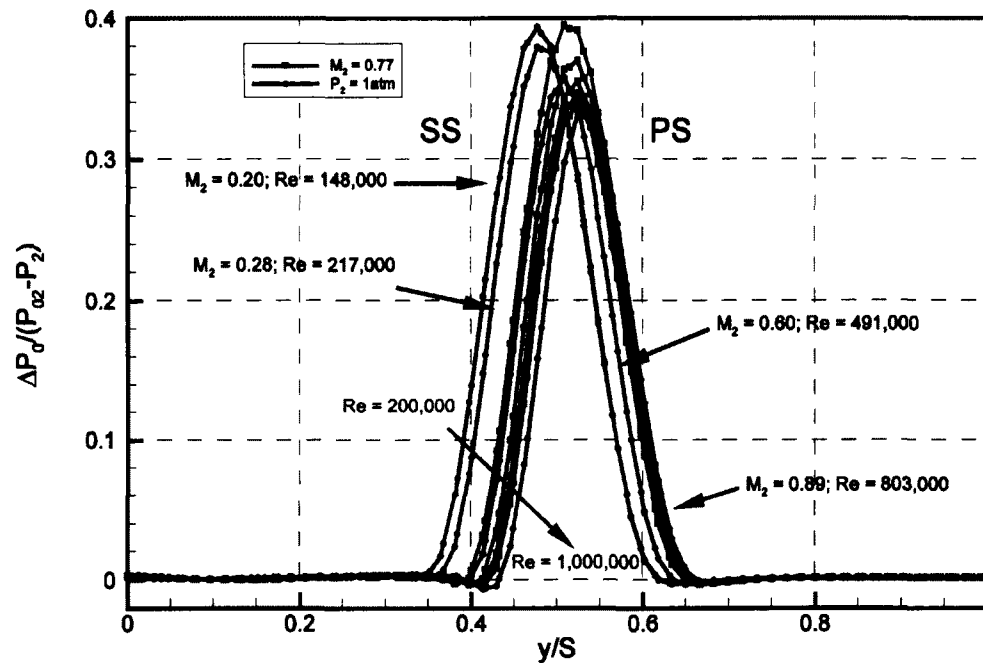


Figure 5.39 Wake Profiles at $1.4 C_x$ at a Constant Mach Number of 0.77 Compared to the Simulations Approximating Wind Tunnel Conditions

5.7 Conclusions

CFD simulations were run for four sets of cases: a fixed Reynolds number, two fixed Mach numbers, and a set which varies the Mach number while the Reynolds number corresponds to a fixed exit pressure. The blade loadings were found to be strongly affected by the Mach number, while the Reynolds number only slightly influenced the blade loadings by affecting the transition location. The exit flow angles determined by the simulations increased with the blade loadings resulting from changes in the Mach number. While the Mach number affected the

exit flow angle by 1.2 degrees as the Mach number increased from 0.05 to 0.94, the Reynolds number influence on exit flow angle was negligible.

Some of the blade loadings, especially at high Mach numbers, showed evidence suggestive of flow separation in the form of a plateau in pressure followed by a sudden decrease in pressure. However, only the cases above a Mach number of about 0.89 showed actual reversed flow; all the other cases remained attached. Because these cases were in the process of separating before transitioning to turbulent flow, the displacement thickness and shape factor each exhibited a peak before the transition location. This peak in the displacement thickness has the same effect on the inviscid flow as a small separation bubble, thus resulting in a pressure distribution suggesting flow separation.

The total pressure loss coefficient was used to assess the influence of both the Mach number and the Reynolds number on the losses. The Mach number had a negligible effect on the total pressure loss coefficient below a value of 0.89. Above $M_2 = 0.89$, losses due to shock waves appeared, raising the total pressure loss coefficient rapidly with Mach number. In the absence of shock losses, the Reynolds number had a stronger influence on the total pressure loss coefficient than the Mach number. An increase in the Reynolds number resulted in a decrease in the total pressure loss coefficient. The total pressure loss coefficient was increased further for the cases which were nearly separated.

The simulations which approximated the wind tunnel conditions indicated that the blade loading and exit flow angle in the wind tunnel will be essentially

independent of Reynolds number effects for the Reynolds number range examined. The combined effects of Mach number and Reynolds number in the wind tunnel are predicted to have opposing effects on the transition location. At Mach numbers below 0.5, the result is that the transition location is predicted to stay roughly constant. Above $M_2 = 0.5$, the transition location is predicted to move towards the trailing edge of the blade. The Mach number effect on the total pressure loss coefficient in the wind tunnel is predicted to be very small relative to the changes due to Reynolds number, suggesting the wind tunnel results for total pressure loss coefficient will be more representative of the Reynolds number effects than the Mach number effects prior to the onset of shocks in the flow.

Chapter 6

Experimental Performance Results of the SL2 Cascade

6.1 Introduction

This study is concerned with the influence of outlet Mach number on the total pressure losses through a turbine cascade. Common practice is to correct the influence of compressibility by a factor which relates the total pressure loss coefficient in the compressible range to the value at the incompressible limit as suggested by Dunham and Came (1970). Because the wind tunnel capabilities were extended to low Mach numbers as outlined in Chapter 4, it is possible to take measurements below the incompressible limit. Measurements were made for ten Mach numbers between 0.2 and 1.0.

Because the wind tunnel discharges to atmosphere, Mach number is varied by changing the blowing pressure. However, this also has the effect of changing the Reynolds number. Chapter 5 was concerned with determining the influence of Reynolds number on the results numerically. This included cases where the Mach

number was varied while the Reynolds number corresponded to a constant exit pressure, as this was intended to approximate the behaviour of the wind tunnel. In reality, the exit pressure will be reduced at higher Mach numbers due to the diffuser that exhausts the flow from the test section. Thus additional CFD simulations have been run to closely match the experimental results, as shown in Figure 6.1. These two sets of results will be compared throughout this chapter. This comparison will be used both to validate the computations and to extend the understanding of the experimental data. Additionally, the data for this cascade from Taremi et al. (2010) will also be included to indicate the repeatability of the experimental results.

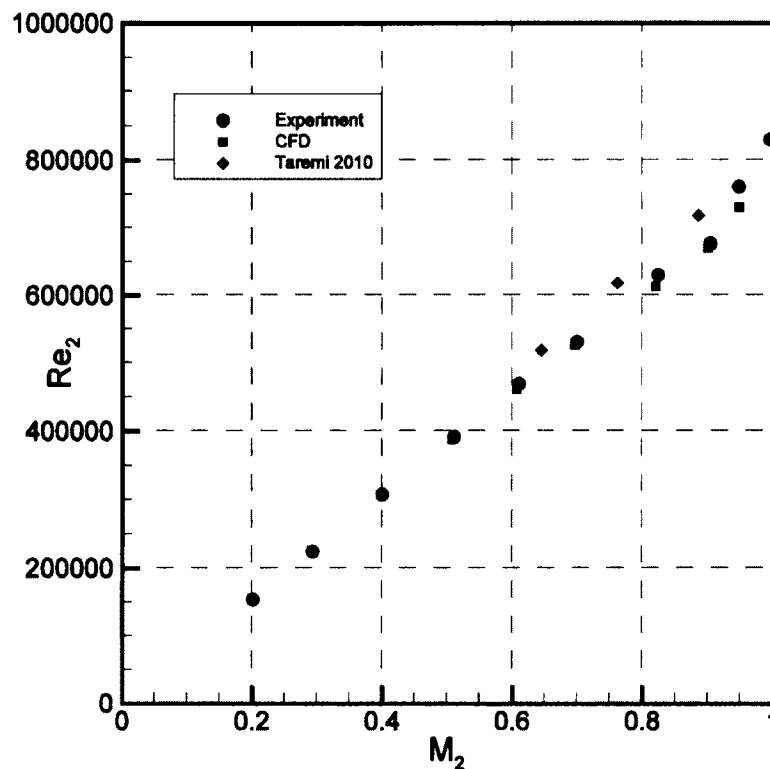


Figure 6.1 Experimental Test Cases Compared to CFD Test Cases Simulating Wind Tunnel Conditions

6.2 Flow Quality

6.2.1 Introduction

When running any experiment, it is important to check the flow quality to ensure confidence in the results. In particular, tests are performed on the upstream uniformity, downstream periodicity, and, for two-dimensional flow studies such as this one, the axial-velocity-density ratio (AVDR). Jeffries (2000) compared the results of the Carleton high speed wind tunnel to the results from four other high speed wind tunnels to ensure that quality measurements are possible with the apparatus. However, several additional tests are necessary every time a cascade is installed in the wind tunnel to ensure the quality of the results.

6.2.2 Exit Flow Angles and Exit Flow Angle Correction

The probe stem shifted slightly during the runs and required a small correction. This shift occurred because the sharp edge of the probe stem cut into the Teflon support shown in Figure 6.2 each run. Because CFD typically produces reliable results for the trend in exit flow angle, the CFD results were used to guide the flow angle correction. In comparing the uncorrected experimental results to the CFD results, the difference between the two was found to increase by an average 0.2° per run of the wind tunnel. This is consistent with the wake measurements: the flow angle on either side of the wake had an average difference of 0.2° . Rather than correct the experimental results to match perfectly the trend of the CFD, this

average of 0.2° was used for the correction. Figure 6.3 shows the exit flow angle variation with Mach number after applying this correction, the CFD results which were used to develop the correction, and the exit flow angles determined by Taremi et al. (2010). The results from Taremi et al. (2010) show a similar trend, further supporting this correction.

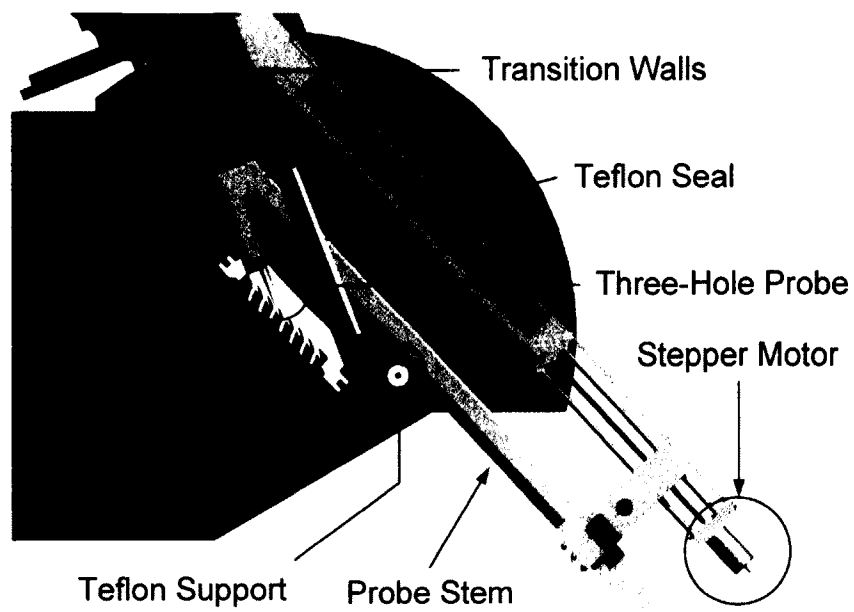


Figure 6.2 Location of Teflon Support

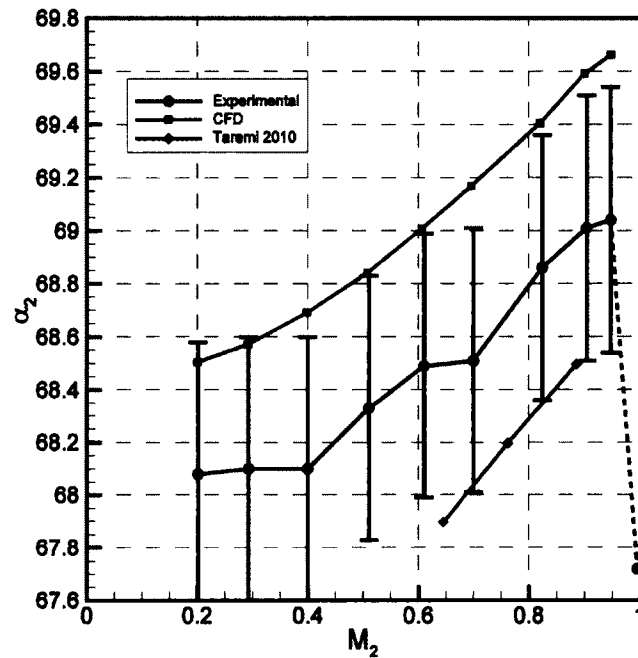


Figure 6.3 Exit Flow Angle Variation with Exit Mach Number for Experiment Compared to CFD with Reynolds Number Corresponding to Constant Exit Pressure

In addition to the exit flow angle, the shifting of the probe stem also affected the wake data. As the probe stem shifted, the apparent centre of the wake also shifted. To correct for this shift, the centre of the wake – taken as the location of minimum total pressure – was determined for the measurement plane based on the measured exit flow angle and a reference case. Because the interest is in the movement of the wake from case to case, the selection of the reference case is unimportant and arbitrary. The location of the centre of the wake with respect to the reference case, illustrated in Figure 6.4, is determined from

$$\frac{y}{s} = \frac{y_{ref}}{s} + \left(\frac{x}{C_x}\right) \left(\frac{C_x}{s}\right) (TAN\alpha - TAN\alpha_{ref}) \quad 6.1$$

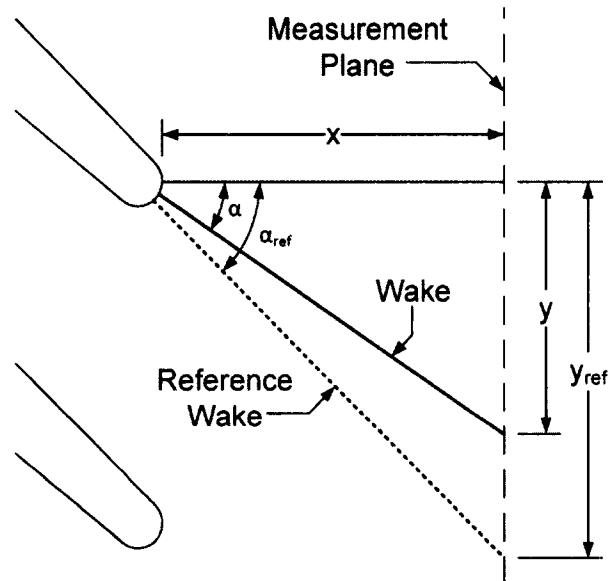


Figure 6.4 Illustration of Wake Centre Correction

6.2.3 Upstream Uniformity

Leakage flows from the test section or improper alignment of the test section side walls can affect the upstream uniformity, as well as the overall quality of the results. To assess the upstream uniformity, upstream static pressure measurements were taken with a row of static pressure taps distributed evenly across the full width of the cascade at 1.4 axial chord lengths upstream of the leading edge. Figure 6.5 shows the inlet Mach numbers measured at the wall. There is no significant variation in the results, indicating that upstream static pressures at the wall do not vary during the run in the pitchwise direction.

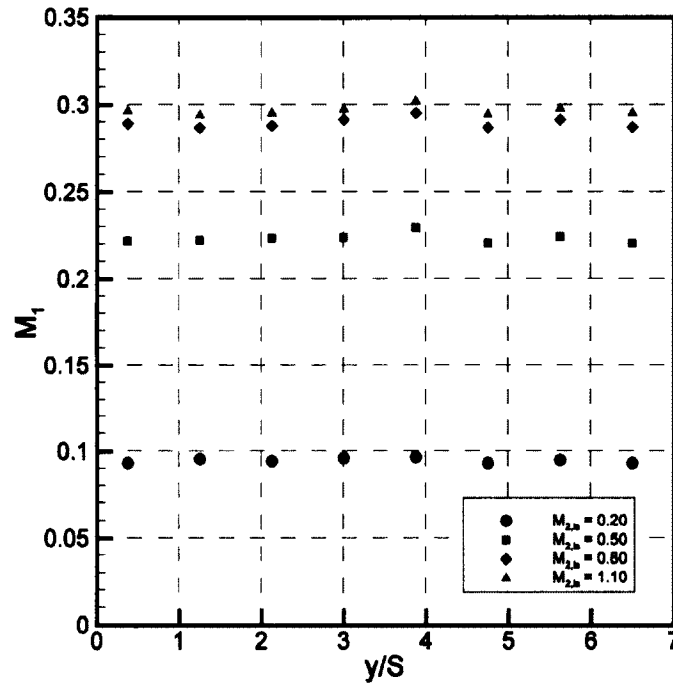


Figure 6.5 Results of Upstream Uniformity Check

6.2.1 Axial-Velocity-Density Ratio

The Axial-Velocity-Density Ratio (AVDR) is a measure of the streamtube expansion or contraction across the blade row and is defined as

$$AVDR = \frac{\int_0^1 \rho_2 V_2 \cos \alpha_2 d\left(\frac{y}{S}\right)}{\int_0^1 \rho_1 V_1 \cos \alpha_1 d\left(\frac{y}{S}\right)} \quad 6.2$$

In a two-dimensional flow the AVDR is equal to 1.0 since the flow is neither expanding nor contracting in the spanwise direction. While the AVDR alone is not sufficient to prove two-dimensional flow, as discussed in Section 2.5.5, it is a useful metric nonetheless. To ensure sufficient quality, generally the AVDR for two-dimensional flow should be within 0.98 and 1.02.

The value of AVDR is generally acceptable as seen in Figure 6.6. For Mach numbers between 0.29 and 0.89, the AVDR from this study is closer to 1.0 than the results from Taremi et al. (2010). At the lowest Mach number of 0.20 the AVDR rises to 1.04. This could be a sign that the flow structures on the endwalls of the cascade have grown sufficiently to interfere with the two-dimensionality of the flow. Likewise, the AVDR rises significantly above Mach 0.9. This is likely related to the development of shock waves in the flow. It is important to note that the three-hole probe used to traverse the wake has only been calibrated to a Mach number of 0.94. Any measurements above this should be treated with some caution. For this reason, the measurement at $M_2 = 1.00$ has been connected to the rest of the data with a dashed line.

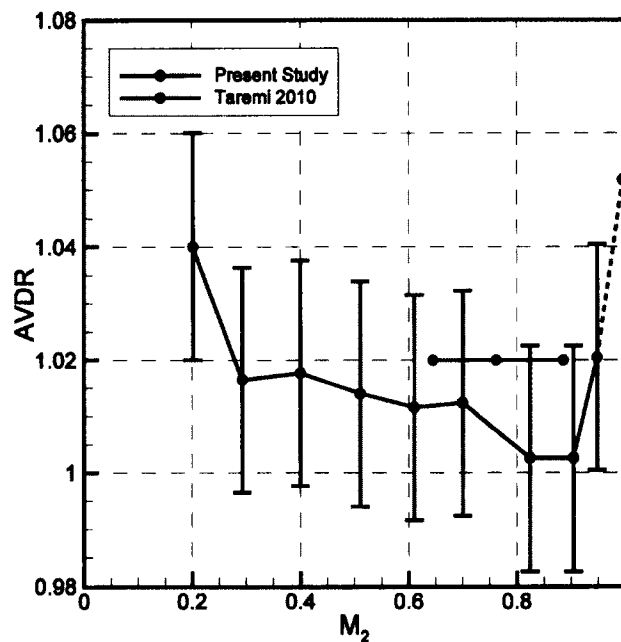


Figure 6.6 Variation of AVDR with Exit Mach Number

6.2.2 Periodicity

One of the goals of cascade testing is to obtain test results relevant to a periodic geometry. As such, it is important to establish that the results are, in fact, periodic. This has been done by simply comparing the results of several adjacent blades. Figure 6.7 shows the mixed-out total pressure loss coefficient for five blades at an isentropic exit Mach number of 0.20 and 0.80. At $M_{2,is} = 0.8$, the total pressure loss coefficient is within ± 0.0015 for all five blades. However, the fifth blade has a higher mixed-out exit Mach number, indicating the flow over the fifth blade is not periodic at this Mach number. At $M_{2,is} = 0.2$, the total pressure loss coefficient varies by ± 0.00512 . The increased variation in total pressure loss coefficient at this low Mach number can be attributed to the increased uncertainty of the results, as outlined in Section 4.6.3, rather than a loss of periodicity at low Mach numbers. Figure 6.8 shows the AVDR and exit flow angle at an isentropic exit Mach number of 0.20 and 0.80. These results demonstrate that while the flow over the first four blades is similar, the flow over the fifth blade is clearly not periodic.

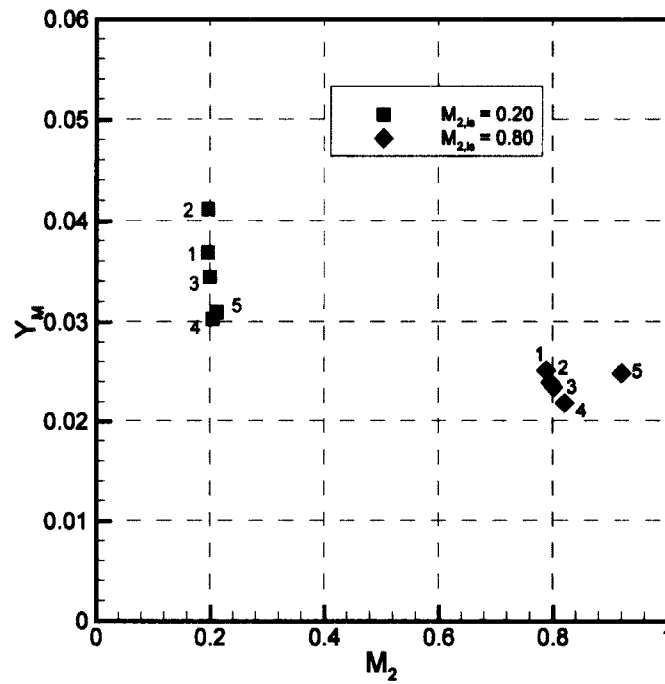


Figure 6.7 Results of Periodicity Check: Total Pressure Loss Coefficient

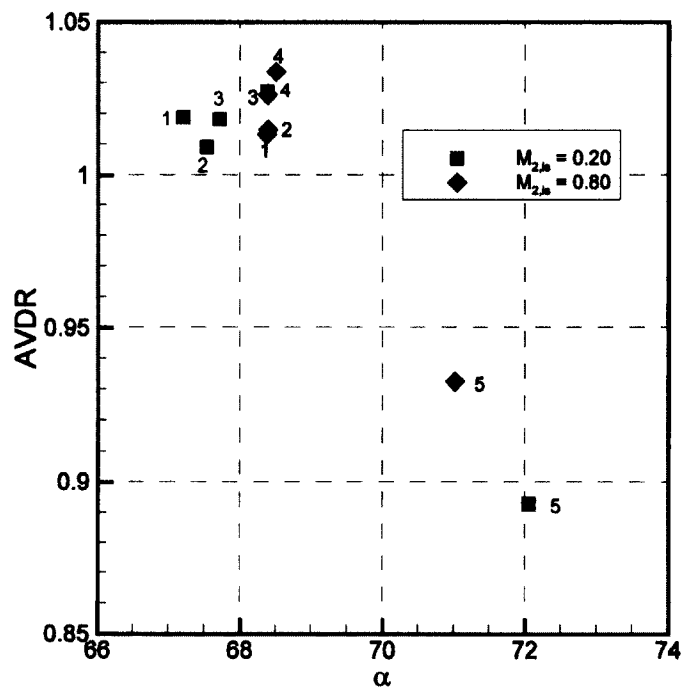


Figure 6.8 Results of Periodicity Check: Axial-Velocity-Density Ratio and Exit Flow Angle

6.3 Blade Loadings

Figure 6.9 shows the blade loadings measured at several Mach numbers. These results are compared to the CFD results for the corresponding Mach numbers. The results match the CFD very well on the suction side for all Mach numbers. While the pressure side results do not match as well, they are consistent with a mismatch in the incidence angles between the experiment and the CFD. Additionally, the Mach number calculation for the measurements is especially sensitive to error at low Mach numbers, as outlined in Section 4.6.2. Section 5.4.3 related features seen in the computed blade loadings to the flow nearly separating before undergoing transition on the suction side. While the experimental blade loadings match the CFD results closely, boundary layer traverses would be necessary to be confirm whether or not the flow undergoes transition before separation can occur.

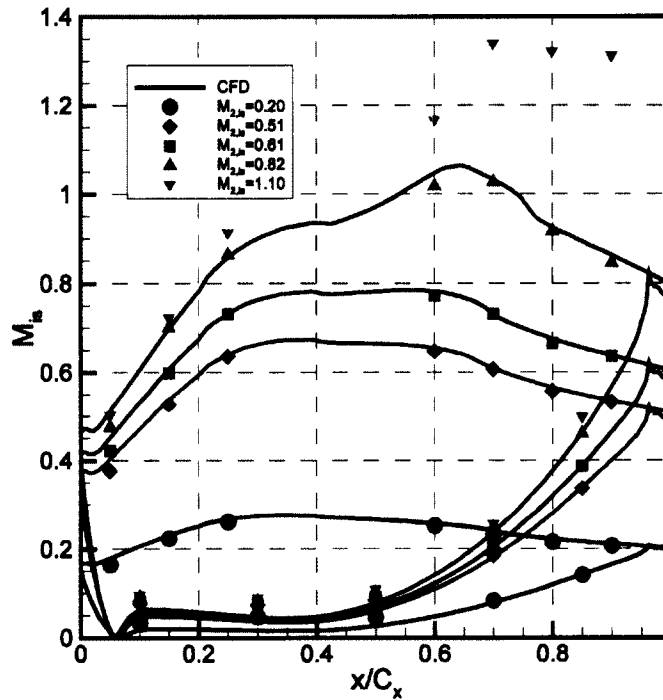


Figure 6.9 Blade Loadings for Experiment Compared to CFD for Several Mach Numbers

6.4 Losses

Figure 6.10 shows the total pressure loss coefficients determined for SL2 experimentally along the results from Taremi et al. (2010) for the same cascade and the CFD results for the Reynolds number corresponding to constant exit pressure. The total pressure loss coefficient drops as the Mach number rises from 0.2 to 0.6. Above a Mach number of 0.6, the total pressure loss coefficient remains mostly constant up to $M_2 = 0.89$ after which it rises sharply. In Chapter 5 it was suggested that the total pressure loss coefficient was mostly a function of Reynolds number, and that compressibility effects were mostly seen above a Mach number of 0.89.

The similarity of the trends for experiment and CFD support this conclusion. The differences between the measured and computed losses are discussed further in Section 7.3. The total pressure loss coefficient rises substantially above a Mach number of 0.89, as shock waves start to appear in the flow.

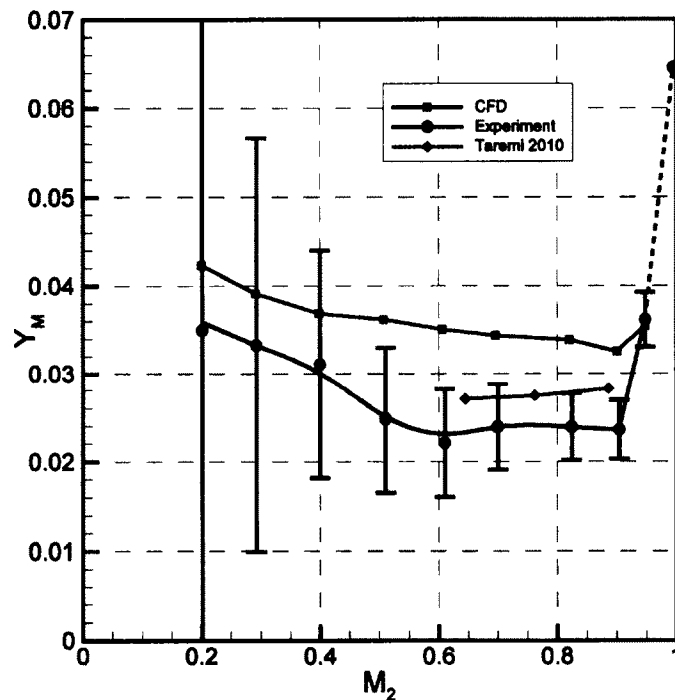


Figure 6.10 Total Pressure Loss Coefficient Variation with Exit Mach Number for Experiment Compared to CFD Simulating Wind Tunnel Conditions

6.5 Wake Profiles

Figure 6.11 shows selected experimental wake profiles. As the Mach number increases, the exit flow angle increases, which results in the wakes shifting towards the pressure side. For the highest Mach number, portions of the flow become supersonic. The extra pressure loss at the highest Mach number near the pressure

side of the wake is the result of the losses generated through a shock wave. Figure 6.12 compares the measured wakes to the wakes extracted from the corresponding CFD at selected Mach numbers. It should be noted that the centres of the wakes have been aligned relative to the design Mach number based on Equation 6.1. The movement of the wake with increasing Mach number has been indicated by connecting the peak value of each wake. The centres of the wakes for the experiment match quite well with the CFD. The experimental wakes are narrower than those in the CFD. This is consistent with the fact that the CFD predicted higher losses than the experiment. At low Mach numbers, the experimental wakes are deeper than the computed wakes, while at higher Mach numbers the experimental and computed wakes have similar depths.

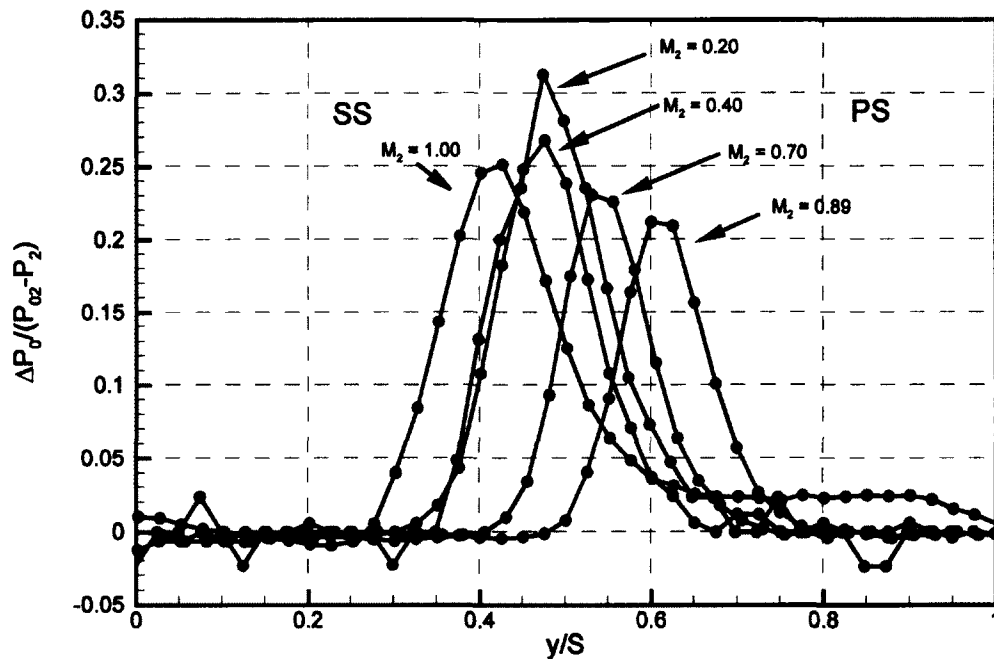


Figure 6.11 Selected Experimental Wake Profiles

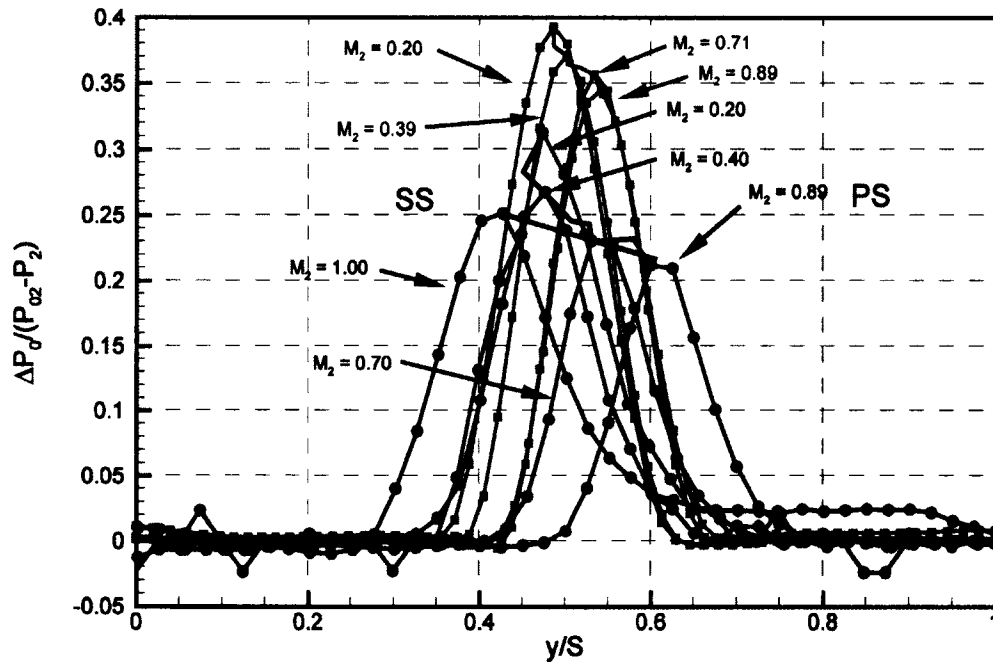


Figure 6.12 Comparison of Selected Experimental and CFD Wake Profiles

6.6 Conclusions

Linear cascade tests were performed for the SL2 cascade at ten Mach numbers between 0.20 and 1.00. To ensure the flow quality of the experiments, tests were performed on the upstream uniformity, downstream periodicity and AVDR. These tests revealed that the probe stem shifted during the experiment, and an appropriate correction was developed for the data. The results of these tests are compared to the simulations from Chapter 5 with Reynolds numbers corresponding to a constant exit pressure.

The blade loading measurements are a close match to the computed blade loadings and the differences can be explained by a mismatch in the incidence angle

between the experiment and the CFD. However, the resolution of the experimental data is not sufficient to support or reject the conclusions drawn from the computed blade loadings regarding the effects of transition on the blade loading.

The measurements of the total pressure loss coefficient show a drop in total pressure loss coefficient as the Mach number is raised from 0.2 to 0.6. Based on the CFD results, this drop is attributed to Reynolds number effects. Between $M_2 = 0.6$ and 0.89, the total pressure loss coefficient remains essentially constant, above which point the losses rise rapidly. This rapid rise in losses can be attributed to the supersonic drag rise associated with the formation of shock waves within the passage.

Investigation of the wake profiles showed that the motion of the wakes with increasing Mach number determined experimentally show good agreement with the computed wakes. Additionally, the experimental wakes are narrower than the wakes from CFD, which is consistent with the fact that the CFD predicted higher losses than the experiment.

Chapter 7

Development of Correction Factors for the Effects of Reynolds Number and Mach Number on Profile Losses

7.1 Introduction

The motivation of this study is to evaluate and improve, if possible, the subsonic Mach number correction of Kacker and Okapuu (1982). Chapters 5 and 6 evaluated the performance of the SL2 cascade for a range of operating conditions defined by both Mach number and Reynolds number. It is useful to establish to what extent the performance of the SL2 cascade compares with the performance of other well-designed blade geometries to determine whether the results are geometry-specific. This chapter compares the numerical and experimental results for total pressure loss from Chapters 5 and 6 to the performance of several cascades described in the open literature. These cumulative results are then used to develop tentative improvements to both the Reynolds number and compressibility

corrections in the Kacker and Okapuu loss system. However, these tentative improvements rely on the CFD for the SL2 cascade to isolate the Reynolds number effects from the compressibility effects, and thus may require further modification before they can be used for general prediction of Mach number and Reynolds number effects on profile losses. Finally, the results for all available cases are compared to the Kacker and Okapuu loss correlation.

7.2 Correction Factors for Design Point Selection Compared to Off-Design

When working with correction factors to predict the effects of Mach number and Reynolds number, it is useful to distinguish between two types of correction factors. These two types will be referred to as design corrections, and off-design corrections.

Design corrections are intended to take the loss predictions at some reference condition (e.g. incompressible), and project what the losses will be at the design condition for an airfoil with the same basic geometric parameters. The corrections in the Kacker and Okapuu loss prediction system are all design corrections. Because the Kacker and Okapuu system is based on data which were collected at incompressible conditions with Reynolds numbers around 200,000, design corrections are needed to make loss predictions for airfoils which were designed to operate at other Mach numbers or Reynolds numbers.

When developing a design correction, each cascade should ideally only be evaluated at its design point. However this requires data from a set of cascades with a wide range of geometries and design Reynolds numbers and Mach numbers which is not available. The limited data can be supplemented by the use of CFD or by including off-design data for conditions where the cascade performed similarly to a cascade optimised for those other conditions. While using off-design data in the development of a design correction is not ideal, the losses generated by a blade at an off-design operating point will generally be higher than the losses generated by a blade that is optimised for that operating point. Therefore the off-design data can be considered to give an upper estimate for the possible values of a well designed blade. Design corrections benefit from the fact that they only attempt to predict the losses for a well designed airfoil, and thus they will tend to rely on fewer variables. It is worth noting that the design point will not necessarily be the operating point which produces minimum loss for that airfoil. For example, the design may have been optimised to produce good performance over a range of conditions, at the expense of optimum performance at the design point.

Off-design corrections are corrections which predict the additional losses generated when operating the same airfoil at a different conditions from the design conditions. Off-design corrections account for the additional losses both due to changing operating condition and due to the fact that the airfoil is not optimised for the new operating condition. Off-design corrections benefit from the fact that they can make use of any cascade data, although they will require additional parameters

to account for additional sources of losses. Since most data obtained in cascade experiments are for the same geometry operated at a range of conditions, such data are most suited for developing off-design corrections.

The motivation of this chapter is to evaluate and improve, if possible, the Kacker and Okapuu subsonic Mach number loss correction. The Kacker and Okapuu loss system predicts the losses at the design point of a cascade. As such, any improvements to the correction factors will be design corrections.

In Chapter 5 it was determined that the Reynolds number effects are of a similar magnitude to the Mach number effects. To address this, Section 7.5 develops a tentative Reynolds number correction from the CFD data for the SL2 cascade. This correction is intended to be used as a design correction, although it is developed from off-design data.

Section 7.6 evaluates the subsonic design correction for Mach number. Due to the limited design point data, this evaluation is done with mostly off-design data, provided the losses were representative of design point losses as discussed in Section 7.4.

7.3 Comparison of Numerical and Experimental Losses from the Present Study

For this study, CFD simulations were performed to match the combinations of Mach numbers and Reynolds numbers obtained in the experiment, as illustrated

in Figure 7.1. As seen in Figure 7.2, there is good agreement for the trend in total pressure loss coefficient with Mach number between the experiment and the simulations, although there are significant differences in magnitudes. Below a Mach number of about 0.5, the calculated loss coefficients are about 1.2 times the measured loss coefficients. Above $M_2 = 0.5$, the calculated loss coefficients are about 1.4 times the measured loss coefficients. There are a number of differences between the numerical modelling and the experiment which may explain the differing loss coefficients, including the transition model used in the CFD and the fact that the simulations treat the flow as steady-state while the experimental results are time-averaged values of a flow that may have some time variation.

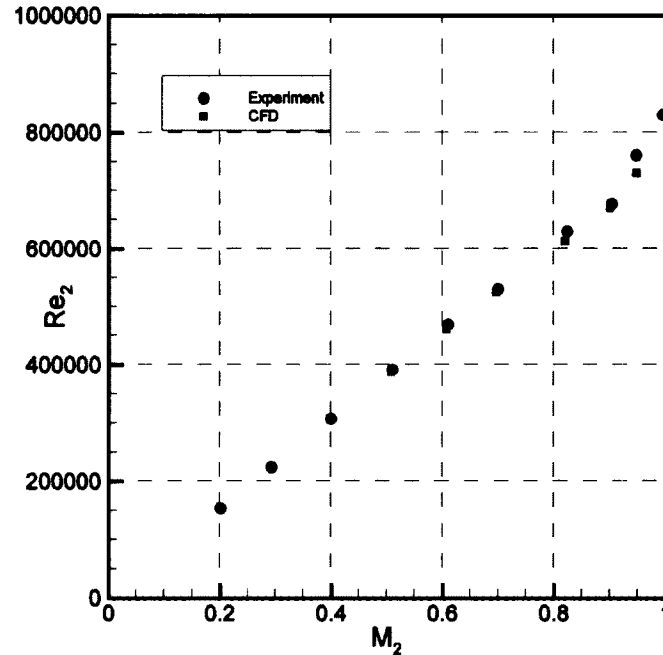


Figure 7.1 Experimental Test Cases Compared to CFD Test Cases which Simulated Wind Tunnel Conditions

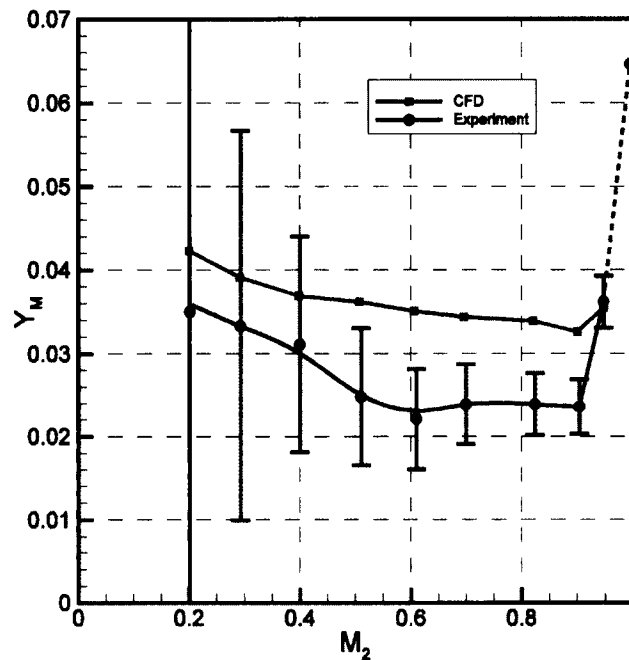


Figure 7.2 Total Pressure Loss Coefficient for Experiment Compared to CFD which Simulated Wind Tunnel Conditions

The transition model used in the numerical studies has been validated for a wide range of conditions by Langtry et al. (2004). However, the transition model has not been modified to account for the effects of compressibility (Menter et al. 2006), which may have some effect on the results in this study.

For this study, possible vortex shedding at the trailing edge of the blades is expected to be the most significant unsteady flow feature. If vortex shedding is present, the base pressure is expected to be reduced (Kurosaka et al. 1987). As explained in Section 2.5.2, a decreased base pressure causes higher mixed-out losses. The effect of base pressure on losses is greater for blades with larger trailing edge thickness to throat ratios. Since the SL2 cascade has a trailing edge thickness

to throat ratio of about 0.0867, the effect of base pressure is expected to be small. The fact that the experiment measures time-averaged values means that the results will be affected by any unsteady flow features, whereas the CFD results will not account for these effects as the simulations were run for steady-state conditions to keep the simulation times manageable.

7.4 Sources of Data from the Literature

The results presented thus far are all specific to the SL2 cascade. Data from other cascades must be used in order to establish the effect of geometry on the results. For this reason, data from the open literature were also considered. The majority of the cases were in fact obtained at Carleton University. There are relatively few transonic turbine results available in the open literature from other research groups.

The studies summarised in Table 7.1 include loss data for compressible cascade tests at both subsonic and supersonic outlet Mach numbers but only the subsonic results are used here. Note that the loss data for the OX cascade (Mee et al. 1992) was presented as a kinetic energy loss coefficient, $\Delta\phi^2$, normalised by the kinetic energy loss coefficient at the design point. This normalisation was removed by estimating a reference kinetic energy loss coefficient of 0.035. This value is based on the kinetic energy loss values of the HS1A, HS1C, and HS1D cascades (Corriveau 2005), and is thus only approximate. As a result, the loss data for the OX

cascade will only be used to evaluate the trends in the losses, since the trends will be unaffected by the selected reference kinetic energy loss coefficient.

Table 7.1 Summary of Data Sources from Literature

Source	Cascade Designation	Constant Reynolds Number	Constant Mach Number	Range Studied
Corriveau 2005	HS1A, HS1C, HS1D	No	No	$0.5 < M_2 < 1.3$ $470,000 < Re_2 < 1,200,000$
Corriveau 2005	HS1A, HS1C, HS1D	No	Yes	$M_2 = 0.6, 0.85, 0.95, 1.05$ $320,000 < Re_2 < 1,300,000$
Jouini 2000	HS1A, HS1B	No	No	$0.55 < M_2 < 1.2$ $500,000 \leq Re_2 < 1,100,000$
Jeffries 2000 (Includes Kiock et al. 1986)	HS2	No	No	$0.29 < M_2 < 1.3$ $330,000 < Re_2 < 1,200,000$
Taremi et al. 2010	SL1, SL2, SL3, SL4	No	No	$0.63 < M_2 < 0.9$ $490,000 < Re_2 < 720,000$
Mee et al. 1992	OX	No	Yes	$M_2 = 0.92$ $500,000 < Re_2 < 2,000,000$
Mee et al. 1992	OX	Yes	No	$0.57 < M_2 < 1.2$ $Re_2 = 1,000,000 \text{ \& } 2,000,000$
Perdichizzi 1990	CNPM	No	No	$0.18 < M_2 < 1.6$ $160,000 < Re_2 < 1,700,000$

Since the design correction for Mach number is concerned with the losses generated at the design point Mach number of the cascade, each cascade geometry should strictly be used for only the design point Mach number. However, this requires data from a large number of cascade geometries, which are not available. Instead, data collected over the full range of subsonic Mach numbers, design and off-design, are used provided the flow did not separate and the axial-velocity-density

ratio (AVDR) was between 0.96 and 1.04. The data from the HS2 cascade (Jeffries 2000) were largely below the lower limit for AVDR, but since data for HS2 were collected in five different wind tunnels including the one at Carleton, they are still included to provide insights into the influence of “wind tunnel effects”. However, the data from only three of these European wind tunnels will be considered because of some concerns raised by Kiock et al. (1986) about the quality of the data from the fourth European facility. The data from the HS1B cascade (Jouini 2000) was above the upper limit for AVDR and will not be presented. Further, the scope of this study is concerned with the subsonic compressibility correction only. Thus the supersonic data points are omitted. Finally, the author’s judgement has been used to reject any data where the losses rise excessively when the operating point differs significantly from the design point. Specifically, several data points from the HS1A, HS1C, and HS1D cascades (Corriveau 2005) at low Reynolds numbers were considered to be too far off-design to be useful for the evaluation of a design correction factor.

7.5 Reynolds Number Correction

7.5.1 Introduction

While the motivation and main focus of this study is to evaluate and improve, if possible, the subsonic Mach number correction of Kacker and Okapuu (1982), the results of Chapter 5 have shown that the Reynolds number effects on the total pressure loss coefficients are of a similar or greater magnitude to the subsonic Mach

number effects. This can be seen in Figure 7.3 which compares the results of the simulations for the SL2 geometry which varied the Mach number at a fixed Reynolds number of 600,000 and simulations in which the Mach number and Reynolds number varied as in the experiment.

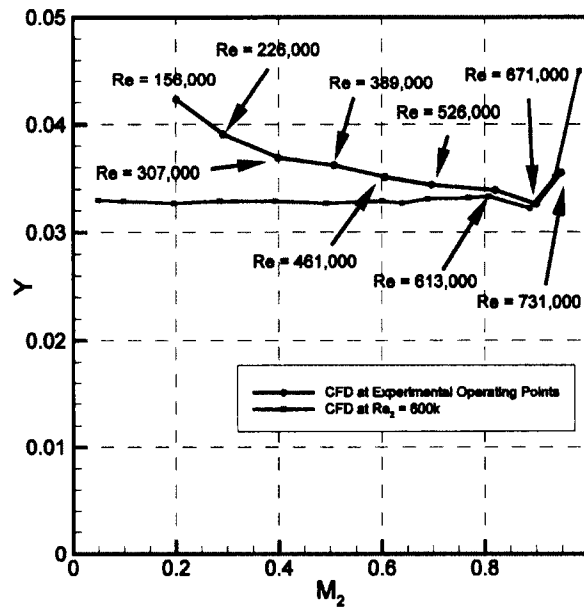


Figure 7.3 Comparison of Loss Prediction for SL2 CFD Test Cases Which Simulated Wind Tunnel Conditions and at Constant Reynolds Number of 600,000

The SL2 CFD simulations performed at constant Mach number will be used in an attempt to remove the Reynolds number effects from the experimental results. This is done by first reviewing the Kacker and Okapuu correction for Reynolds number effects to develop a possible equation that may be more effective at correcting the Reynolds number effects. This equation is then applied to the simulations. The suggested improvements are thus based on the SL2 results only and rely on the CFD simulations to separate the Reynolds number effects from the

Mach number effects. Consequently the proposed improvements are tentative and will likely require further modification as more data becomes available or similar simulations are applied for other cascade geometries.

7.5.2 Development of New Reynolds Number Correction

Formula

As outlined in Chapter 2, the Reynolds number correction to profile losses in the Kacker and Okapuu loss system is applied as follows

$$Y_{P,KO} = 0.914 \left(\frac{2}{3} Y_{P,AMDC} K_P + Y_{SHOCK} \right) f(Re) \quad 7.1$$

where

$$f(Re) = \begin{cases} \left(\frac{Re}{2 \times 10^5} \right)^{-0.4} & , Re \leq 2 \times 10^5 \\ 1 & , 2 \times 10^5 < Re \leq 10^6 \\ \left(\frac{Re}{10^6} \right)^{-0.2} & , Re > 10^6 \end{cases} \quad 7.2$$

Note that in this thesis the Reynolds number is always expressed as $Re = \frac{\rho_2 V_2 C}{\mu}$. This is the form used by Kacker and Okapuu as well. Because nearly all the data being considered has Reynolds numbers between 200,000 and 1,000,000, this is the range investigated here. Zhu and Sjolander (2005) suggested an alternative correction for the low Reynolds number range:

$$f(Re) = \begin{cases} \left(\frac{Re}{2 \times 10^5} \right)^{-0.575} & , Re \leq 2 \times 10^5 \\ 1 & , 2 \times 10^5 < Re \leq 10^6 \\ \left(\frac{Re}{10^6} \right)^{-0.2} & , Re > 10^6 \end{cases} \quad 7.3$$

Both of the above Reynolds number corrections normalise the Reynolds number by some reference value. In the case of the Kacker and Okapuu correlation, which is based on the Ainley and Mathieson system, the reference Reynolds number is 200,000 since this is the Reynolds number at which most of the data from Ainley and Mathieson (1951) was collected. Because the present study uses the SL2 cascade, a more appropriate reference Reynolds number is its design Reynolds number of 600,000. Additionally, the above Reynolds number corrections modify the profile losses through the exponent to which the Reynolds number is raised. For both Equations 7.2 and 7.3 the exponent used below a Reynolds number of 200,000 is smaller (more negative) than the exponent used above $Re = 1,000,000$. While the corrections in the above equations assume no correction is necessary between Reynolds numbers of 200,000 and 1,000,000, the computations for SL2 at least indicate that there are Reynolds number effects in this range. For these reasons, it seems likely that a successful Reynolds number correction for the range of Reynolds numbers between 200,000 and 1,000,000 will be proportional to the Reynolds number raised to some exponent which increases (becomes less negative) as the Reynolds number increases.

Based on the above discussion, the equation which was considered to correct the Reynolds number effects in the SL2 data takes the form

$$f(Re) = \begin{cases} \left(\frac{2 \times 10^5}{Re_{ref}}\right)^a \left(\frac{Re}{2 \times 10^5}\right)^{-0.575} & , Re \leq 2 \times 10^5 \\ \left(\frac{Re}{Re_{ref}}\right)^{a+b} \left(\frac{Re-2 \times 10^5}{10^6-2 \times 10^5}\right) & , 2 \times 10^5 < Re \leq 10^6 \\ \left(\frac{10^6}{Re_{ref}}\right)^{a+b} \left(\frac{Re}{10^6}\right)^{-0.2} & , Re > 10^6 \end{cases} \quad 7.4$$

where a and b are the curve fitting constants. By using a nonlinear least squares optimisation, the values of a and b found to best fit the SL2 data are -0.181 and 0.076 respectively. These values were determined by using the data calculated by the CFD cases in this study which held the Mach number constant and varied the Reynolds number as given in Section 5.5. As mentioned above, the reference Reynolds number for this data was chosen to be $600,000$. The choice of reference Reynolds number will be discussed further in Section 7.5.4. Note that the Reynolds number correction outside of the range of the data has been assumed to follow the trends given in Equation 7.3, and has only been adjusted to ensure that the curve is continuous.

The use of Equation 7.4 prompts the introduction of new terminology. When Equation 7.4 is applied to the loss coefficient measured by the experiment, the result is a value that estimates the loss coefficient at the reference Reynolds number.

$$Y_{corr} = \frac{Y}{f(Re)} \quad 7.5$$

where Y is the total pressure loss coefficient determined by the experiment or simulation

Unlike the Kacker and Okapuu correlation, the Reynolds number correction in Equation 7.4 was applied to both the profile loss coefficient and the trailing edge loss coefficient. This is done mostly because the trailing edge losses are expected to be related to the boundary layer integral length scales, which will be related to Reynolds number. The trailing edge losses are still expected to be predicted separately from the profile losses, as done by Kacker and Okapuu, but the Reynolds number correction is now applied to both components.

One particular advantage of Equation 7.4 is that it provides a blend of the Reynolds number corrections for the ranges of Reynolds number below 200,000 and above 1,000,000. This is illustrated in Figure 7.4 which compares Equation 7.4 to Equations 7.2 and 7.3. Equations 7.2 and 7.3 have sharp slope discontinuities at $Re = 200,000$ and $1,000,000$. While Equation 7.4 still has slope discontinuities at these points, they are visibly less sharp, resulting in a curve that appears more physically realistic. Equation 7.4 predicts that the profile losses will decrease by about 22% as the Reynolds number increases from 200,000 to 1,000,000 while Equations 7.2 and 7.3 predict there will be no change in this range. This represents a significant change in predicted losses, and a more realistic behaviour than the constancy indicated by the earlier correction formulae.

Figure 7.5 compares the Reynolds number correction to the losses determined by the CFD simulation which held the Mach number constant and varied the Reynolds number between $Re = 200,000$ and $1,000,000$. Since these are the data used to derive the correction formula, it is unsurprising that they match Equation

7.4 well. However, Figure 7.5 indicates that the CFD gave slightly different results at each Mach number. This suggests that the Reynolds number effects are not entirely independent of Mach number.

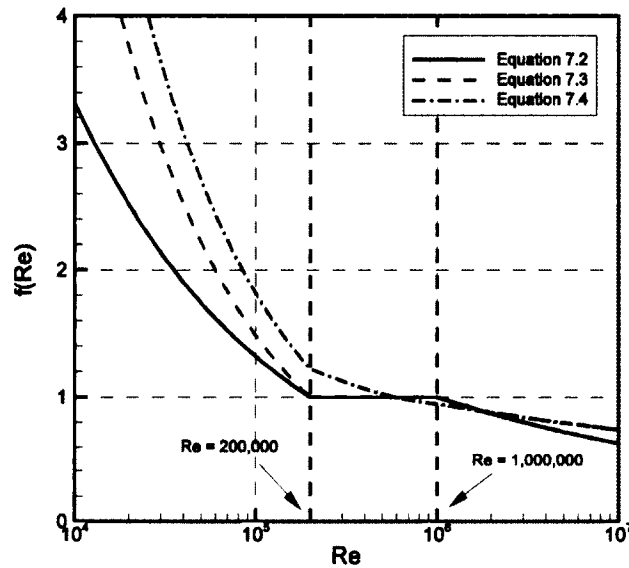


Figure 7.4 Tentative New Reynolds Number Profile Loss Correction Compared to Existing Corrections in Common Use

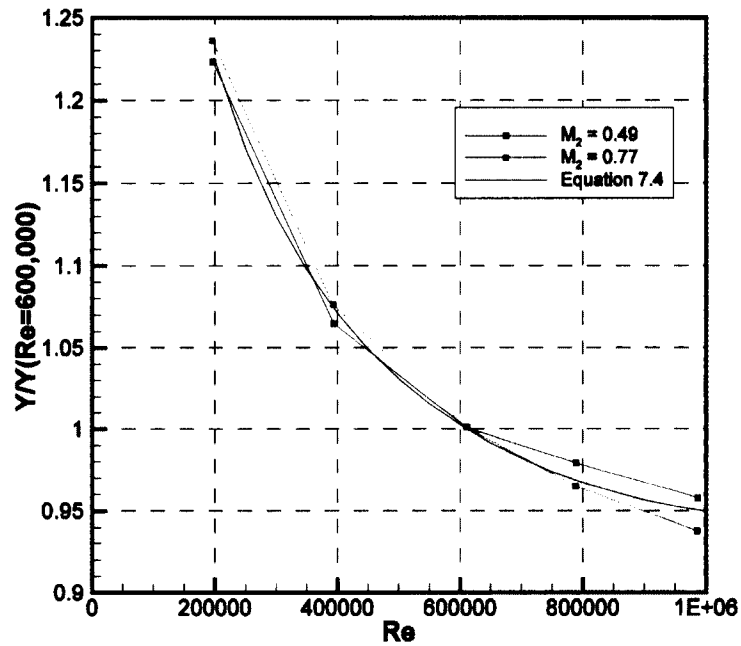


Figure 7.5 Reynolds Number Correction Compared to CFD Results for SL2 with Constant Mach Numbers of 0.49 and 0.77

Figure 7.6 compares the losses calculated by the simulations at constant Reynolds number to the Reynolds number corrected losses from the simulations which reproduced the wind tunnel conditions. Note that neither of these sets of simulations was used to develop the correction formula. With the exception of the data point at Mach 0.2, the Reynolds number corrected total pressure losses from the CFD cases which reproduced the experimental operating points are all within 2% of the value calculated by the simulations performed at constant Reynolds number. The data point at Mach 0.2 for the simulations which matched the wind tunnel conditions has a Reynolds number below 200,000, and thus the Reynolds number correction for this point uses the first part of Equation 7.4.

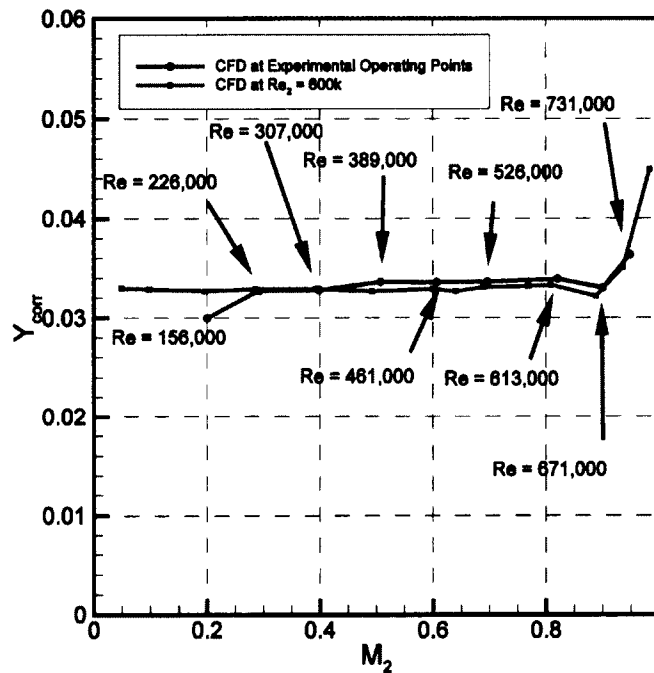


Figure 7.6 Losses Corrected for Reynolds Number Effects for CFD Test Cases Which Simulated Wind Tunnel Conditions and at Constant Reynolds Number of 600,000

7.5.3 Effect of Proposed Reynolds Number Correction

Figure 7.7 compares the experimental results for the SL2 cascade as presented in Chapter 6 both before and after being corrected by Equation 7.4. As described, this correction is based on the CFD. In the absence of experimental data collected at constant Reynolds number, this correction provides the only estimate of the effect of Reynolds number on the losses for this cascade. The Reynolds number correction is most significant for the experimental data at lower Mach numbers where the Reynolds numbers were 200,000 or less. After applying the Reynolds number correction, the total pressure loss coefficient at Mach numbers below 0.4 is nearly constant. Without the Reynolds number correction, the total pressure loss

coefficient rises continuously as the Mach number decreases. This makes it clear that a good estimate of the incompressible value of total pressure loss coefficient cannot be obtained without accounting for Reynolds number effects.

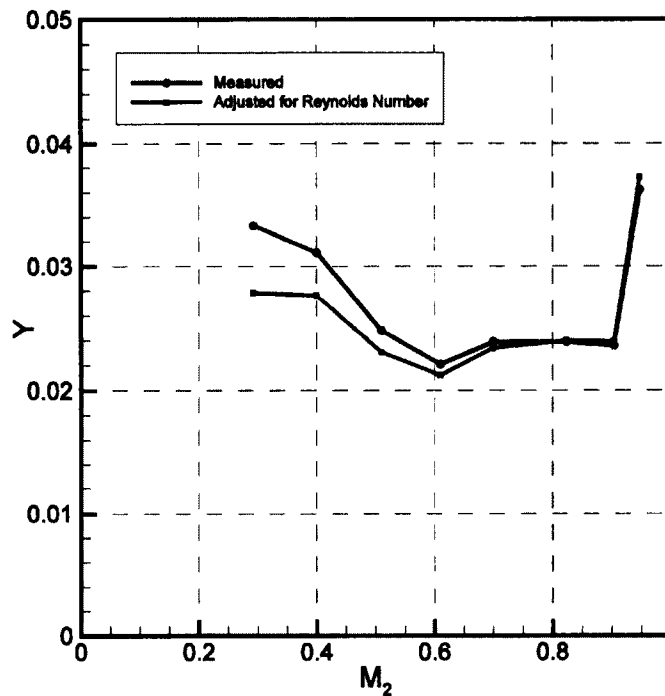


Figure 7.7 Comparison of Total Pressure Loss Coefficient in SL2 Cascade With and Without the Proposed Reynolds Number Correction

7.5.4 Choice of Reference Reynolds Number

The new Reynolds number correction, Equation 7.4, was developed specifically to correct the experimental data for the SL2 cascade to a common reference Reynolds number of $Re_{ref} = 600,000$. However, the broader goal was to devise an improved Reynolds number correction for use in the Kacker & Okapuu loss system. In that system, and the Ainley & Mathieson system that precedes it, the

predicted losses are assumed to apply at $Re_{ref} = 200,000$ since that is the Reynolds number at which most of the underlying cascade data were obtained. The Reynolds number correction is then used to adjust the predicted profile losses to apply at a different desired Reynolds number. To accommodate both of these uses for the new correction, it was formulated in terms of an adjustable Re_{ref} as indicated in Equation 7.4.

The form of Equation 7.4 requires the reference value of the Reynolds number to be between 200,000 and 1,000,000. For the SL2 data, the design Reynolds number was chosen, and in general it may seem that the design Reynolds number would be an appropriate choice. However, this has the disadvantage of normally limiting Equation 7.4 to use as an off-design correction since it would always correct a set of data for a fixed geometry to the value at the design Reynolds number. In the case that the design Reynolds number is unknown or has not yet been selected, values of 200,000 and 1,000,000 are recommended as being appropriate for low pressure and high pressure turbines respectively.

As this study is concerned with the development of a design correction, it is desired to use Equation 7.4 to correct the total pressure loss coefficients at the design point for a range of geometries to the value that would be seen if those cascades had been designed to operate at the reference Reynolds number. Note that the purpose of Equation 7.4 is only to correct for the change in design Reynolds number. It is assumed the cascades all have the same values of β_1 , α_2 , t_{max}/c , s/c , and t_{TET}/o , but have had their detailed geometries optimised for their individual design

Reynolds number. In this case the reference Reynolds number should be the value for which the geometry was optimised. For SL2, this value is 600,000. For the Kacker and Okapuu loss system the Reynolds number of 200,000 at which the reference data were collected is appropriate. For future correlations the reference value will have to be determined based on the data from which the correlation is developed. Note that changing a set of data from one reference Reynolds number to another will always change the whole data set by a constant factor.

7.5.5 Future Development of the Reynolds Number Correction

Equation 7.4 is not yet expected to provide a definitive alternative to the Kacker and Okapuu Reynolds number correction for profile losses for all turbine blade rows. This is because the curve fitting coefficients suggested for use with Equation 7.4 were based on CFD for a single cascade, and thus may not be valid for a wide range of geometries. Because it is difficult to obtain experimental data for the full possible range of Reynolds numbers while maintaining a constant Mach number, it is expected that future efforts to improve the Reynolds number correction may rely heavily on CFD. Ideally CFD simulations would be obtained for a range of geometries with a range of design Mach numbers, to develop a Reynolds number correction that also accounts for any influence of Mach number.

In any case, the results of Chapter 5 indicate that the Reynolds number independence of the total pressure loss coefficient for values from 200,000 to

1,000,000, suggested by Kacker and Okapuu, may not be valid. As such, Equation 7.4 may be used as a tentative alternative Reynolds number correction. This model can be fine-tuned through the coefficients a and b as more data becomes available. Additionally, the reference Reynolds number may have to be adjusted as outlined in Section 7.5.4. The tentative Reynolds number correction complete with curve fitting coefficients based on the CFD simulations for SL2 is then

$$f(Re) = \begin{cases} \left(\frac{2 \times 10^5}{6 \times 10^5}\right)^{-0.181} \left(\frac{Re}{2 \times 10^5}\right)^{-0.575} & , Re \leq 2 \times 10^5 \\ \left(\frac{Re}{6 \times 10^5}\right)^{-0.181+0.076\left(\frac{Re-2 \times 10^5}{10^6-2 \times 10^5}\right)} & , 2 \times 10^5 < Re \leq 10^6 \\ \left(\frac{10^6}{6 \times 10^5}\right)^{-0.105} \left(\frac{Re}{10^6}\right)^{-0.2} & , Re > 10^6 \end{cases} \quad 7.6$$

7.6 Subsonic Mach Number Correction

7.6.1 Introduction

With a Reynolds number correction for the SL2 cascade established, the effects of Mach number on the losses can be examined. Since the Reynolds number correction is based on the CFD for the SL2 cascade, the behaviour of the total pressure loss coefficient with Mach number for the SL2 cascade will be the primary basis for determining the Mach number effects. The data collected from the literature will also be considered. However, due to the lack of a more appropriate correction, data from the literature will be adjusted to a common Re_{ref} of 600,000

using the Reynolds number correction developed for the SL2 cascade. Therefore the results for the data from the literature should be treated with some caution.

7.6.2 Subsonic Mach Number Correction in the Kacker and Okapuu Loss System

The subsonic Mach number correction presented by Kacker and Okapuu consists of two parts: an inlet shock correction, Y_{SHOCK} , which is used when the inlet Mach number is above 0.4; and a subsonic compressibility correction factor, K_p . These are applied as follows

$$Y_p = 0.914 \left(\frac{2}{3} Y_{p,AMDc} K_p + Y_{SHOCK} \right) \quad 7.7$$

where

$$K_p = \begin{cases} 1 & M_2 \leq 0.2 \\ 1 - 1.25(M_2 - 0.2) \left(\frac{M_1}{M_2} \right)^2 & M_2 > 0.2 \end{cases} \quad 7.8$$

The factor K_p is intended to correct for the suppression of local separations and the thinning of boundary layers that will occur due to the increased flow acceleration that occurs as the exit Mach number is increased towards 1.0. The prediction of losses due to leading edge shocks in the Kacker and Okapuu system is intended to capture the losses due to shocks that form at the hub, and are thus not applicable to midspan cascade testing. As a result, the inlet shock correction was not considered in this study. Equation 7.8 is illustrated in Figure 7.8 for a range of values of M_1/M_2 .

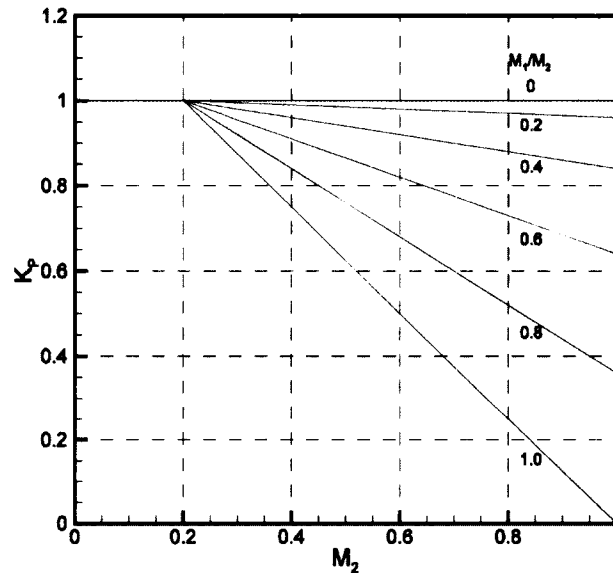


Figure 7.8 Kacker and Okapuu Prediction of Exit Mach Number Effect on Total Pressure Loss Coefficient for Several Values of M_1/M_2

As seen, for an impulse blade, for which $M_1/M_2 = 1.0$, and with an outlet Mach number of $M_2 = 1.0$, $K_p = 0$ and the correction results in a profile loss coefficient that is solely determined by Y_{SHOCK} . It is clearly unreasonable that there is no loss contribution predicted from the blade surface flow. While such an impulse blade row is not expected to occur in a gas turbine engine, it is nevertheless physically realisable, and it is therefore troubling that a correction formula should have such an unphysical limiting behaviour. For this reason, it was decided to re-examine the correction.

For the convergent flow passages typical of gas turbine blade rows, the value of M_1/M_2 is limited by the value of the inlet Mach number M_1 for which the passage chokes. For the cascades in the present database, this value of M_1 at the choking condition varied from 0.25 to 0.54. As a result, the minimum of M_1/M_2 that

occurred was about 0.25 and the minimum K_p was about 0.7. This is illustrated in Figures 7.9 and 7.10 which show the values of K_p predicted by the Kacker & Okapuu correction for all the available cases. Since choking inside the passage typically occurs for a value of the final exit Mach number M_2 slightly below 1.0, the ratio M_1/M_2 for a given blade row actually decreases as M_2 nears 1.0. The net result is an approximately constant value of K_p for a given blade row as M_2 approaches 1.0. As seen in Figure 7.10, the values of M_1/M_2 for the data lie mostly between 0.3 and 0.5. The exceptions are the HS1A, HS1C, and HS1D data (Corriveau 2005) which have values of M_1/M_2 between about 0.6 and 0.75.

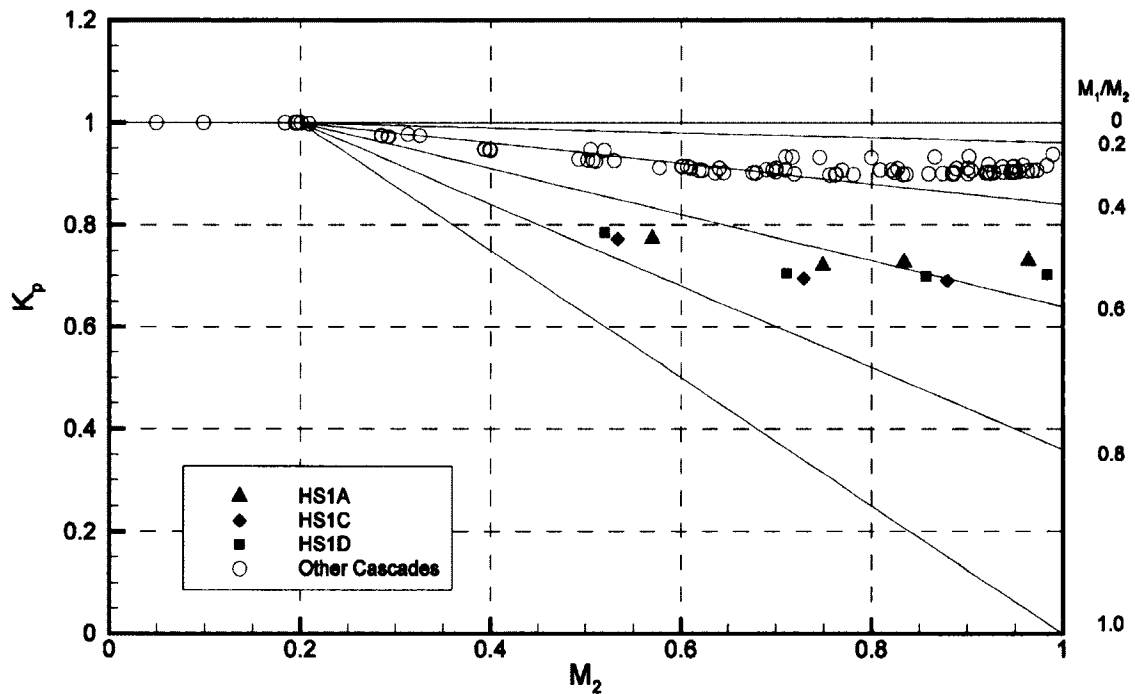


Figure 7.9 Kacker and Okapuu Prediction of Exit Mach Number Effect on Total Pressure Loss Coefficient for Several Cascades

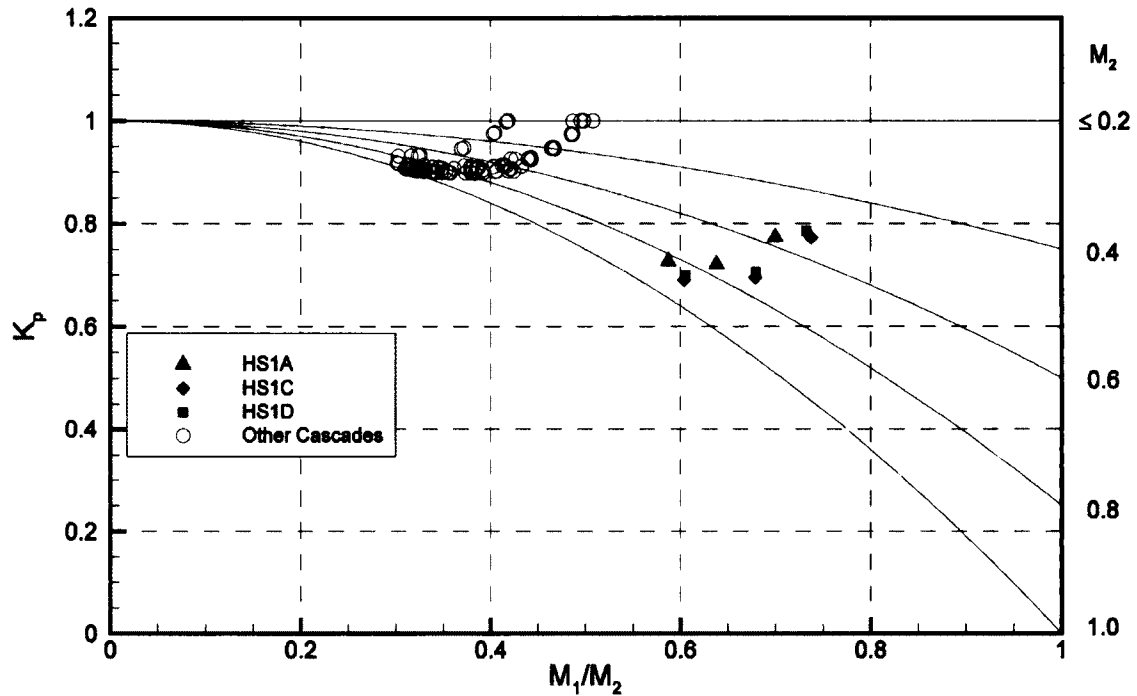


Figure 7.10 Kacker and Okapuu Prediction of Flow Acceleration Effect on Total Pressure Loss Coefficient for Several Cascades

7.6.3 Estimation of the Incompressible Limit

The Kacker and Okapuu compressibility correction is based on adjusting by the factor K_p the profile losses predicted at incompressible conditions. The total pressure losses corrected for Reynolds number with Equation 7.6 were used to estimate this incompressible limit for the losses:

$$Y_{corr,inc} = Y_{corr}(M_2 = 0) \quad 7.9$$

Because K_p is a factor relating the losses predicted at the incompressible conditions to those predicted at compressible conditions, the ratio of Y_{corr} to $Y_{corr,inc}$

will be used to evaluate the change of the loss coefficient from its incompressible value as the Mach number increases:

$$K_{corr} = \frac{Y_{corr}}{Y_{corr,inc}} \quad 7.10$$

K_{corr} is in effect the measured value of K_p .

As defined in Equations 7.5 and 7.9 above, the incompressible limit of the losses corrected to the reference Reynolds number is referred to as $Y_{corr,inc}$, and Y_{corr} refers to the losses corrected to the reference Reynolds number through Equation 7.4. These corrections have been applied for all cascades in the collected data set, even though the Reynolds number correction Equation 7.6 was based solely on the SL2 CFD data.

Note that the factor K_p from the Kacker and Okapuu loss system is used to adjust the losses for compressibility effects from a cascade designed for incompressible conditions. The estimate for the incompressible limit is based on extrapolating from the lowest Mach number at which the cascades were tested. These mach numbers were typically much lower than the design Mach numbers for the respective cascades. Consequently the loading distributions, and therefore the surface boundary developments, were far from optimum. In effect, the incompressible loss levels are estimated from data at “off-design” Mach numbers. Therefore one might expect the losses to be higher than they would be for a cascade that had been designed and optimised for the lower Mach number, but otherwise had the same inlet and outlet flow angles and the same solidity and maximum

thickness. For this reason, the loss values obtained by extrapolating to the incompressible limit are expected to be high.

Note that Equation 7.6 uses the reference Reynolds number of 600,000 which is most appropriate for the SL2 data. The other cascades in this study are mostly high pressure turbine profiles. Since high pressure turbines typically have design Reynolds numbers much higher than 200,000, the reference Reynolds number of 600,000 may in fact be a more appropriate value than the 200,000 used in the Kacker and Okapuu loss system.

The use of a reference Reynolds number of 600,000 allows all the results to be directly compared. If the design Reynolds number for each cascade had been used, which may be more appropriate as suggested by Section 7.5.4, then all the results for each cascade would be different by a factor that would be constant for a given cascade. Since the estimated value for the incompressible limit would also be adjusted by the same factor as the rest of the data for each cascade, the value of K_{corr} will be independent of the choice of reference Reynolds number.

The estimation of the incompressible limit was done with a linear extrapolation for the data at the lowest Mach numbers for each cascade, as demonstrated in Figure 7.11 for HS1C. The incompressible limits of the losses estimated for each cascade are tabulated in Appendix F. In the case of the HS2 cascade, data were available for the same cascade geometry for four European wind tunnels as well as the Carleton facility, and the incompressible limit was estimated separately for each wind tunnel. The linear fit was extended to a Mach number of

0.3 where the losses are expected to reach a constant value. The value of 0.3 was chosen because the SL2 Reynolds number corrected loss coefficient in Figure 7.7 is constant at a Mach number of 0.3. On the other hand, the Kacker and Okapuu correction assumes that the incompressible limit is reached only at $M_2 = 0.2$.

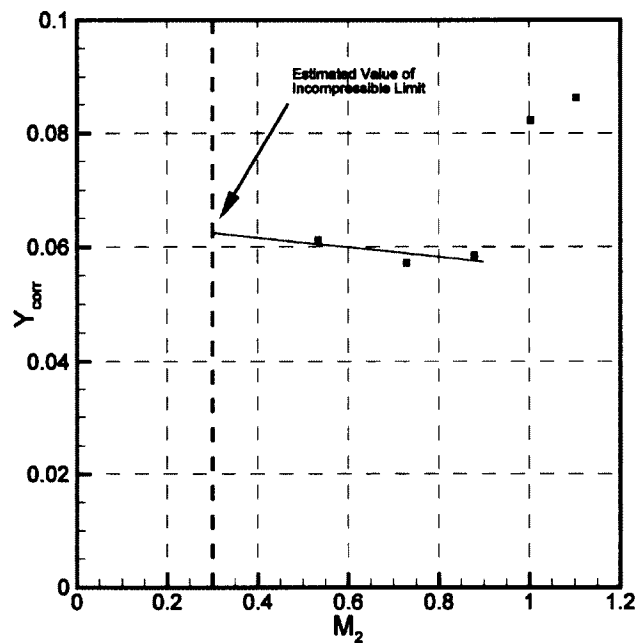


Figure 7.11 Estimate of the Incompressible Limit of the Reynolds Number Corrected Total Pressure Loss Coefficient for HS1C

7.6.4 Dependence of Incompressible Limit on the Testing Facility

As discussed in the previous section, data were available for the HS2 cascade geometry for four European wind tunnels as well as the Carleton facility. The data from only three of these European wind tunnels will be considered because of some concerns raised by Kiock et al. (1986) about the quality of the data from the fourth

facility. The incompressible limit was estimated separately for each wind tunnel as shown in Figure 7.12.

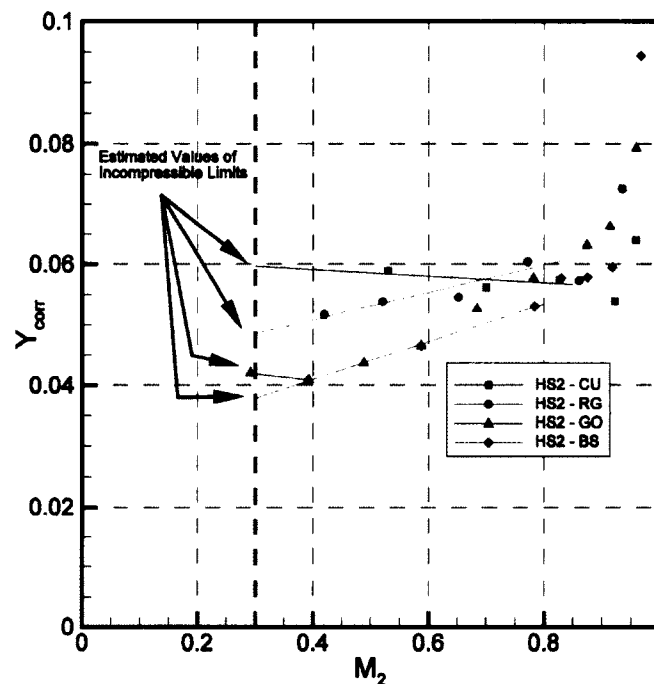


Figure 7.12 Estimation of the Incompressible Limit for HS2 Based on Data from Four Different Wind Tunnels

As seen in Figure 7.12, the estimated value of $Y_{corr,inc}$ for HS2 varies from 0.038 to 0.06. This is partly due to the higher uncertainty at lower Mach numbers, as discussed in Section 4.6.3. Due to the sensitivity to error, obtaining an accurate estimate of the incompressible limit for these losses is especially difficult. The data in this study come from experiments focused on Mach numbers above 0.6; improving the estimate for the incompressible limit for any cascade will require investigations that include exit Mach numbers below about 0.4 and prefer lower.

The incompressible limit is used to calculate the ratio of Y_{corr} to $Y_{\text{corr,inc}}$. This ratio is referred to as K_{corr} , as defined in Equation 7.10 above. K_{corr} is in effect the measured value of K_p and can be compared with the value of K_p given by the Kacker and Okapuu correction. Since $Y_{\text{corr,inc}}$ is in the denominator of K_{corr} , the wide range of values of $Y_{\text{corr,inc}}$ obtained for HS2 for the different facilities has a large effect on the value of K_{corr} , as shown in Figure 7.13.

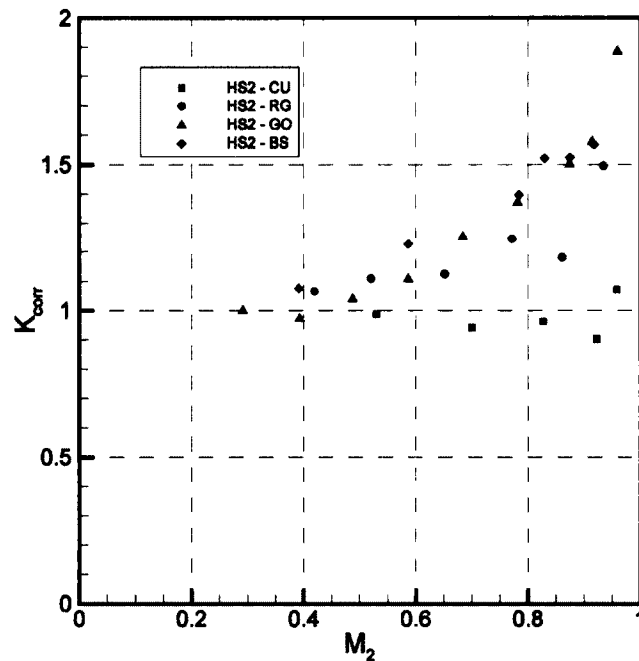


Figure 7.13 Ratio of Reynolds Number Corrected Total Pressure Loss Coefficient to Incompressible Limit for the HS2 Cascade from Four Different Wind Tunnels

Due to the range of values estimated for the incompressible limit, the variation in the total pressure loss coefficient with Mach number depends on the source of the data. It is also possible that the differences in the incompressible limits is partly the result of some unaccounted for difference in the operating

conditions of the different wind tunnels, such as turbulence intensity or length scale. The turbulence intensity in the European wind tunnels was measured to be 1% or less, while the turbulence intensity in the Carleton wind tunnel is typically around 4%. For these reasons, only the HS2 data from the Carleton facility will be used when evaluating the Kacker and Okapuu loss system.

7.6.5 Evaluation of Subsonic Correction Factor from Kacker and Okapuu Loss System

The Kacker and Okapuu subsonic Mach number correction, given by Equation 7.8 and shown in Figure 7.8, indicates that there is no effect of compressibility below outlet Mach numbers of 0.2. For M_2 from 0.2 to 1.0 the profile loss coefficient is predicted to decrease as a function of M_2 and M_1/M_2 , where M_1/M_2 is a measure of the flow acceleration through the blade passage. For a highly accelerated flow, or low value of M_1/M_2 , the decrease is relatively small. As noted in Section 7.6.2, for impulse blades, for which $M_1/M_2 \cong 1.0$, the reduction in losses is greatest.

The Kacker and Okapuu subsonic Mach number correction is intended to account for the suppression of local separations and the thinning of boundary layers due to accelerating flow. As seen in Figure 7.14, the losses for SL2 rise significantly above $M_2 = 0.9$. This was identified in Chapters 5 and 6 as being the result of shock losses, which are not expected to be accounted for by the Kacker and Okapuu subsonic Mach number correction. For this reason, the Mach number at which

shock losses appear was estimated for each cascade, as illustrated in Figure 7.14 for SL2. These values are tabulated in Appendix F.

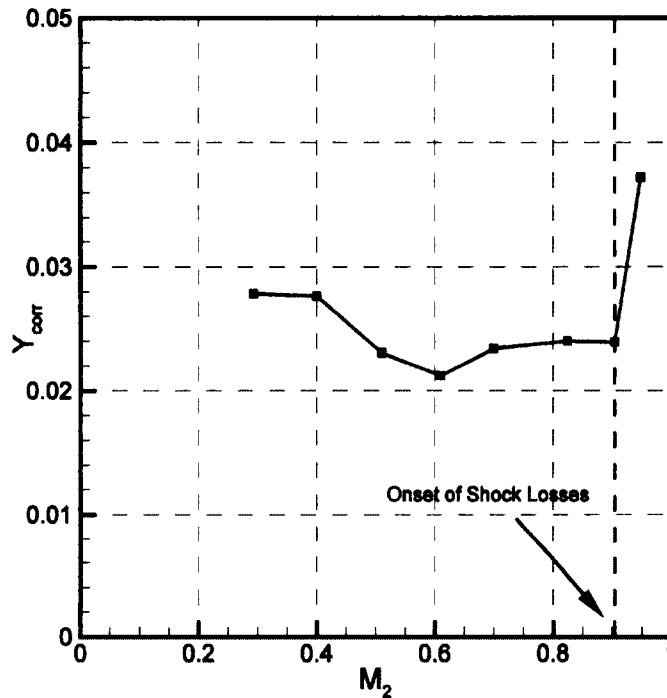


Figure 7.14 Variation of Y_{corr} with Mach number for SL2 Showing Onset of Shock Losses

Figure 7.15 compares the values of K_p against K_{corr} ; the latter is essentially the measured value of K_p for the collected data. Data which included shock losses have been identified. In Section 7.6.3, it was noted that the incompressible limit used to calculate K_{corr} is based on off-design data, and may thus be higher than the true incompressible limit of losses for equivalent design point data. As such, the values of K_{corr} in Figure 7.15 may be less than the values that should ideally be used.

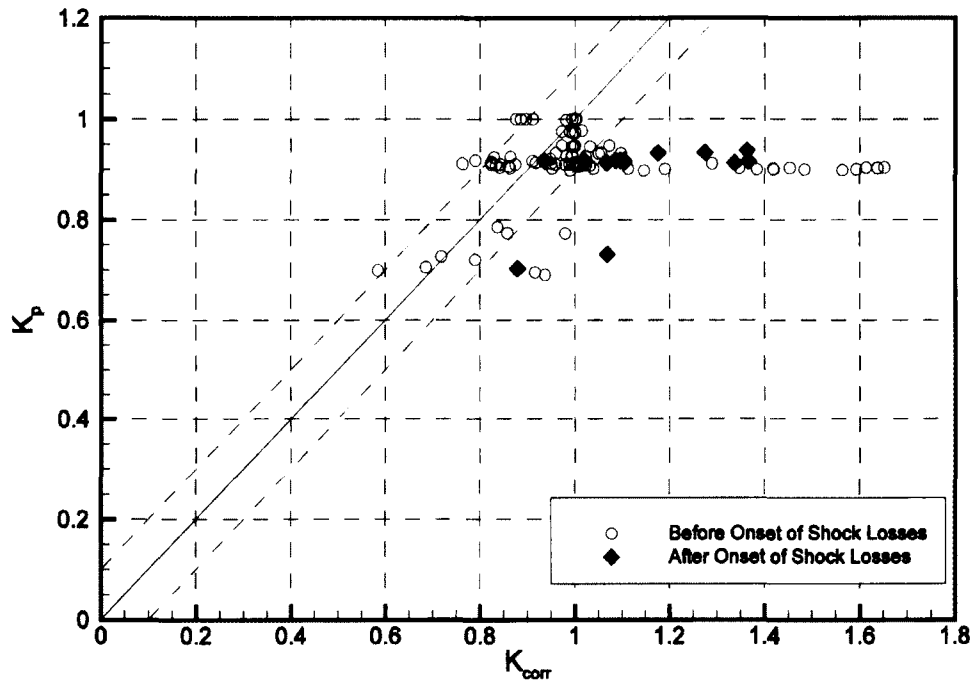


Figure 7.15 Evaluation of Compressibility Correction K_p against K_{corr} Indicating Data which Included Shock Losses

As expected, Figure 7.15 indicates that the Kacker and Okapuu subsonic Mach number correction does not predict the rise in losses due to the appearance of shock waves in the flow. However, Figure 7.15 also includes data points for which no shock losses appeared to be present but for which the experimentally obtained values of K_{corr} are nevertheless considerably higher than those predicted by K_p . These data are from two cascades: the SL1 cascade tested at Carleton by Taremi (2010) and the OX cascade tested at Oxford by Mee et al. (1992). These are cases for which the subsonic losses rose as M_2 increased, rather than decreased as predicted by the Kacker and Okapuu correction. Figure 7.16 shows the variation of K_p with K_{corr} for the same results as Figure 7.15 but with the data with shock losses omitted

and with the SL1 and OX cascades highlighted. The reason that these two cascades give a different trend has not been identified, but it may be partly due to the fact that the incompressible limits for these cascades were extrapolated from data obtained from higher than Mach 0.6.

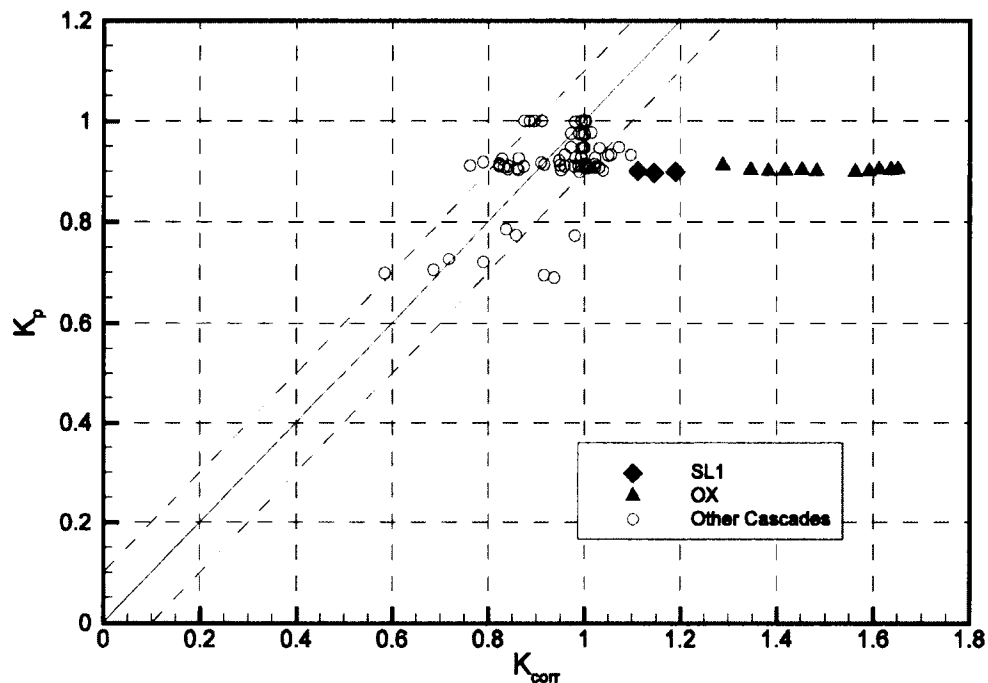


Figure 7.16 Evaluation of Compressibility Correction K_p against K_{corr} Indicating Data from the SL1 and OX Cascades

Figure 7.17 evaluates the values of K_p against K_{corr} , omitting the data for the SL1 and OX cascades as well as the data which included shock losses. The data lie mostly within ± 0.1 of the value predicted by Kacker and Okapuu. This appears to support the prediction of the Kacker and Okapuu loss system that increasing the exit Mach number will reduce the total pressure loss coefficient. However, since only six of the eight cascades evaluated follow this trend, there may be room for further

improvement to the Kacker and Okapuu subsonic Mach number correction to encompass the behaviour of the other two cascades.

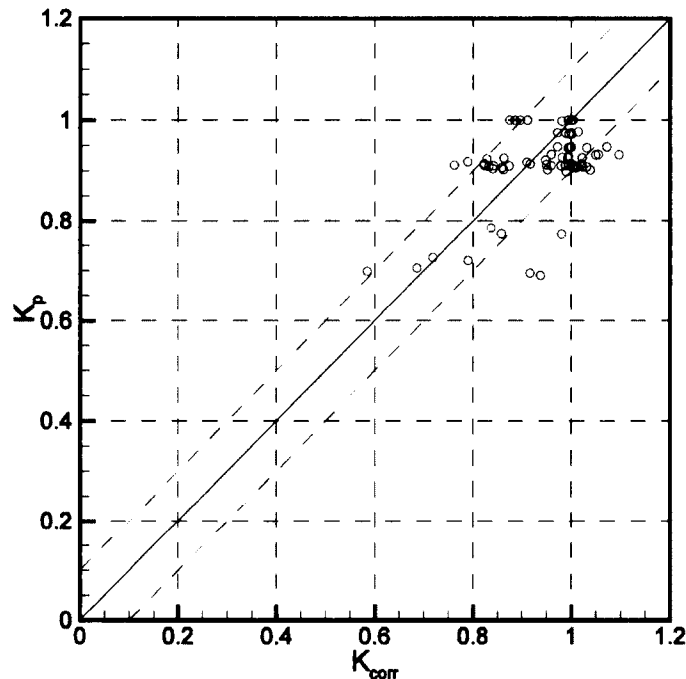


Figure 7.17 Evaluation of Compressibility Correction K_P against K_{corr}

7.6.6 Onset of Shock Losses Within the Blade Passage

Above a Mach number of about 0.9, the SL2 results showed a large rise in total pressure loss coefficient. This is consistent with the results of the data in the literature, although some of the cascades showed a rise at a Mach number as low as 0.8, as summarised in Appendix F. The rise in losses can be attributed to the appearance of shock waves in the flow, as sections of the flow will locally become supersonic while the mixed-out exit Mach number is still subsonic. This indicates that a loss correlation that accounts for shock losses in the passage should be

applied for exit Mach numbers less than 1.0. While the Mach number at which shock losses will first appear is not the same for all geometries, the Mach number of 0.9 indicated by the SL2 results is expected to provide a more reasonable estimate than the value of 1.0 currently used by the Kacker and Okapuu system.

7.6.7 Suggested Improvements to the Subsonic Mach Number

Design Correction

Given the above results, the data in this study are considered insufficient to develop an improvement to the Kacker and Okapuu subsonic Mach number correction factor, K_p , for the total pressure loss coefficient. However, it is suggested that the correction for shock losses should be applied when the exit Mach numbers exceed 0.9. This value is based primarily on the onset of shock losses for the SL2 cascade. Future efforts to improve the correction should preferably include a prediction for the Mach number at which the shock losses will appear based on the geometric information available in the early stages of design. It is beyond the scope of this study to develop such a new correction.

7.6.8 Discussion and Recommendations for Future

Development of Subsonic Mach Number Loss Corrections

As discussed in Chapter 5, the small changes in loss coefficient due to Mach number effects calculated by the CFD are attributed to the development of the second suction peak in the blade loadings and the movement of the transition

location towards the trailing edge. Both of these effects are geometry specific and will be difficult to build into a general correlation unless they can be controlled with geometric parameters that are known early in the design. The data in this study is insufficient to determine how the blade loading will influence the Mach number effects on losses. Neither the change in transition location due to Mach number nor the effect it has on the total pressure loss coefficient can be predicted from the data in this study.

Because the effect of Mach number on total pressure loss coefficient appears to be largely a result of the overall blade loading and the influence of Mach number on the transition location, further efforts to determine the effect of compressibility on losses will likely incorporate measures of these factors. Blade loading is usually chosen early in the design based on a blade loading parameter, such as the Zweifel coefficient. However, the transition location is not estimated until late in the design when detailed CFD is performed. Incorporating the transition location into a correction for compressibility effects will require a general prediction of the transition location. Such a prediction can be expected to be based on aspects of both the flow and geometry. Some of the relevant flow parameters are the Reynolds number, turbulence intensity and length scale, and a measure of the overall channel acceleration, such as M_1/M_2 . Additionally, the location of the suction peak will have a significant effect on the transition location. The location of the suction peak will be affected by geometric parameters such as stagger angle and unguided turning. Because the location of the suction peak will also be affected by the detailed

curvature distribution, a method for predicting the transition location that can be used at an early stage of the design will only be approximate.

The improvements suggested here are based on limited data sets. Of particular note is the fact that the data examined are for the losses above $M_2 = 0.6$, while the design Mach numbers are all at or above 0.8. The addition of data for cascades with design Mach numbers below about 0.4, and preferably lower, would be useful for determining the incompressible limit. Ideally a set of cascades with similar geometric parameters, such as metal angles and trailing edge thickness, but with different design Mach numbers from 0 to 1.0 would be tested. Additionally the range of M_1/M_2 in this study was also limited, with most of the data between 0.3 and 0.5. Since this study was motivated by a shortcoming in the Kacker and Okapuu loss system that would be evident at high values of M_1/M_2 and high exit Mach numbers, it would be of particular interest to have data for geometries with such high values of M_1/M_2 .

Since producing a set of geometries which vary M_2 and M_1/M_2 over large ranges may not be feasible, the use of CFD may prove valuable to obtain a larger set of data for use in developing an improved correlation. Since such a study would require using CFD outside the normal ranges of testing, it would be essential to supplement the CFD with experimental cases for validation. However, the airfoils would still need to be designed which would require access to the tools to design a series of cascades that reflect state-of-the-art industrial turbine airfoil design.

Chapter 8

Conclusions and Recommendations

8.1 Conclusions

The primary objective of this study was to evaluate the effect of subsonic compressibility on midspan losses in a turbine cascade.

An improved wind tunnel control system has been implemented successfully. The improved control system allows for less variation in Mach number during the run, as well as reduced settling time. The new control system also allows the wind tunnel to be run at Mach numbers as low as 0.1 whereas the old control system was usable only down to Mach numbers of about 0.55. In addition to the improved quality of the control, the new control system includes an improved user interface.

The detailed experimental and computational results were presented for the midspan performance of the SL2 turbine cascade. Experimental results were obtained for Mach numbers between 0.2 and 1.0 with the Reynolds number corresponding to an atmospheric pressure at the exit of the diffuser. The resulting range of Reynolds numbers based on true chord and cascade outlet velocity was from about 150,000 to 830,000.

The computed blade loadings indicate that changes to the Reynolds number result in only minor differences to the blade loadings, while changes to the Mach number changed the blade loadings significantly. The Reynolds number effects on the computed blade loadings were determined to be the result of changes to the transition location on the suction surface. It is not known whether the transition location shows similar changes in the experiment. The Mach number effects on the blade loadings resulted in the development of a second suction peak as well as overall increased blade loading.

Some of the computed blade loadings, especially at high Mach numbers, showed evidence of flow separation in the form of a pressure plateau which varied in size with Reynolds number. However, only the cases above a Mach number of about 0.89 showed actual reversed flow; all the other computed cases remained attached. Investigation of the boundary layers indicated that the flows were in the process of separating at the point of transition. This resulted in a peak in the displacement thickness, which results in a pressure distribution suggesting separation.

The results of the simulations indicated that the Mach number had a small influence on the exit angle, increasing the exit angle by 1.2 degrees as the Mach number increased from 0.05 to 0.94, while the effect of Reynolds number on exit angle was negligible. This increase in exit angle with Mach number can be largely explained by the increased blade loading at higher Mach numbers.

The computed results indicate that the effect of both the Reynolds number and Mach number on the total pressure losses have a similar magnitude for the range studied. While the simulations predicted total pressure loss coefficients between roughly 1.2 and 1.6 times larger than the experiment, the changes in losses with operating point measured by the experiment are similar to those from the simulations. This supports the conclusion that the Reynolds number and Mach number effects on losses are of a similar magnitude for the range studied. The Reynolds number effects on losses are essentially due to the effect of Reynolds number on the boundary layer development, especially regarding the location of transition. The effect of Mach number on the losses can be attributed both to the change in the loading distribution and the change in the transition location. As the Mach number was increased, the blade loading developed a second suction peak and the simulations predict that the transition location shifted towards the rear of the blade. These effects had a tendency to increase and decrease the losses respectively, with the net effect being very little variation in the total pressure loss coefficient.

These results were combined with data from the open literature to develop tentative improvements for the correction factors for Reynolds number and Mach number effects on profile losses in the Kacker and Okapuu loss prediction system. These improvements include a prediction for the Reynolds number effects between 200,000 and 1,000,000 that is based on the CFD results for the SL2 cascade. The proposed correction factor for Reynolds number effects predicts that the profile losses will decrease by about 22% as the Reynolds number increases from 200,000

to 1,000,000. The Kacker and Okapuu loss system predicts there will be no change in this range. Also, it was observed that the shock losses will affect the losses before an exit Mach number of 1.0. In the absence of a method for predicting the onset of shock losses, it is tentatively recommended that the onset of shock losses be predicted to occur at about $M_2 = 0.9$. While the data were insufficient to improve the Kacker and Okapuu subsonic Mach number correction further, a number of shortcomings were identified. The predicted losses for high values of M_1/M_2 are unrealistically small. Additionally, while the Kacker and Okapuu subsonic Mach number correction predicts that an increase in Mach number will always result in decreased total pressure loss coefficient, two of the eight cascades examined had the opposite trend. Because these tentative improvements rely on the CFD results for a single cascade to separate the Reynolds effects from the Mach number effects, they will require further confirmation before they can be used for general profile loss prediction.

8.2 Recommendations for Future Work

The results of this study have highlighted several areas of interest which will benefit from future investigations.

When investigating the effect of Mach number on the losses generated in a turbine, it is common to assume that the Reynolds number will not have a significant effect on the losses, provided the Reynolds numbers are large. While the Reynolds number effects on losses are small, this study has shown that they are on

the same order as the Mach number effects in the subsonic range. Any efforts to interpret the effect of Mach number on losses should thus attempt to remove any Reynolds number effects. This can be accomplished by including experimental or computational test cases which maintain a constant Reynolds number. Accomplishing this experimentally is challenging when the wind tunnel used discharges to atmosphere as is the case with the Carleton High Speed Wind Tunnel. Where these options are unfeasible, correlations may be used to estimate the effect of Reynolds number, although the results should then be treated with some caution. Similarly, any efforts to interpret the effect of Reynolds number on losses should attempt to remove any Mach number effects through experiments, computations, or where necessary, through correlations.

Further, because transition appears to play an important role in the development of losses with Mach number, it will be beneficial to investigate the effect of Mach number on transition. Predicting the effect of Mach number on losses at an early stage of design will likely require some means of predicting the movement of the transition point. While this study used computational results to predict the transition location, the transition model has not been validated for Mach number effects. Therefore, it will be important to include experimental results for any investigations on the Mach number effect on transition. Transition location can be measured with surface hot film anemometry. While this is feasible in the Carleton High Speed Wind Tunnel, obtaining hot film measurements is a challenging task. Transition location can also sometimes be inferred from surface flow

visualisation techniques by identifying where the shear stress increases rapidly, although the interpretation of the results can be more difficult than with hot film anemometry.

The suggested improvements to the Kacker and Okapuu loss system indicate that the total pressure loss coefficient will decrease with Mach number up to Mach 0.9 at which point the effects of shock waves will begin to show. However, the Mach number at which shock waves begin to form will be a function of the geometry. A method for estimating the Mach number at which shock losses will appear based on simple geometric parameters would provide a valuable future improvement.

While every effort has been made to ensure the data is of good quality, the uncertainty in the data at low Mach numbers is significant. It is suggested that future correlations should include studies performed in both high and low speed facilities on geometrically similar cascades in order to measure the incompressible limit of the loss coefficient reliably. This is complicated by the fact that low speed facilities typically operate at significantly lower Reynolds numbers than high speed facilities. In order to compare the data from both high and low speed facilities, the Reynolds numbers must be matched. While some facilities, such as the Carleton High Speed Wind Tunnel, are capable of a limited degree of independent Reynolds number and Mach number control, achieving the range of Reynolds number control necessary to match the results from a low speed facility is usually not possible.

The suggested improvements to the Reynolds and Mach number corrections are based on limited data sets. Of particular note is the fact that the data examined

are mostly concerned with the losses above $M_2 = 0.6$, while the design Mach numbers are all at or above 0.8. The addition of data for cascades with design Mach numbers below about 0.4, and preferably lower, would be useful for determining the incompressible limit. However, such data would have limited additional value since gas turbines do not generally have design Mach numbers in this range. Additionally the range of M_1/M_2 in this study was also limited with most of the data having values between 0.3 and 0.5. Since this study was motivated by a shortcoming in the Kacker and Okapuu loss system that would be evident at high values of M_1/M_2 and high exit Mach numbers, data for geometries with high values of M_1/M_2 would be particularly useful for evaluating and improving the Kacker and Okapuu Mach number correction in this range. Again, however, this data may be of limited value since impulse or near impulse turbines are not typically used in gas turbines.

References

- Ainley, D. G. and Mathieson, G. C. R. (1951), "A Method of Performance Estimation for Axial-Flow Turbines," British ARC, R&M, **2974**.
- Anderson, J. D., (2005), *Fundamentals of Aerodynamics*, 4th Edition, McGraw-Hill, New York, NY.
- Argüelles Díaz, K. M., Fernández Oro, J. M., Blanco Marigorta, E., (2009), "Cylindrical Three-Hole Pressure Probe Calibration for Large Angular Range," *Flow Measurement and Instrumentation*, **20**, 57-68.
- Benner, M., (2003), "Influence of Leading-Edge Geometry on Profile and Secondary Losses in Turbine Cascades," Ph.D. thesis, Carleton University, Ottawa, Canada.
- Binder, A., Schroeder, T., and Hourmouziadis, J., (1989), "Turbulence Measurements in a Multistage Low-Pressure Turbine," *ASME Journal of Turbomachinery*, **111**, pp. 153-161.
- Boyle, R. J., Lucci, B. L., Senyitko, R. G. (2002), "Aerodynamic Performance and Turbulence Measurements in a Turbine Vane Cascade," NASA TM 2002-211709.
- Carscallen, W. E., Gostelow, J. P., and Mahallati, A., (2009), "Some Vortical Phenomena in Flows Over Transonic Turbine Nozzle Vanes Having Blunt Trailing Edges," ISABE-2009-1216.

- Corriveau, D. (2005), "Influence of Loading Distribution on the Performance of High Pressure Turbine Blades," Ph.D. thesis, Carleton University, Ottawa, Canada.
- Corriveau, D., and Sjolander, S. A., (2006), "Influence of Loading Distribution on the Off-Design Performance of High-Pressure Turbine Blades," *ASME Journal of Turbomachinery*, **129**, 563-571.
- Coton, T., Arts, T., and Lefebvre, M., (2001), "Effects of Reynolds and Mach Numbers on the Profile Losses of a Conventional Low-Pressure Turbine Rotor Cascade with an Increasing Pitch-Chord Ratio," *Proc. Instn. Mech. Engrs., J. Power and Energy*, **215 Part A**, 763-772.
- Delery, J., and Marvin, J. G., (1986), "Shock-Wave Boundary Layer Interactions," AGARD-AG-280.
- Denton, J. D., and Xu, L., (1990), "The Trailing Edge Loss of Transonic Turbine Blades," *ASME Journal of Turbomachinery*, **112**, 277-285.
- Denton, J. D., (1993), "Loss Mechanisms in Turbomachines," *ASME Journal of Turbomachinery*, **115**, pp. 621-656.
- Dunham, J., and Came, P. M., (1970), "Improvements to the Ainley-Mathieson Method of Turbine Performance Prediction," *ASME Journal of Engineering for Power*, **92**, pp. 252-256.
- Haller, B. R., and Camus, J. J., (1984), "Aerodynamic Loss Penalty Produced by Film Cooling Transonic Turbine Blades," *ASME Journal of Engineering for Gas Turbines and Power*, **106**, pp. 198-205.

- Hoheisel, H., Kiock, R., Lichtfuss, H. J., and Fottner, L., (1987), "Influence of Free-Stream Turbulence and Blade Pressure Gradient on Boundary Layer and Loss Behaviour of Turbine Cascades," *ASME Journal of Turbomachinery*, **109**, pp. 210-219.
- Hourmouziadis, J., (1989), "Aerodynamic Design of Low Pressure Turbines," AGARD-LS-167.
- Islam, A. M. T., (1999), "An Experimental and Computational Study of the Aerodynamics of Turbine Blades with Damage," Ph.D. thesis, Carleton University, Ottawa, Canada.
- Japikse, D., and Baines, N. C., (1994), *Introduction to Turbomachinery*, 1st Edition, Concepts ETI, Oxford University Press, Oxford, UK.
- Jeffries, M. S., (2000), "Initial Investigations of Transonic Turbine Aerodynamics Using the Carleton University High-Speed Wind Tunnel," Ph.D. thesis, Carleton University, Ottawa, Canada.
- Jouini, D. B. M., (2000), "Experimental Investigation of Two Transonic Linear Turbine Cascades at Off-Design Conditions," Ph.D. thesis, Carleton University, Ottawa, Canada.
- Jouini, D. B. M., Sjolander, S. A., and Moustapha, S. H., (2002), "Midspan Flow-Field Measurements for Two Transonic Linear Turbine Cascades at Off-Design Conditions," *ASME Journal of Turbomachinery*, **124**, pp. 176-186.

- Kacker, S. C., and Okapuu, U., (1982), "A Mean Line Prediction Method for Axial Flow Turbine Efficiency," *ASME Journal of Engineering for Power*, **104**, pp. 111-119.
- Kiock, R., Lehthaus, F., Baines, N. C., and Sieverding, C. H., (1986), "The Transonic Flow Through a Plane Turbine Cascade as Measured in Four European Wind Tunnels," *ASME Journal of Engineering for Gas Turbines and Power*, **108**, 277-284.
- Kline, S. J., and McClintock, F. A., (1953), "Describing Uncertainties in Single-Sample Experiments," *Mechanical Engineering*, **75**, pp. 3-8.
- Kurosaka, M., Gertz, J. B., Graham, J. E., Goodman, J. R., Sundaram, P., Riner, W. C., Kuroda, H., and Hankey, W. L., (1987), "Energy Separation in a Vortex Street," *Journal of Fluid Mechanics*, **178**, pp.1-29.
- Ladwig, M., and Fottner, L., (1993), "Experimental Investigations of the Influence of Incoming Wakes on the Losses of a Linear Turbine Cascade," ASME paper No. 93-GT-394.
- Langtry, R. B., and Menter, F. R., (2005), "Transition Modeling for General CFD Applications in Aeronautics," AIAA 2005-522.
- Langtry, R. B., Menter, F. R., Likki, S. R., Suzen, Y. B., Huang, P. G., and Völker, S., (2006), "A Correlation-Based Transition Model Using Local Variables Part II – Test Cases and Industrial Applications," *ASME Journal of Turbomachinery*, **128**, pp. 423-434.

- Li, S. M., Chu, T. L., Yoo, Y. S., and Ng, W. F., (2002), "Transonic Flow Losses of Two Steam Turbine Blades at Large Incidences," ASME paper No. GT-2002-30334.
- Li, S. M., Chu, T. L., Yoo, Y. S., and Ng, W. F., (2004), "Transonic and Low Supersonic Flow Losses of Two Steam Turbine Blades at Large Incidences," ASME Journal of Fluids Engineering, **126**, pp. 966-975.
- Mayle, R. E., (1991), "The Role of Laminar-Turbulent Transition in Gas Turbine Engines," ASME Journal of Turbomachinery, **113**, pp. 509-537.
- Mee, D. J., Baines, N. C., Oldfield, M. L. G., Dickens, T. G., (1992), "An Examination of the Contributions to Loss on a Transonic Turbine Blade in Cascade," ASME Journal of Turbomachinery, **114**, pp. 155-162.
- Menter, F. R., Langtry, R. B., Likki, S. R., Suzen, Y. B., Huang, P. G., and Völker, S., (2006), "A Correlation-Based Transition Model Using Local Variables Part I – Model Formulation," ASME Journal of Turbomachinery, **128**, pp. 413-422.
- Moustapha, S. H., Carscallen, W. E., and McGeachy, J. D., (1993), "Aerodynamic Performance of a Transonic Low Aspect Ratio Turbine Nozzle," ASME Journal of Turbomachinery, **115**, pp. 400-408.
- Perdichizzi, A., (1990), "Mach Number Effects on Secondary Flow Development Downstream of a Turbine Cascade," ASME Journal of Turbomachinery, **112**, pp. 643-651.
- Rodger, P., Sjolander, S. A., and Moustapha, S., (1992), "Establishing Two-Dimensional Flow in a Large-Scale Planar Turbine Cascade," AIAA paper No. 92-3066.

- Scribner, C. A., (2011), Private Communication, Carleton University, Ottawa, Canada.
- Sieverding, C. H., Stanilas, M., and Snoeck, J., (1980), "The Base Pressure Problem in Transonic Cascades," *ASME Journal of Engineering for Gas Turbines and Power*, **102**, pp. 711-718.
- Song, B., Ng, W. F., Cotroneo, J. A., Hofer, D. C., and Siden, G., (2007), "Aerodynamic Design and Testing of Three Low Solidity Steam Turbine Nozzle Cascades," *ASME Journal of Turbomachinery*, **129**, pp. 62-71.
- Šťastný, M., Šafařík, P., Hořejší, I., and Matas, R., (1997), "Flow Around the Sections of Rotor Blading of a Turbine Stage with Relatively Long Blades at Off-Design Conditions," *Proc. Instn. Mech. Engrs., J. Power and Energy*, **211 Part A**, pp. 207-213.
- Taremi, F., Sjolander, S. A., and Praisner, T. J., (2010), "Measurements of Endwall Flows in Transonic Linear Turbine Cascades: Part I – Low Flow Turning," *ASME paper No. GT2010-22759*.
- Taremi, F., Sjolander, S. A., and Praisner, T. J., (2010), "Measurements of Endwall Flows in Transonic Linear Turbine Cascades: Part II – High Flow Turning," *ASME paper No. GT2010-22760*.
- Taremi, F., (2010), Private Communication, Carleton University, Ottawa, Canada.
- Treaster, A. L., and Yocum, A. M., (1978), "The Calibration and Application of Five-Hole Probes," *NAVSEA TM-78-10*.
- Van Driest, E. R., (1952), "Investigation of Laminar Boundary Layer in Compressible Fluids Using the Crocco Method," *NACA TN 2597*.

-
- Zhang, Q., Sandberg, D., and Ligrani, P. M., (2005), "Mach Number and Freestream Turbulence Effects on Turbine Vane Aerodynamic Losses," *AIAA Journal of Propulsion and Power*, **21 no. 6**, pp. 988-996.
- Zhu, J., and Sjolander, S. A., (2005), "Improved Profile Loss and Deviation Correlations for Axial Turbine Blade Rows," ASME paper No. GT2005-69077.

Appendix A

Three-Hole Probe Calibration

A.1 Calibration Procedure

A calibration is required in order to convert the pressures read by the three-hole probe into the desired information: total pressure, static pressure, and flow angle. As explained by Treaster and Yocum (1978), the calibration must use pressure coefficients that are independent of velocity and are a function only of the flow angularity. The coefficients used for this calibration are

$$C_{\alpha} = \frac{P_2 - P_3}{P_1 - \bar{P}} \quad \text{A.1}$$

$$C_{P_0} = \frac{P_0 - P_1}{P_1 - \bar{P}} \quad \text{A.2}$$

$$C_{P_s} = \frac{P_0 - P_s}{P_1 - \bar{P}} \quad \text{A.3}$$

where

$$\bar{P} = \frac{P_2 + P_3}{2} \quad \text{A.4}$$

To generate the calibration coefficients, the probe is mounted in the calibration rig. The calibration rig can generate flow conditions at a specified Mach number while the probe is rotated in the yaw direction. To correct for asymmetry in the probe and misalignment of the calibration jet, the probe undergoes aerodynamic alignment at each Mach number to be calibrated. Aerodynamic alignment is

performed by measuring C_α for a range of yaw angles, rolling the probe 180° and measuring C_α again. The intersection of the two curves of C_α versus yaw angle will correspond to the aerodynamic centre of the probe where the yaw angle between the probe and the calibration jet is zero. Once the probe is aerodynamically aligned, measurements are taken for the full range of yaw angles for which the probe is being calibrated. This process is repeated five times at each Mach number, and the average pressures from the five runs are used to generate the calibration coefficients at each combination of Mach number and yaw angle. The runs are repeated five times to reduce the scatter in the data. The choice of five runs was considered to be sufficient because the results did not change significantly when the number of runs was increased from four to five. While performing five runs reduces the scatter, it was found that the scatter at the lowest Mach number, namely 0.20, was too large. To extend the calibration to this Mach number, the calibration was performed in the low speed facility described by Benner (2003). Once the calibration coefficients are determined, best fit curves are applied at each Mach number to define the final calibration.

The typical procedure used to determine the values of interest from these coefficients is outlined in Figure A.1. The value of C_α can be determined directly from the pressure data. This is used to determine the flow angle. The flow angle can then be used to determine both C_{P0} and C_{Ps} which can be combined with the pressures to determine the total and static pressures. However, these coefficients are subject to compressibility effects. To correct for the effect of compressibility,

the calibration is performed at several Mach numbers. The calibration coefficients are interpolated at an estimated Mach number, and then used as described above. This yields a total and static pressure which can be used as a new estimated Mach number. The procedure is repeated until the estimated Mach number is sufficiently close to the Mach number computed from the total and static pressures.

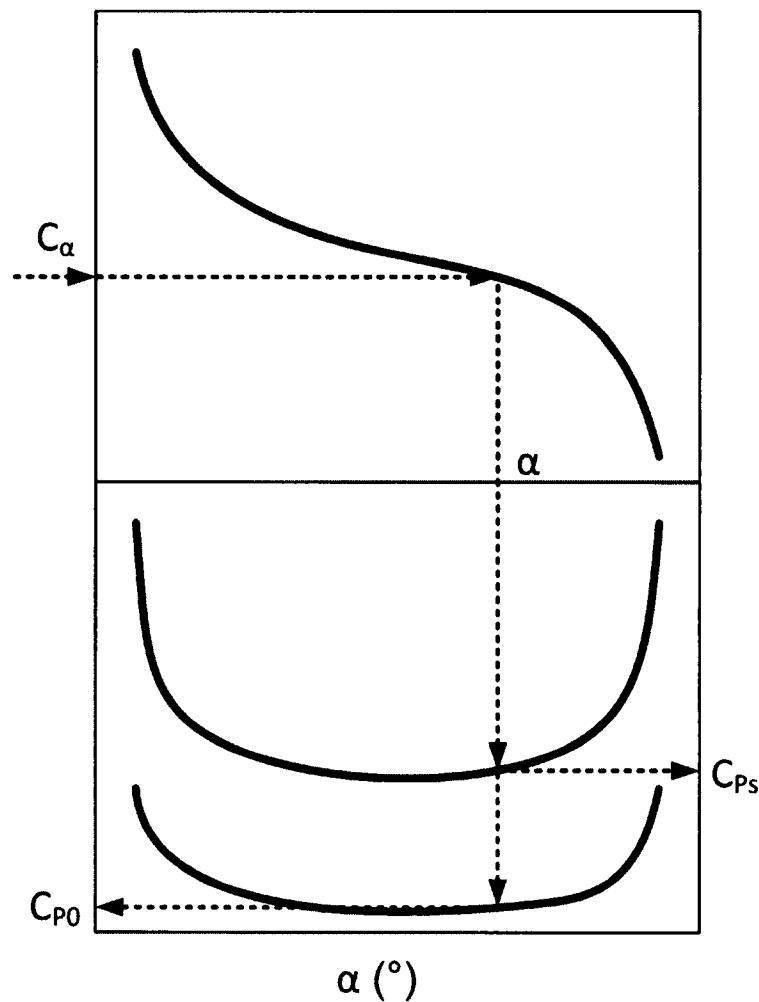


Figure A.1 Procedure to Obtain Flow Direction, Static Pressure, and Total Pressure from the Three Hole Probe Calibration (Reproduced from Argüelles Díaz et al. 2009)

A.2 Calibration Results

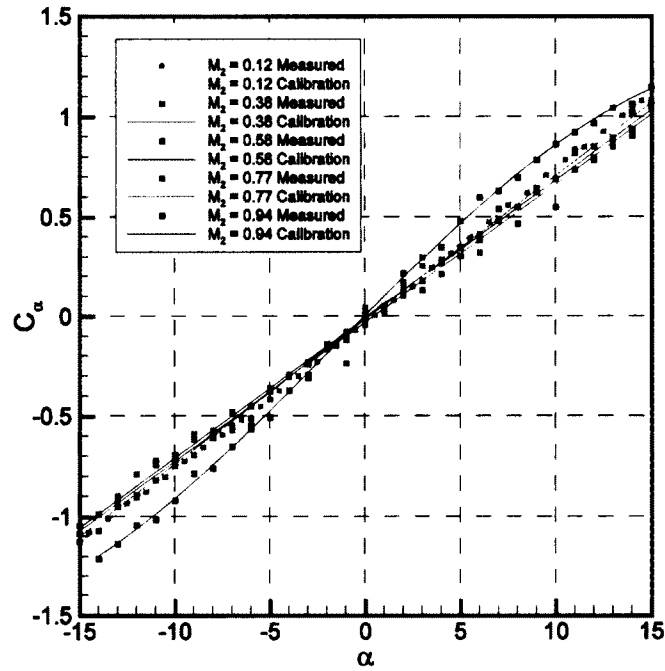


Figure A.2 Calibration Curves for C_α at Five Mach Numbers

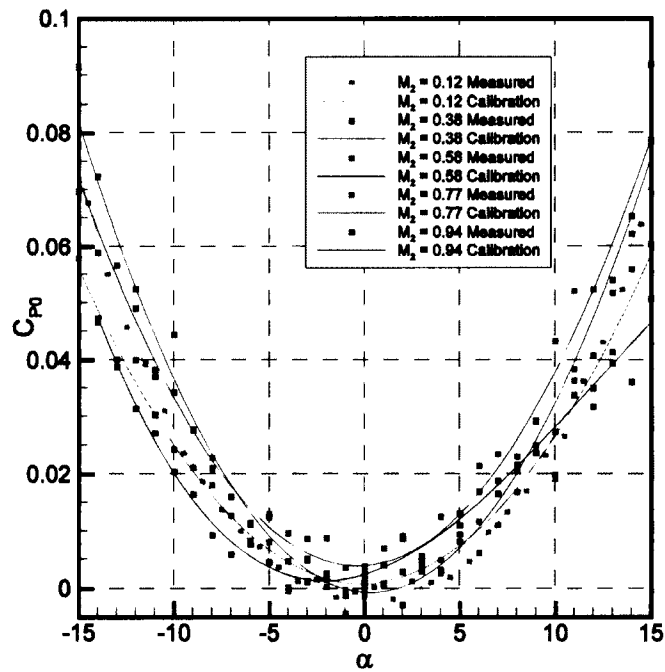


Figure A.3 Calibration Curves for C_{P0} at Five Mach Numbers

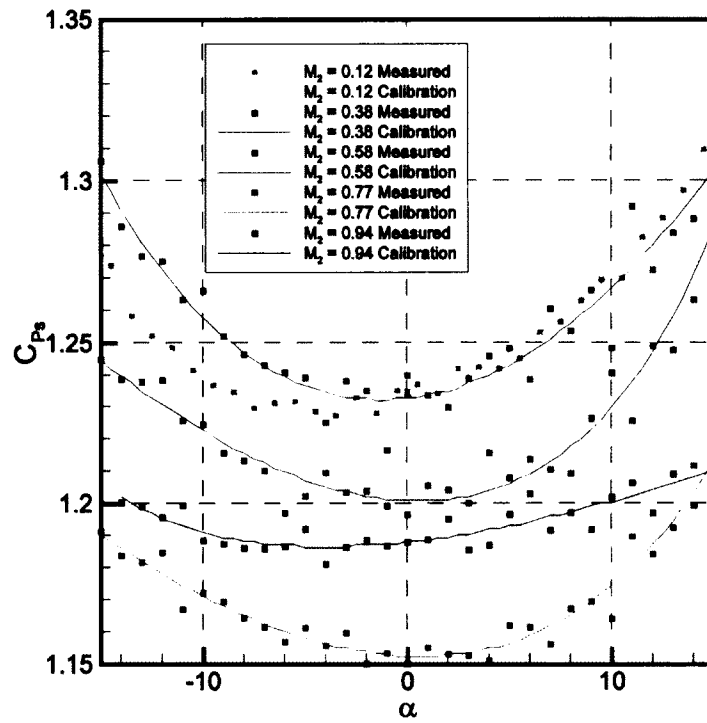


Figure A.4 Calibration Curves for C_{Ps} at Five Mach Numbers

Appendix B

Pressure Transducer Calibrations

The pressure transducers used in this study were calibrated using a Druck DPI 605 Pressure Calibrator. The pressure transducers were given a range of specified pressures with the pressure calibrator, and the resulting voltages were recorded. This range of pressures was repeated three times for both increasing and decreasing pressures to ensure there were no problems with repeatability or hysteresis. A linear regression of the form $P = aV + b$ was used to fit the calibration data. The slope of the correlation has been found to remain constant for months; however, the zero tends to be a function of many parameters which can change from day to day, such as ambient pressure, temperature, and humidity levels. As such, the zero should be corrected daily. The zero correction is based on the pressure read by the Ch11 transducer; this results in some error in the atmospheric pressure. Correcting this error would be impractical and this error is expected to be within reasonable limits. The calibrations are summarised below.

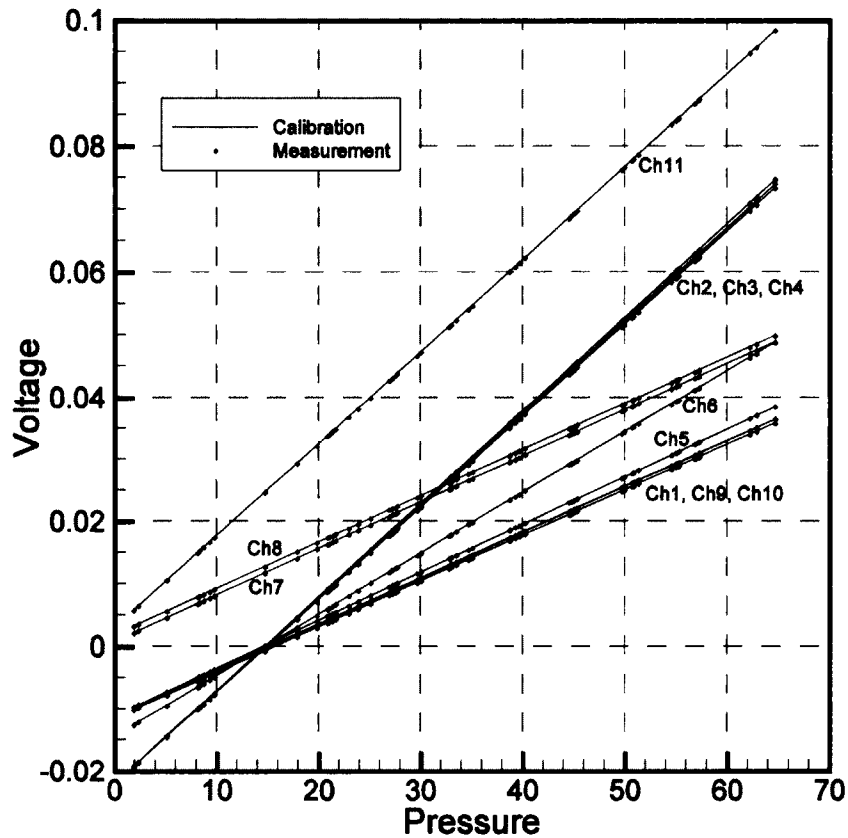


Figure B.1 Transducer Calibration Data and Calibration Curves

Table B.1 Pressure Transducer Calibration Coefficients

Transducer	Slope Coefficient, a	Zero Offset, b
Ch1	1359.51	15.198
Ch2	678.11	14.962
Ch3	669.12	14.757
Ch4	674.07	14.862
Ch5	1305.91	14.614
Ch6	1023.60	14.780
Ch7	1344.00	-0.975
Ch8	1346.00	-2.413
Ch9	1368.49	15.760
Ch10	1359.56	15.279
Ch11	678.39	-1.998

Appendix C

SL2 Geometry

Table C.1 SL2 Coordinates

Suction Surface		Pressure Surface	
x/C_x	y/C_x	x/C_x	y/C_x
0.9998	0.0026	0.0000	0.9337
0.9972	0.0120	0.0011	0.9198
0.9928	0.0256	0.0035	0.9100
0.9873	0.0427	0.0065	0.9026
0.9806	0.0637	0.0093	0.8975
0.9727	0.0883	0.0114	0.8944
0.9635	0.1169	0.0140	0.8911
0.9530	0.1493	0.0153	0.8897
0.9412	0.1855	0.0168	0.8882
0.9281	0.2255	0.0180	0.8870
0.9135	0.2697	0.0191	0.8861
0.8979	0.3168	0.0214	0.8842
0.8813	0.3661	0.0238	0.8824
0.8630	0.4197	0.0276	0.8801
0.8442	0.4741	0.0329	0.8775
0.8249	0.5289	0.0403	0.8749
0.8044	0.5854	0.0508	0.8728
0.7835	0.6418	0.0643	0.8723
0.7618	0.6978	0.0808	0.8743
0.7393	0.7536	0.0996	0.8794
0.7157	0.8089	0.1207	0.8881
0.6906	0.8638	0.1444	0.8978
0.6638	0.9173	0.1713	0.9078
0.6343	0.9701	0.2014	0.9175
0.6021	1.0204	0.2351	0.9261
0.5659	1.0688	0.2722	0.9319
0.5257	1.1135	0.3119	0.9325

Suction Surface		Pressure Surface	
x/C_x	y/C_x	x/C_x	y/C_x
0.4816	1.1530	0.3535	0.9253
0.4317	1.1869	0.3940	0.9085
0.3770	1.2120	0.4304	0.8842
0.3205	1.2249	0.4641	0.8538
0.2625	1.2240	0.4946	0.8201
0.2081	1.2091	0.5226	0.7847
0.1626	1.1849	0.5490	0.7478
0.1234	1.1538	0.5742	0.7099
0.0918	1.1203	0.5985	0.6715
0.0665	1.0867	0.6220	0.6327
0.0462	1.0544	0.6449	0.5936
0.0301	1.0244	0.6673	0.5544
0.0172	0.9970	0.6896	0.5145
0.0073	0.9730	0.7114	0.4748
0.0017	0.9520	0.7330	0.4349
0.0000	0.9337	0.7544	0.3949
--	--	0.7757	0.3548
--	--	0.7961	0.3159
--	--	0.8163	0.2770
--	--	0.8358	0.2394
--	--	0.8538	0.2045
--	--	0.8710	0.1708
--	--	0.8868	0.1398
--	--	0.9012	0.1115
--	--	0.9142	0.0860
--	--	0.9259	0.0629
--	--	0.9361	0.0427
--	--	0.9449	0.0253
--	--	0.9524	0.0103
--	--	0.9586	-0.0019
--	--	0.9632	-0.0109
--	--	0.9687	-0.0165
--	--	0.9740	-0.0191
--	--	0.9787	-0.0200
--	--	0.9817	-0.0199
--	--	0.9847	-0.0194

Suction Surface		Pressure Surface	
x/C_x	y/C_x	x/C_x	y/C_x
--	--	0.9862	-0.0190
--	--	0.9876	-0.0185
--	--	0.9889	-0.0179
--	--	0.9910	-0.0167
--	--	0.9942	-0.0141
--	--	0.9969	-0.0107
--	--	0.9991	-0.0060
--	--	0.9998	0.0026

Table C.2 Blade Surface Static Tap Locations

Suction Side x/C_x	Pressure Side x/C_x
0.05	0.1
0.15	0.3
0.25	0.5
0.5*	0.7
0.6	0.85
0.7	--
0.8	--
0.9	--

Because the static tap at $0.5C_x$ on the suction surface consistently reads lower than expected, data at this location is not presented.

Appendix D

Mixed-Out Computational Results for SL2 Cascade

Table D.1 Mixed-Out Performance Data for CFD Simulations on SL2 Cascade at a Constant Reynolds Number of 611,000

M_2	Re_2	M_1	α_2	Y
0.049	611884.8	0.025	68.4	0.0330
0.098	611873.7	0.050	68.4	0.0329
0.197	611858.1	0.098	68.5	0.0327
0.285	611707.7	0.139	68.6	0.0329
0.394	611536.4	0.184	68.7	0.0329
0.492	611421.2	0.218	68.8	0.0327
0.601	611143.8	0.249	69.0	0.0329
0.641	611092.9	0.258	69.1	0.0327
0.690	610855.8	0.267	69.1	0.0331
0.769	610649.1	0.278	69.3	0.0332
0.808	610542.7	0.282	69.4	0.0333
0.888	610732.2	0.287	69.5	0.0322
0.937	609665.0	0.287	69.7	0.0351
0.983	606330.1	0.288	69.5	0.0450

Table D.2 Mixed-Out Performance Data for CFD Simulations on SL2 Cascade at a Constant Mach Number of 0.49

M_2	Re_2	M_1	α_2	Y
0.491	196499.1	0.217	68.8	0.0401
0.492	394039.0	0.218	68.8	0.0349
0.492	611383.9	0.218	68.8	0.0328
0.493	789195.4	0.218	68.8	0.0321
0.493	986831.3	0.219	68.8	0.0314

Table D.3 Mixed-Out Performance Data for CFD Simulations on SL2 Cascade at a Constant Mach Number of 0.77

M_2	Re_2	M_1	α_2	Y
0.766	196158.9	0.277	69.3	0.0410
0.768	393448.7	0.278	69.3	0.0357
0.769	610644.9	0.278	69.3	0.0332
0.769	788465.7	0.278	69.3	0.0320
0.770	986056.9	0.279	69.3	0.0311

Table D.4 Mixed-Out Performance Data for CFD Simulations on SL2 Cascade with Mach Number and Reynolds Number Corresponding to an Exit Pressure of 1atm

M_2	Re_2	M_1	α_2	Y
0.196	148054.4	0.097	68.5	0.0419
0.285	217390.5	0.138	68.6	0.0385
0.393	305836.3	0.183	68.7	0.0360
0.502	399776.7	0.221	68.8	0.0346
0.601	491282.4	0.249	69.0	0.0340
0.640	529892.4	0.258	69.1	0.0332
0.710	600210.4	0.270	69.2	0.0333
0.769	663992.0	0.278	69.3	0.0327
0.809	708398.7	0.282	69.4	0.0324
0.889	802663.5	0.287	69.5	0.0305

Table D.5 Mixed-Out Performance Data for CFD Simulations on SL2 Cascade with Mach Number and Reynolds Number Corresponding to Wind Tunnel Conditions

M_2	Re_2	M_1	α_2	Y
0.201	156200.6	0.100	68.5	0.0423
0.292	226438.1	0.142	68.6	0.0391
0.399	307383.6	0.185	68.7	0.0369
0.508	388614.2	0.223	68.8	0.0362
0.607	461050.9	0.250	69.0	0.0351
0.697	526106.4	0.268	69.2	0.0344
0.821	613778.3	0.283	69.4	0.0339
0.900	671045.6	0.287	69.6	0.0326
0.948	731208.0	0.287	69.7	0.0355

Appendix E

Mixed-Out Experimental Results for SL2 Cascade

Table E.1 Mixed-Out Performance Data for SL2 Cascade

M_2	Re_2	M_1	AVDR	α_2	Y
0.20	155,000	0.10	1.04	68.1	0.0350
0.29	225,000	0.14	1.02	68.1	0.0333
0.40	308,000	0.19	1.02	68.1	0.0311
0.51	392,000	0.23	1.01	68.3	0.0248
0.61	469,000	0.25	1.01	68.5	0.0221
0.70	531,000	0.27	1.01	68.5	0.0239
0.82	631,000	0.29	1.00	68.9	0.0239
0.90	677,000	0.30	1.00	69.0	0.0236
0.95	761,000	0.29	1.02	69.0	0.0362
1.00	831,000	0.29	1.05	67.7	0.0646

Appendix F

Performance Data at Design Incidence for Several Cascades from the Literature

Table F.1 Performance Data for HS1A Cascade (Corriveau, 2005; Jouini, 2000)

M_2	Re_2	M_1	AVDR	α_2	Y	Y_{corr}	K_{corr}
0.570	511,000	0.399	1.009	56.3	0.0642	0.0625	0.8579
0.749	669,000	0.478	1.000	56.9	0.0568	0.0575	0.7897
0.834	770,000	0.490	1.012	57.2	0.0508	0.0523	0.7183
0.964	870,000	0.512	0.988	57.6	0.0747	0.0779	1.0691
1.059	954,000	0.511	0.998	57.0	0.0936	0.0983	1.3493
1.172	1,020,000	0.512	0.980	57.0	0.0957	0.1012	1.3893
1.277	1,070,000	0.512	0.992	55.0	0.1208	0.1289	1.7703
0.550	500,000	0.385	1.020	56.7	0.0730	0.0708	0.9721
0.710	660,000	0.450	1.020	57.2	0.0670	0.0677	0.9297
0.850	800,000	0.480	1.020	57.7	0.0540	0.0558	0.7666
0.960	880,000	0.484	1.030	57.1	0.0910	0.0949	1.3036
1.060	970,000	0.483	1.030	57.0	0.0850	0.0893	1.2267
1.140	1,040,000	0.480	1.010	57.0	0.1000	0.1061	1.4573
1.160	1,060,000	0.476	1.030	55.9	0.1180	0.1257	1.7262

Table F.2 Performance Data for HS1C Cascade (Corriveau, 2005)

M_2	Re_2	M_1	AVDR	α_2	Y	Y_{corr}	K_{corr}
0.534	477,000	0.394	1.016	55.6	0.0636	0.0612	0.9801
0.729	652,000	0.495	0.999	56.3	0.0567	0.0572	0.9161
0.879	776,000	0.531	0.992	57.0	0.0568	0.0585	0.9373
1.003	868,000	0.545	0.976	57.2	0.0789	0.0822	1.3166
1.103	952,000	0.545	0.982	56.7	0.0821	0.0862	1.3800
1.195	995,000	0.549	0.965	55.8	0.1381	0.1454	2.3279
1.296	1,039,000	0.548	0.966	54.1	0.1805	0.1915	3.0668

Table F.3 Performance Data for HS1D Cascade (Corriveau, 2005)

M_2	Re_2	M_1	AVDR	α_2	Y	Y_{corr}	K_{corr}
0.520	502,000	0.381	1.001	55.4	0.0760	0.0738	0.8371
0.711	686,000	0.483	0.993	56.0	0.0595	0.0604	0.6858
0.857	819,000	0.519	0.996	56.6	0.0497	0.0515	0.5846
0.984	923,000	0.542	0.974	56.7	0.0740	0.0775	0.8797
1.075	996,000	0.543	0.983	55.9	0.0937	0.0987	1.1196
1.180	1,067,000	0.546	0.956	56.0	0.1095	0.1168	1.3257
1.248	1,124,000	0.543	0.961	54.7	0.1473	0.1588	1.8021

Table F.4 Performance Data for HS2 Cascade from Carleton Facility (Jeffries, 2000)

M_2	Re_2	M_1	AVDR	α_2	Y	Y_{corr}	K_{corr}
0.519	479,000	0.231	0.886	66.8	0.0672	0.0647	1.0840
0.683	636,000	0.264	0.915	66.9	0.0593	0.0596	0.9998
0.811	756,000	0.280	0.924	67.0	0.0553	0.0568	0.9528
0.897	860,000	0.281	0.936	67.2	0.0539	0.0562	0.9414
0.936	896,000	0.280	0.946	67.0	0.0666	0.0696	1.1663
0.975	939,000	0.284	0.940	66.8	0.0718	0.0753	1.2622
1.035	1,003,000	0.278	0.956	66.6	0.0910	0.0959	1.6081
1.088	1,069,000	0.275	0.958	65.5	0.1199	0.1279	2.1440
0.530	483,000	0.226	0.910	67.1	0.0611	0.0589	0.9877
0.700	641,000	0.265	0.915	67.2	0.0558	0.0561	0.9411
0.827	759,000	0.280	0.926	67.2	0.0559	0.0575	0.9631
0.922	855,000	0.278	0.939	67.4	0.0518	0.0539	0.9029
0.958	899,000	0.284	0.921	67.4	0.0611	0.0639	1.0709
1.030	938,000	0.287	0.911	67.3	0.0783	0.0821	1.3760
1.065	1,017,000	0.284	0.922	67.0	0.0858	0.0907	1.5201
1.135	1,085,000	0.280	0.936	66.5	0.0965	0.1033	1.7308
1.156	1,114,000	0.282	0.937	65.8	0.1204	0.1296	2.1714
0.534	485,000	0.225	0.911	67.4	0.0702	0.0678	1.1357
0.706	647,000	0.263	0.914	67.5	0.0643	0.0648	1.0860
0.838	769,000	0.276	0.923	67.5	0.0608	0.0626	1.0487
0.924	857,000	0.280	0.934	67.4	0.0597	0.0621	1.0411
0.958	893,000	0.282	0.924	67.5	0.0709	0.0741	1.2420
0.998	939,000	0.286	0.912	67.4	0.0713	0.0748	1.2538
1.067	1,012,000	0.282	0.926	67.1	0.0878	0.0927	1.5533

Table F.5 Performance Data for HS2 Cascade from VKI Rhode-St.-Genèse, Belgium (RG) Facility (Klock et al. 1986)

M_2	Re_2	M_1	AVDR	α_2	Y	Y_{corr}	K_{corr}
0.420	337,000	0.191	0.937	66.1	0.0571	0.0517	1.0653
0.521	423,000	0.222	0.945	66.3	0.0571	0.0538	1.1092
0.652	536,000	0.256	0.936	66.6	0.0556	0.0545	1.1244
0.772	666,000	0.275	0.925	66.9	0.0597	0.0604	1.2449
0.861	765,000	0.281	0.929	67.1	0.0556	0.0573	1.1805
0.935	847,000	0.280	0.928	67.2	0.0698	0.0726	1.4956

Table F.6 Performance Data for HS2 Cascade from DFVLR Goettingen, West Germany (GO) Facility (Kiock et al. 1986)

M_2	Re_2	M_1	AVDR	α_2	Y	Y_{corr}	K_{corr}
0.292	378,000	0.131	0.977	66.3	0.0456	0.0422	1.0022
0.393	490,000	0.172	0.975	66.4	0.0424	0.0410	0.9744
0.488	592,000	0.209	0.976	66.4	0.0440	0.0438	1.0414
0.587	673,000	0.234	---	66.6	0.0461	0.0467	1.1099
0.684	770,000	0.253	0.964	67.8	0.0512	0.0527	1.2538
0.782	827,000	0.269	0.958	66.9	0.0557	0.0578	1.3747
0.874	867,000	0.275	0.945	67.3	0.0607	0.0633	1.5040
0.914	834,000	0.278	0.939	67.4	0.0640	0.0664	1.5793
0.959	893,000	0.281	0.937	67.1	0.0760	0.0793	1.8863
1.055	898,000	0.281	0.933	66.7	0.0980	0.1024	2.4344
1.131	880,000	0.283	0.924	66.1	0.1282	0.0422	1.0022
1.168	806,000	0.279	0.965	63.0	0.2671	0.0410	0.9744
1.185	857,000	0.279	0.941	65.1	0.1449	0.0438	1.0414
1.225	796,000	0.279	0.954	62.2	0.2842	0.0467	1.1099

Table F.7 Performance Data for HS2 Cascade from Braunschweig, West Germany (BS) Facility (Kiock et al. 1986)

M_2	Re_2	M_1	AVDR	α_2	Y	Y_{corr}	K_{corr}
0.392	490,000	0.166	0.989	66.8	0.0424	0.0410	1.0784
0.587	673,000	0.225	0.987	66.9	0.0461	0.0467	1.2289
0.784	786,000	0.256	0.993	67.1	0.0515	0.0532	1.3995
0.830	798,000	0.259	0.980	67.3	0.0560	0.0579	1.5236
0.875	785,000	0.263	0.987	67.3	0.0562	0.0580	1.5258
0.918	776,000	0.266	0.986	67.4	0.0579	0.0596	1.5695
0.967	771,000	0.264	0.977	67.3	0.0917	0.0944	2.4855

Table F.8 Performance Data for SL1 Cascade (Taremi 2010)

M_2	Re_2	M_1	AVDR	α_2	Y	Y_{corr}	K_{corr}
0.636	490,000	0.270	0.980	68.9	0.0287	0.0278	1.1118
0.756	590,000	0.290	0.980	69.0	0.0288	0.0286	1.1458
0.874	690,000	0.300	0.990	69.2	0.0292	0.0297	1.1898

Table F.9 Performance Data for SL2 Cascade (Taremi 2010)

M_2	Re_2	M_1	AVDR	α_2	Y	Y_{corr}	K_{corr}
0.645	520,000	0.270	1.020	67.9	0.0271	0.0265	0.9514
0.762	620,000	0.290	1.020	69.0	0.0275	0.0276	0.9897
0.886	720,000	0.300	1.020	68.5	0.0283	0.0289	1.0385

Table F.10 Performance Data for CNPM Cascade (Perdichizzi, 1990)

M_2	Re_2	M_1	AVDR	α_2^*	Y	Y_{corr}	K_{corr}
0.184	168,091	0.077	---	---	0.0569	0.0421	0.8963
0.194	182,517	0.081	---	---	0.0552	0.0428	0.9114
0.209	201,612	0.087	---	---	0.0563	0.0460	0.9808
0.313	340,540	0.127	---	---	0.0525	0.0476	1.0142
0.326	357,363	0.131	---	---	0.0507	0.0464	0.9888
0.505	595,685	0.188	---	---	0.0505	0.0503	1.0720
0.519	612,072	0.192	---	---	0.0484	0.0484	1.0313
0.717	836,466	0.232	---	---	0.0477	0.0495	1.0551
0.710	828,436	0.231	---	---	0.0434	0.0450	0.9592
0.746	873,237	0.236	---	---	0.0494	0.0515	1.0967
0.799	943,325	0.242	---	---	0.0470	0.0493	1.0495
0.866	1,029,508	0.247	---	---	0.0521	0.0552	1.1755
0.902	1,076,066	0.248	---	---	0.0560	0.0598	1.2746
0.990	1,190,350	0.249	---	---	0.0587	0.0640	1.3635
1.009	1,216,077	0.249	---	---	0.0567	0.0621	1.3232
1.022	1,232,682	0.248	---	---	0.0613	0.0673	1.4341
1.113	1,372,217	0.245	---	---	0.0610	0.0684	1.4579
1.217	1,530,678	0.237	---	---	0.0688	0.0789	1.6808
1.268	1,565,004	0.231	---	---	0.0737	0.0848	1.8075
1.264	1,563,524	0.231	---	---	0.0803	0.0925	1.9698
1.210	1,519,371	0.235	---	---	0.0819	0.0937	1.9971
1.366	1,604,408	0.218	---	---	0.0888	0.1028	2.1893
1.388	1,613,056	0.216	---	---	0.0848	0.0983	2.0936
1.551	1,678,272	0.192	---	---	0.1113	0.1300	2.7705
1.576	1,688,280	0.188	---	---	0.1208	0.1413	3.0097
1.561	1,682,500	0.188	---	---	0.1276	0.1491	3.1767

*Nominal exit angle = 66°

Table F.11 Incompressible Limits of Reynolds Number Corrected Total Pressure Loss Coefficient

Cascade	$Y_{corr,inc}$
HS1A	0.0728
HS1C	0.0625
HS1D	0.0881
HS2 - CU	0.0597
HS2 - GO	0.0421
HS2 - RG	0.0485
HS2 - BS	0.0380
CNPM	0.0469
SL1	0.0250
SL2	0.0278
SL2 - CFD	0.0329

Table F.12 Onset Mach Number of Shock Losses

Cascade	$M_{2,on}$
HS1A	0.84
HS1C	0.87
HS1D	0.85
HS2 - CU	0.93
HS2 - GO	0.91
HS2 - RG	0.86
HS2 - BS	0.92
CNPM	0.80
SL1	--
SL2	0.90
SL2 - CFD	0.90